

THE VERTICAL PROPAGATION OF INERTIAL WAVES
IN THE OCEAN

by

KEVIN DOUGLAS LEAMAN

B.S., University of Michigan
(1970)

M.S., University of Michigan
(1972)

SUBMITTED IN PARTIAL FULFILLMENT OF THE
REQUIREMENTS FOR THE DEGREE OF
DOCTOR OF PHILOSOPHY

at the

MASSACHUSETTS INSTITUTE OF TECHNOLOGY

and the

WOODS HOLE OCEANOGRAPHIC INSTITUTION

June, 1975

Signature of Author.....

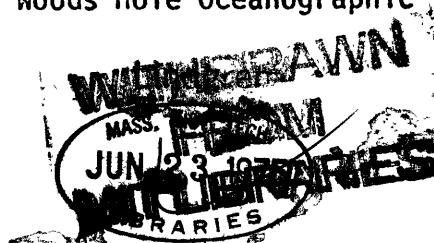
Joint Program in Oceanography, Massachusetts
Institute of Technology - Woods Hole
Oceanographic Institution, and Department of
Earth and Planetary Sciences, and Department
of Meteorology, Massachusetts Institute of
Technology, June 1975

Certified by.....

Thesis Supervisor

Accepted by.....

Chairman, Joint Oceanography Committee in the
Earth Sciences, Massachusetts Institute of
Technology - Woods Hole Oceanographic
Institution



THE VERTICAL PROPAGATION OF INERTIAL WAVES IN THE OCEAN

by

Kevin Douglas Leaman

Submitted to the Massachusetts Institute of Technology-Woods Hole Oceanographic Institution Joint Program in Oceanography in June, 1975, in partial fulfillment of the requirements for the degree of Doctor of Philosophy.

ABSTRACT

A set of vertical profiles of horizontal ocean currents, obtained by electro-magnetic profilers in the Atlantic Ocean southwest of Bermuda in the spring of 1973, has been analyzed in order to study the vertical structure and temporal behavior of internal waves, particularly those with periods near the local inertial period. An important feature of the observed structure is the polarization of horizontal velocity components in the vertical. This polarization, along with temporal changes of the vertical wave structure seen in a time series of profiles made at one location, has been related to the direction of vertical energy flux due to the observed waves. Whereas the observed vertical phase propagation can be affected by horizontal advection of waves past the point of observation, the use of wave polarization to infer the direction of vertical energy propagation has the advantage that it is not influenced by horizontal advection. The result shows that at a location where profiles were obtained over smooth topography, the net energy flux was downward, indicating that the energy sources for these waves were located at or near the sea surface. An estimate of the net, downward energy flux ($\sim .2 - .3$ erg/cm²/sec) has been obtained. Calculations have been made which show that a frictional bottom boundary layer can be an important energy sink for near-inertial waves. A rough estimate suggests that the observed, net, downward energy flux could be accounted for by energy losses in this frictional boundary layer. A reflection coefficient for the observed waves as they reflect off the bottom has been estimated.

In contrast, some profiles made over a region of rough topography indicate that the rough bottom may also be acting to generate near-inertial waves which propagate energy upward.

Calculations of vertical flux of horizontal kinetic energy, using an empirical form for the energy spectrum of internal waves, show that this vertical flux reaches a maximum for frequencies 10% - 20% greater than the local inertial frequency. Comparison with profiler velocity data and frequency spectra supports the conclusion that the dominant waves had frequencies 10% - 20% greater than the inertial frequency. The fact that the waves were propagating energy in the vertical is proposed as the reason for the observed frequency shift.

Finally, energy spectra in vertical wave number have been calculated from the profiles in order to compare the data with an empirical model of the energy density spectrum for internal waves proposed by C. Garrett and W. Munk (1975). The result shows that although the general shape and magnitude of the observed spectrum compares well with the empirical model, the two-sided spectrum is not symmetric in vertical wave number. This asymmetry has been used to infer that more energy was propagating downward than upward. These calculations have also been used to obtain the coherence between profiles made at the same location, but separated in time (the so-called dropped, lagged, rotary coherence). This coherence is compared with the aforementioned empirical model. The coherence results show that the contribution of the semidiurnal tide to the energy of the profiles is restricted to long vertical wave lengths.

Thesis Supervisor: Dr. Thomas B. Sanford
Title: Associate Scientist

ACKNOWLEDGEMENTS

I wish to thank above all Dr. Thomas B. Sanford of the Woods Hole Oceanographic Institution for providing the data on which this report is based, and for many helpful comments and suggestions. Initial acquisition and processing of data obtained by the electro-magnetic profiler was successful primarily due to the efforts of R. G. Drever, E. Denton, A. Bartlett, J. Dunlap and J. Stratton, all of the above institution. Support for the experiment which is described in this report was provided by the Office of Naval Research under contracts N00014-66-C-0241, NR 083-004 and N000 14-74-C-0262, NR 083-004.

For my personal support as a graduate student I thank the National Science Foundation for its award to me of a graduate fellowship for three years. I also thank the Office of Naval Research (under the above contracts) for providing part of my support.

TABLE OF CONTENTS

	Page
Abstract	2
Acknowledgements	4
List of Figures	7
Chapter I Introduction and Historical Review	10
Chapter II Description and Analysis of Data from the Five-day Time Series of Profiles	21
a.) Dominance of inertial-period motions in EMVP profiles--the "mirror-imaging" of profiles	21
b.) Low-frequency "geostrophic" profiles	23
c.) High-frequency velocity components in the upper 2.5 km as a function of time	27
d.) The average perturbation kinetic energy profile, and a smoothed profile of Brunt- Väisälä frequency	32
e.) The stretching of the vertical coordinate and the normalization of velocity by the mean Brunt-Väisälä profile	36
f.) Spectral decomposition of stretched pro- files	42
g.) Paired profiles	54
Chapter III Vertical Polarization and the Vertical Propa- gation of Internal-inertial Waves	57
a.) Summary of data	57
b.) The vertical spatial behavior of hori- zontal internal wave velocity components	58

	Page
Chapter III c.) Polarization in the deep water	71
d.) Comparison with meteorological observations	72
Chapter IV The Use of the Ratio of Clockwise to Counterclockwise Energy as a Reflection Coefficient. Reflection of Internal Waves from a Smooth Bottom	76
a.) Calculation of a reflection coefficient for the observed waves	76
b.) A model for the reflection of internal waves from a smooth bottom	81
Chapter V Comparison of Vertical Wave Number Spectra with Theoretical Models. Computation of Dropped, Time-lagged, Rotary Coherence (DLRC). The Vertical Energy Flux of Internal-inertial Waves	89
a.) Vertical wave number spectra	89
b.) Dropped, time-lagged, rotary coherence of profiles	98
c.) The vertical energy flux of near-inertial waves	107
Chapter VI Some Observations over Rough Topography	119
Chapter VII Conclusions, a Further Discussion of Some of the Data and Recommendations for Future Experiments	126
Appendix A Profile Locations and Times	142
Appendix B Use of Electro-magnetic Velocity Profilers to Measure Internal Waves	146
Appendix C Accuracy and Precision of Observations	159
Appendix D A More General Treatment of the Partition of Energy Between Clockwise and Counterclockwise Spectra	163
Bibliography	170
Biographical Note	174

LIST OF FIGURES

Figure Number		Page
1.	Electro-magnetic velocity profiler	16
2.	Bathymetry of the MODE region. Location of central mooring time series is shown by an X. The ridge over which rough topography profiles were made is circled.	18
3.	Paired drops, 219D and 221D, made at the same location and with a time separation of one half of an inertial period.	22
4.	Average profile of the east velocity component during the five-day time series.	25
5.	Average profile of the north velocity component during the five-day time series.	26
6.	Contours of the east velocity component during the five-day time series. Negative east components are indicated by hatched regions.	28
7.	Contours of the north velocity component during the five-day time series. Negative north components are indicated by hatched regions.	29
8.	Average profiles of high-frequency horizontal kinetic energy and Brunt-Väisälä frequency.	33
9.	Stretched and unstretched vertical pressure coordinates.	39
10.	East component of profile 219D as originally obtained (a), after removal of the mean profile (b), and after stretching and normalizing(c).	40
11.	North component of profile 219D as originally obtained (a), after removal of the mean profile (b), and after stretching and normalizing (c).	41
12.	Total spectrum (east and north energy) for 9 down profiles.	43

Figure Number	Page
13. Clockwise (CW) and counterclockwise (ACW) spectra for 9 down profiles. In the text, CW is $C(m')$ and ACW is $A(m')$.	45
14. Spectra of east and north velocity components for 9 down profiles.	48
15. Total spectrum (east and north energy) for 9 up profiles.	49
16. Clockwise (CW) and counterclockwise (ACW) spectra for 9 up profiles.	50
17. Spectra of east and north velocity components for 9 up profiles.	51
18. Simultaneous paired drops, 235U and 236U, separated horizontally by 4.8 km.	55
19. Horizontal coordinate rotation (see equations III-2).	59
20. Direction of rotation of the horizontal velocity vector of an internal wave for positive and negative vertical wave numbers. The curved arrow shows the direction in which \vec{v} rotates with increasing z .	59
21. Propagation diagram for internal waves. \vec{C}_g is the group velocity vector, \vec{k} is the wave number vector, and \vec{v} is a vector representing water velocity.	62
22. Reflection coefficient $A(m')/C(m')$.	79
23. Comparison of theoretical and observed total energy spectra in stretched vertical wave number.	96
24. Dropped, lagged, rotary cospectrum (normalized) between velocity components U_1 and U_3 (see text for a further description of Figures 24 to 27).	101
25. Dropped, lagged, rotary cospectrum (normalized) between velocity components V_1 and V_3 .	102
26. Dropped, lagged, rotary quadrature spectrum (normalized) between velocity components U_1 and U_3 .	103

Figure Number		Page
27.	Dropped, lagged, rotary quadrature spectrum (normalized) between velocity components V_1 and V_3 .	104
28.	Frequency dependence of the vertical flux of horizontal kinetic energy, using a theoretical form for the energy spectrum of the internal wave field.	114
29.	Frequency spectrum, obtained by averaging 12 spectra computed from current meter records at 1500 m in the MODE region. Energy density units are $(\text{cm/sec})^2/\text{cph}$.	117
30.	Smoothed hodograph of profile 190D between 3000 dbar and 4500 dbar. Depths are in hundreds of decibars.	122
31.	Smoothed hodograph of profile 192D between 3000 dbar and 4500 dbar. Depths are in hundreds of decibars.	123

Chapter I Introduction and Historical Review

For many years the subject of internal waves has been of intense interest to meteorologists, aeronomists, and oceanographers. These internal waves are oscillations in the atmosphere or ocean that are supported by buoyancy and pressure forces, and also by the fictitious Coriolis force introduced by the rotation of the earth. Oscillations having time and length scales appropriate to internal waves have been observed at many locations in the ocean. In the atmosphere, motions having time and space scales appropriate to internal waves have also been observed. However, until recently, meteorologists and oceanographers have been studying internal wave phenomena from decidedly different points of view. This has been brought about primarily by the different types of instrumentation used in the two disciplines. Observations of atmospheric internal waves are discussed first.

In the years since World War II, several methods have been developed by meteorologists for observing variables such as wind and temperature in the atmosphere. Wind measurements, which are of primary interest in the present study, have been performed using the following methods: tracking the distortion of smoke (actually sodium) trails left by high altitude rockets; tracking of radar reflecting balloons with ground-based radar; visual tracking of meteor trails by telescopes; tracking chaff (strips of aluminized reflecting material) with ground-based radar; and radio-echo tracking of

meteor trails. All of these methods have their disadvantages. Rockets, for example, are expensive to use, and they have not usually been applied to rapidly repeated measurements in the atmosphere. Visual and radio-echo tracking of meteors depend, of course, on a sufficient number of meteors entering the upper atmosphere. Except in rare cases when meteor showers occur, the number of meteors in the atmosphere has usually been insufficient to study high-frequency oscillations in the wind field, such as internal waves. More recently, tracking of ascending, radar reflecting balloons has provided better measurements of atmospheric winds.

All of these methods, although diverse in concept, have in common the fact that they provide profiles of horizontal atmospheric winds as a function of altitude. Many examples of these profiles have been presented in the literature (see, for example, the paper by L. Broglio in "Proceedings of the First International Symposium on Rocket and Satellite Meteorology," in which results from rocket profiles are presented, and the radar balloon observations of Endlich, Singleton and Kaufman (1969)). Thus, the attention of meteorologists and aeronomists has historically been directed toward observing the vertical structure of the atmospheric wind field. Attempts at using repeated profiles to determine the amount of energy contributed by high-frequency (internal wave and turbulent) oscillations at different time scales or frequencies have been notably less successful than the measurements of the

profiles themselves. These attempts have usually consisted of trying to fit diurnal and semidiurnal period sinusoids to the winds observed at a given altitude (Elford and Robertson, 1953; Smith, 1960).

The situation in the oceans has been substantially different. Until recently, the primary tools which oceanographers have used to observe oscillations with frequencies in the internal wave range have been fixed-location current meters, temperature sensors, and neutrally buoyant floats. The current meter allows one to measure, at a fixed point in the ocean, the horizontal current vector as a function of time. If current meters are placed at many locations in a part of the ocean (by being put on moorings), then time measurements in a spatial array are obtained. These arrays allow one to obtain good temporal resolution of velocity, but only at a limited number of points in space.

Current meters have provided a large volume of data on the temporal behavior of the ocean. Fofonoff (1969) showed that the behavior of horizontal velocity components and temperature in the internal wave frequency band (those frequencies corresponding to periods between one half of the local pendulum day, $1/(2\sin(\text{Lat.}))$ days, and the local stable oscillation period of a particle of water, or the Brunt-Väisälä period) could be reasonably well related to the expected behavior of internal waves in a linear model. Webster (1968) summarizes many of the current meter observations that have been used to study internal waves and other high-frequency

oceanic phenomena. Most of these current meter records have shown that the dominant contributions to horizontal kinetic energy spectra come from frequencies near the local inertial frequency, corresponding to the aforementioned period of one half of a pendulum day, and from the tides.

Temperature observations have been made using several different methods. Hauritz, Stommel and Munk (1959) observed temperature oscillations as a function of time at two fixed depths, 50 and 550 meters, near Bermuda. These data yielded frequency spectra for the temperature oscillations.

Another method, employed by Charnock (1965) and LaFond and LaFond (1971), is to tow a weighted thermistor chain behind a vessel. If the speed of the vessel is large compared to the horizontal phase propagation speed of the waves being observed, spectral analysis of the temperature trace obtained at a given depth gives a horizontal wave number spectrum of the observed isotherm displacements. Similar observations can be obtained by towing an isotherm-following "fish" behind a research vessel (Katz, 1973, 1975).

The use of neutrally buoyant floats has also provided data on internal waves. Pochapsky (1972) used such floats to observe oscillations of temperature and horizontal velocity with periods in the internal wave range. Voorhis (1968) obtained measurements of vertical motion with a neutrally buoyant float which rotates in the presence of vertical flow past the float. The rate of rotation of the float gives an estimate of this vertical flow.

Many of the observations described above (as well as others which have not been mentioned) have been gathered together by Garrett and Munk (1972, 1975) in an attempt to model the energy spectrum of internal waves in frequency and horizontal wave number. The model depends not only on individual spectra of temperature or velocity, but also on the correlation, or coherence, between observations made at different points of a spatial array. Coherence observations have also been gathered together and described by those authors (Garrett and Munk, 1972, 1975).

A major difficulty with this type of model construction has been lack of knowledge concerning the vertical structure of the wave field. This vertical structure is difficult to determine using velocity (or temperature) measurements from moorings, since only a limited number of instruments can be placed on any one mooring. Thus, vertical profiles of horizontal velocity, which have been the most common method of observation in the atmosphere, have been the least common type of observation in oceanographic work.

Recently, however, several methods have been developed that allow the oceanographer to obtain vertical profiles of horizontal current in the ocean that are analogous to profiles obtained in the atmosphere. One such method involves the use of acoustic transponders located on the ocean bottom to track a float as it descends through the water column (Rossby, 1969; Pochapsky and Malone, 1972).

Another method uses a moored vertical cable with inclinometers located at various points along the cable (McNary, 1968).

Horizontal currents cause the cable to distort. This distortion, as measured by the inclinometers, can then be converted to values of the horizontal velocity component along the cable. A third method uses horizontal electrical currents induced by the flow of ocean water through the terrestrial magnetic field (Sanford, 1971). The device which measures these electrical currents is called an electro-magnetic velocity profiler, or EMVP. A picture of this device, developed by T. Sanford and R. Drever of the Woods Hole Oceanographic Institution, is shown in Figure 1. The EMVP is released from a research vessel, and as it falls to the ocean bottom it continuously records the horizontal component of electrical current, as well as temperature, conductivity, and pressure. When the EMVP reaches the bottom, it reverses and ascends through the water column, again recording the above variables. There are no hard connections (cables, etc.) between the research vessel and the EMVP: the only communication from EMVP to ship is through acoustic telemetry. All data are recorded on 7-track magnetic tape within the EMVP. Upon return to the ship, the data on the tape is reformatted onto 9-track tape, and several computer programs are used to convert the internally recorded variables to their physical counterparts, such as temperature. Another routine, using a conversion equation, converts horizontal electrical current density to horizontal water flow relative to an unknown, but depth independent, horizontal velocity. A further description of the EMVP and its operation can be found in Sanford, et. al. (1974).

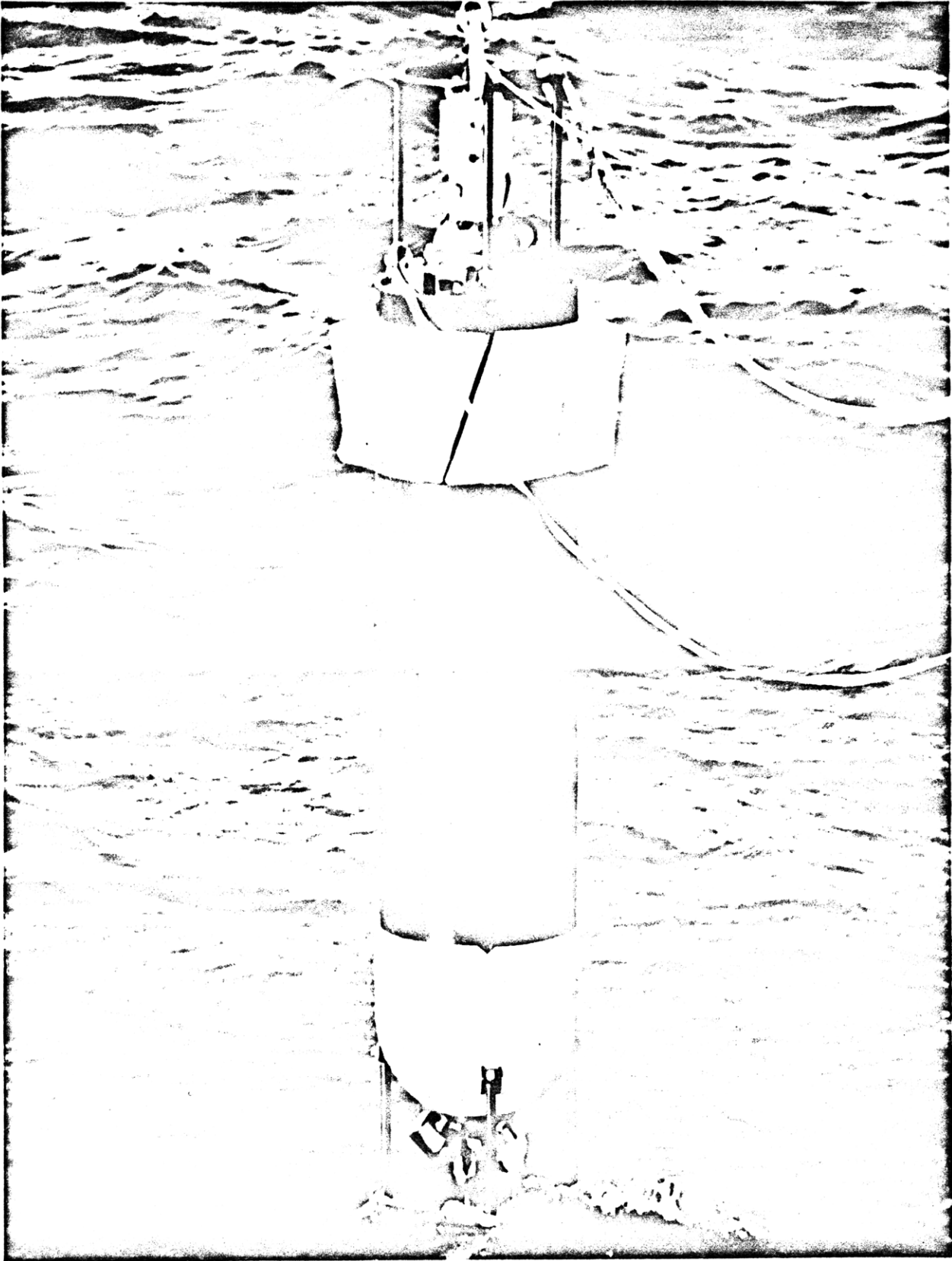


Figure 1. Electro-magnetic velocity profiler

The horizontal velocity component is not the only quantity that has been measured by vertical profiling. Vertical profiles of temperature, conductivity and salinity have been obtained by raising and lowering a CTD (conductivity-temperature-depth sensor). Such data have been presented by Hayes (1975) and Hayes, et. al. (1975).

We turn now to a description of the experiment which is discussed in this report. In the spring of 1973 a large-scale oceanographic experiment called MODE (Mid-Ocean Dynamics Experiment) was carried out in the Atlantic Ocean, southwest of Bermuda. A map showing the bathymetry in the region of this experiment is shown in Figure 2. The EMVP was used to take a large number of vertical profiles during the experiment. The locations, dates and times of all profiles are given in Appendix A. We are going to concentrate particularly on two subsets of all the profiles. The first subset consists of a time series of repeated profiles made at the center of the experiment ($69^{\circ} 40' W$, $27^{\circ} 59' N$). This will be called the "central mooring time series," since the central mooring of the MODE experiment was located near these coordinates. This time series, made up of 20 profiles, lasted from June 11-15, 1973. (These profiles are designated by an asterisk in Appendix A). As can be seen from Figure 2, the location of the series is over a region of smooth bottom topography. The second subset is made up of some profiles taken around a ridge east of the time series, in a region of rough topography. These locations are shown in Figure 2.

Any profile that has ever been made by the EMVP has shown two dominant contributions to the velocity structure in the vertical. The first contribution is a low-frequency part, which does not change appreciably from one profile to the next at the same location, and which corresponds well with current shear derived by geostrophic shear calculations in that region. The second part is a high-frequency contribution which is evidently due to internal waves, particularly those with frequencies near the local inertial frequency. It is this high-frequency part that will be of main interest in what follows.

Chapter II gives a description and analysis of the velocity data obtained from the five-day time series of profiles. Plots of mean flow and average perturbation horizontal kinetic energy versus depth are given, as are contour plots showing the evolution of features in the velocity field in time, and spectra of the high-frequency profile structure in vertical wave number.

One of the most interesting results obtained from the spectral analysis in Chapter II is that there is a definite elliptical polarization of the high-frequency waves in the profiles. That is, the horizontal current vector in a profile (after the mean has been removed) clearly tends to rotate with depth. This polarization and its relation to the vertical propagation of internal wave energy is described in Chapter III. In Chapter III, comparisons will be made between our observations and similar observations made in the atmosphere.

Chapter IV describes the reflection of internal waves from a smooth bottom. The spectra presented in Chapter II are used to attempt to calculate reflection coefficients for these waves.

Chapter V presents a comparison of the vertical wave number spectra in Chapter II to the theoretical models of Garrett and Munk (1972, 1975). The coherence of velocity components between pairs of profiles separated by a time lag is also presented. Vertical energy flux of the observed waves is discussed in more detail.

Chapter VI discusses the profiles obtained over rough topography. Chapter VII provides some conclusions, a further discussion of some of the data, and recommendations for future experiments.

Chapter II Description and Analysis of Data from the Five-day Time Series of Profiles

It was mentioned in the introduction that EMVP data is historically more akin to meteorological measurements in the upper atmosphere than to oceanographic data. In particular, profiler data emphasizes the vertical structure of the ocean or atmosphere, while until recently most oceanographic work has emphasized the temporal behavior of oceanic motions. This chapter will present, in various forms, horizontal velocity data obtained during the five-day series of profiles, and will describe some of the methods used to reduce and analyze this data. Succeeding chapters are devoted to the interpretation of results obtained from this analysis. The reader may refer to Appendix B for a brief discussion of internal wave measurements made by the EMVP and to Appendix C for a discussion of the accuracy and precision of data presented in the following sections.

a.) Dominance of inertial-period motions in EMVP profiles--the "mirror-imaging" of profiles

Figure 3 shows the east and north components of two profiles, 219D and 221D. (The letter D signifies that the down portion of a drop was used. The letter U will be used to denote the up portion of a drop.) The time separation between the two profiles is approximately one half of an inertial period. The vertical sampling rate is one point every 10 dbar. It is evident from the figure that,

VELOCITY PROFILES 219D & 221D

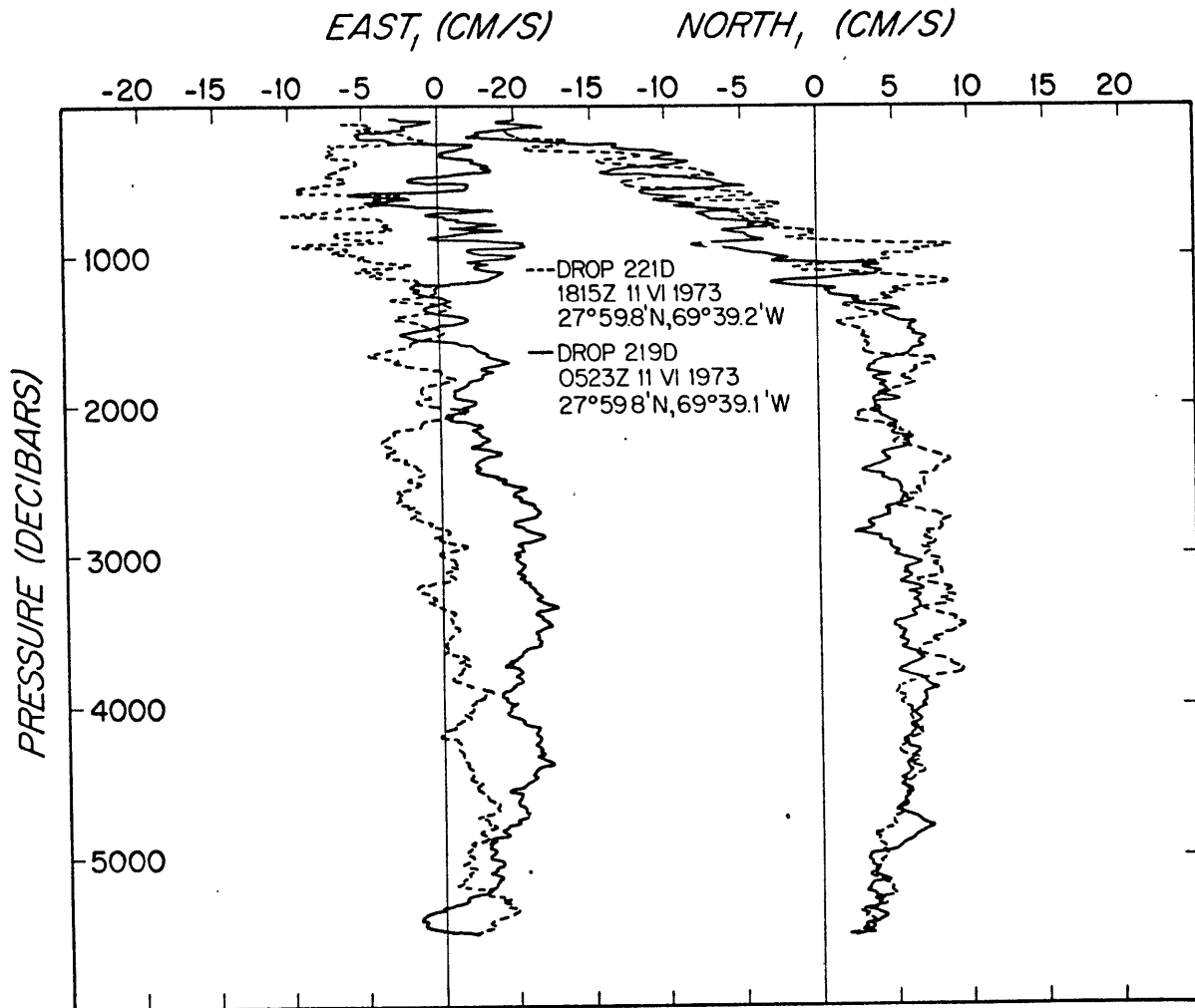


Figure 3. Paired drops, 219D and 221D, made at the same location and with a time separation of one half of an inertial period.

superimposed on a low-frequency shear in the profiles, there is a considerable amount of high-frequency activity. This high-frequency activity is evident in the almost total reversal of the velocity structure over the time interval. If we remove the low-frequency shear of the profiles (by averaging all drops in the time series and subtracting the low-frequency shear profile from each drop separately), we find that the high-frequency part that is left over is negatively correlated in profiles made one half of an inertial period apart. This negative correlation, or "mirror-imaging," is an indication that the EMVP profiles are strongly dominated in the high frequencies by motions with periods close to the local inertial period. It will be shown later that some of the observed variability is also contributed by the semidiurnal tide.

b.) Low-frequency "geostrophic" profiles

For ease of discussion we will call oscillations with frequencies less than the local inertial frequency "low-frequency" oscillations, or the "geostrophic" part of the flow. Similarly, oscillations with frequencies greater than or equal to the inertial frequency will be called "high-frequency," or "internal wave" oscillations. It should be clear that these terms are used solely to simplify the description of the data. We do not intend to imply that all motions with frequencies less than inertial are in geostrophic balance. Also, high-frequency motions are not necessarily due to internal waves. A certain amount of high-frequency energy may be contributed by turbulence, for example. It is known,

however, that there is a "well," or depression in frequency spectra obtained in the MODE region (see Figure 29). This well exists in the range of periods from the inertial period to periods of several days. Therefore, averaging velocity data over several days will partition the profile data into high-frequency and low-frequency parts. In order to characterize more fully this partition of energy between the low-frequency "geostrophic" and high-frequency "internal wave" parts of the profiles, we have averaged all 20 profiles in the time series. (The 20 profile time series occupies a time interval of about 103 hours.) This averaging was done simply by removing the "barotropic," or depth-averaged, part of each profile, and then taking an average over the 20 drops at each level. The depth-averaged part of each profile was removed because it is unknown and is not the true barotropic part of the velocity profile (see Sanford (1971)). The resulting low-frequency profiles are shown in Figures 4 and 5 for the east and north components.

There is some indication in these mean profiles of a decrease in the mean shear in the 18° water (around 400 dbar). There is also an indication that the mean shear increases again near the bottom, in the Antarctic Bottom Water. In terms of the geostrophic shear relation this might be expected. Figure 8 shows the mean Brunt-Väisälä profile at the location of the time series. Since the Brunt-Väisälä frequency is proportional to the square root of the vertical potential density gradient, this profile shows that the vertical density gradient has a relative minimum at about

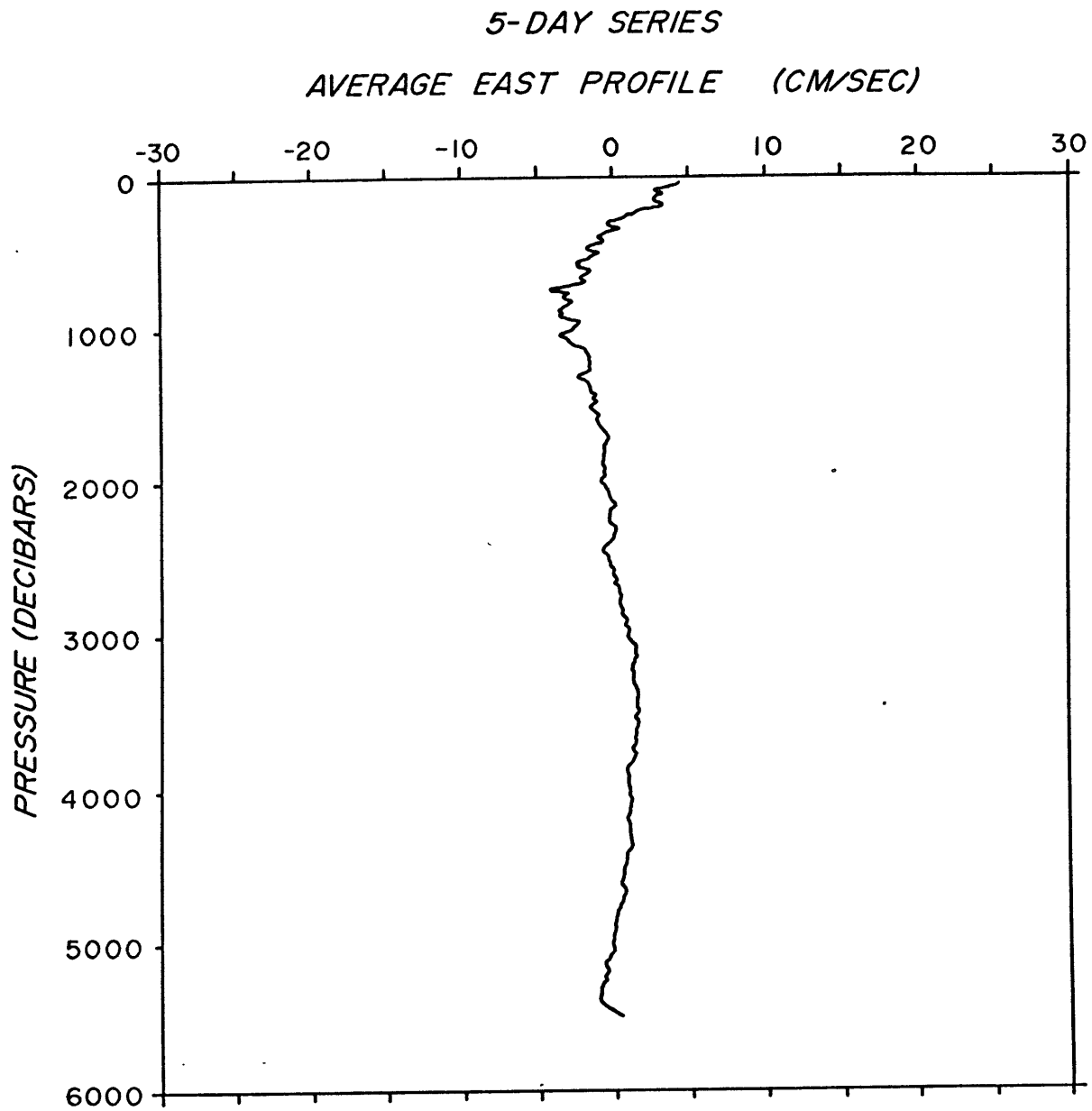


Figure 4. Average profile of the east velocity component during the five-day time series.

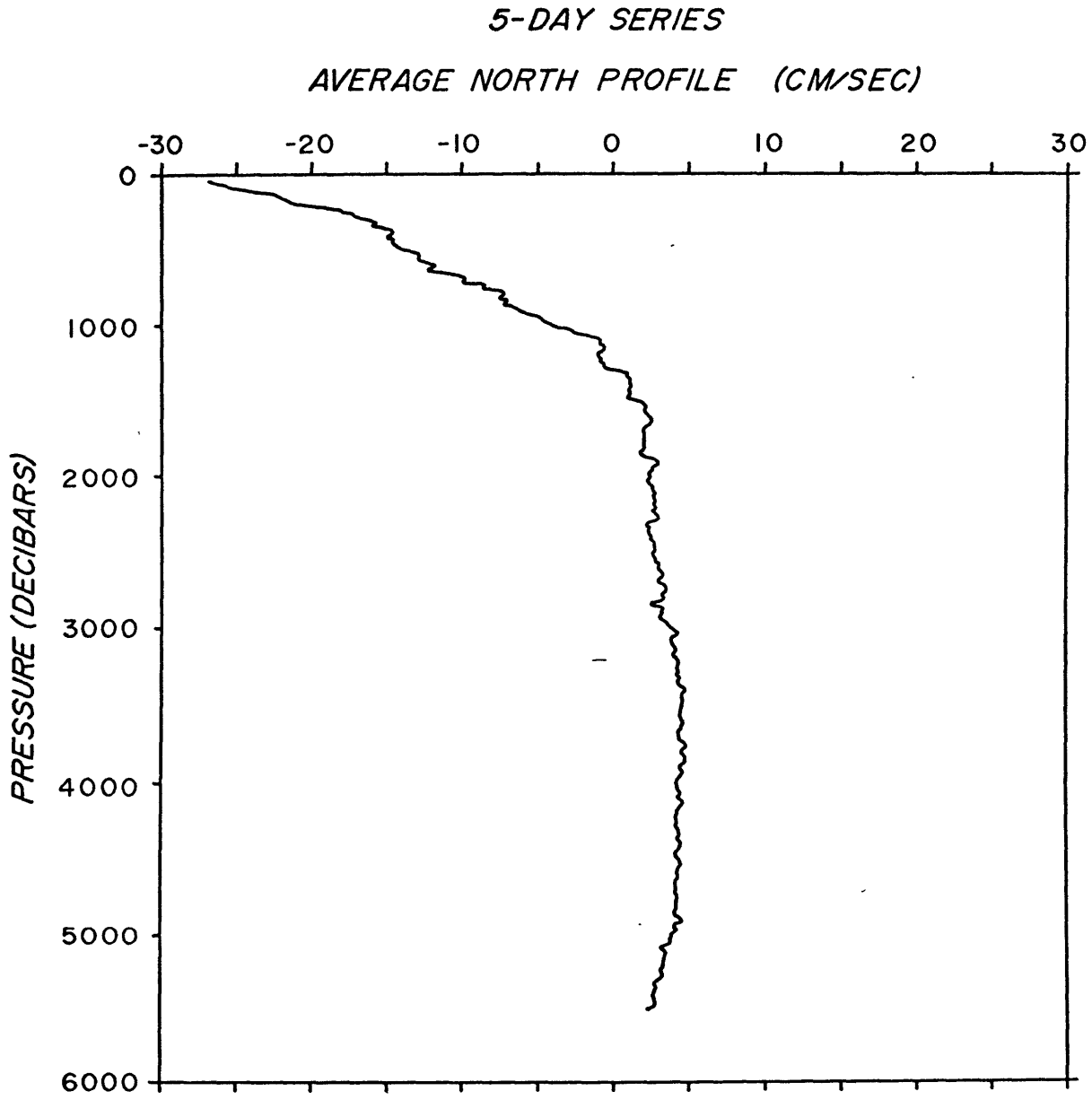


Figure 5. Average profile of the north velocity component during the five-day time series.

400 dbar, and increases slowly from about 4500 dbar to the bottom. The vertical shear of a geostrophic flow is proportional to the horizontal density gradient. It is reasonable to expect that the shear flow has caused the density field to distort in such a manner that the horizontal density gradient at a point is proportional to the vertical density gradient at the same point. Keeping in mind the fact that we have assumed the low-frequency flow to be in geostrophic balance, the above would seem to be a reasonable explanation of the observed decrease in shear of the mean flow at 400 dbar and of the increase in this shear as the bottom is approached.

c.) High-frequency velocity components in the upper 2.5 km as a function of time

From the 20 high-frequency profiles in the five-day time series, (that is, the profiles obtained after the mean velocities of Figures 4 and 5 have been removed), contour plots of east and north velocity components have been made (Figures 6 and 7). These plots show how various structures in the horizontal velocity field evolve as time progresses. This evolution appears as changes in the depth and size of individual features. Before discussing the significance of these plots, a few comments on their construction should be made.

First, the distribution of profiles in time is not uniform. In particular, there are relatively large gaps in time between 224D and 226D, and between 228D and 230D. Between these two pairs of drops the profiler had to be used for inter-comparison drops with

CONTOURS OF ZERO EAST VELOCITY COMPONENT

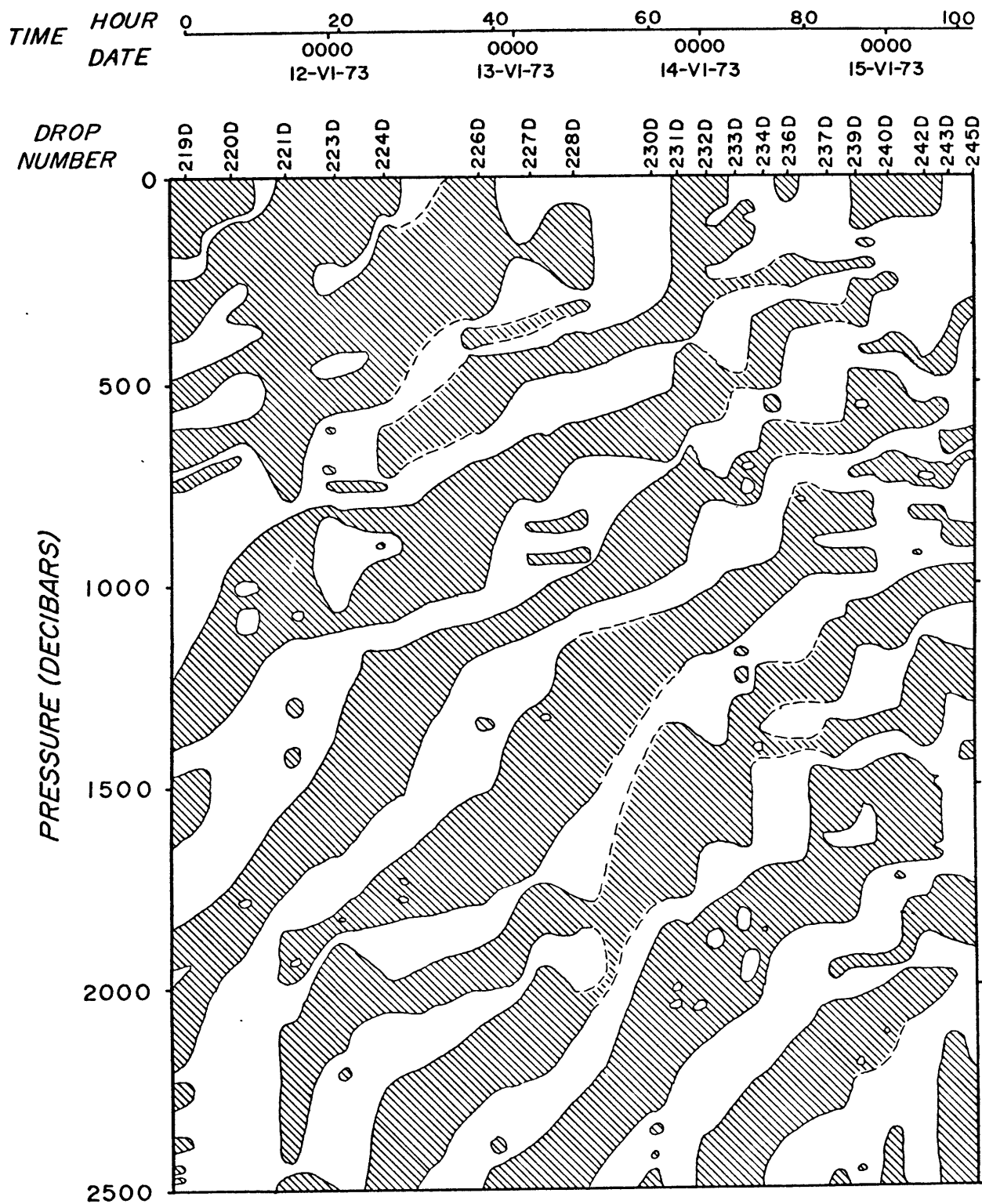


Figure 6. Contours of the east velocity component during the five-day time series. Negative east components are indicated by hatched regions.

CONTOURS OF ZERO NORTH VELOCITY COMPONENT

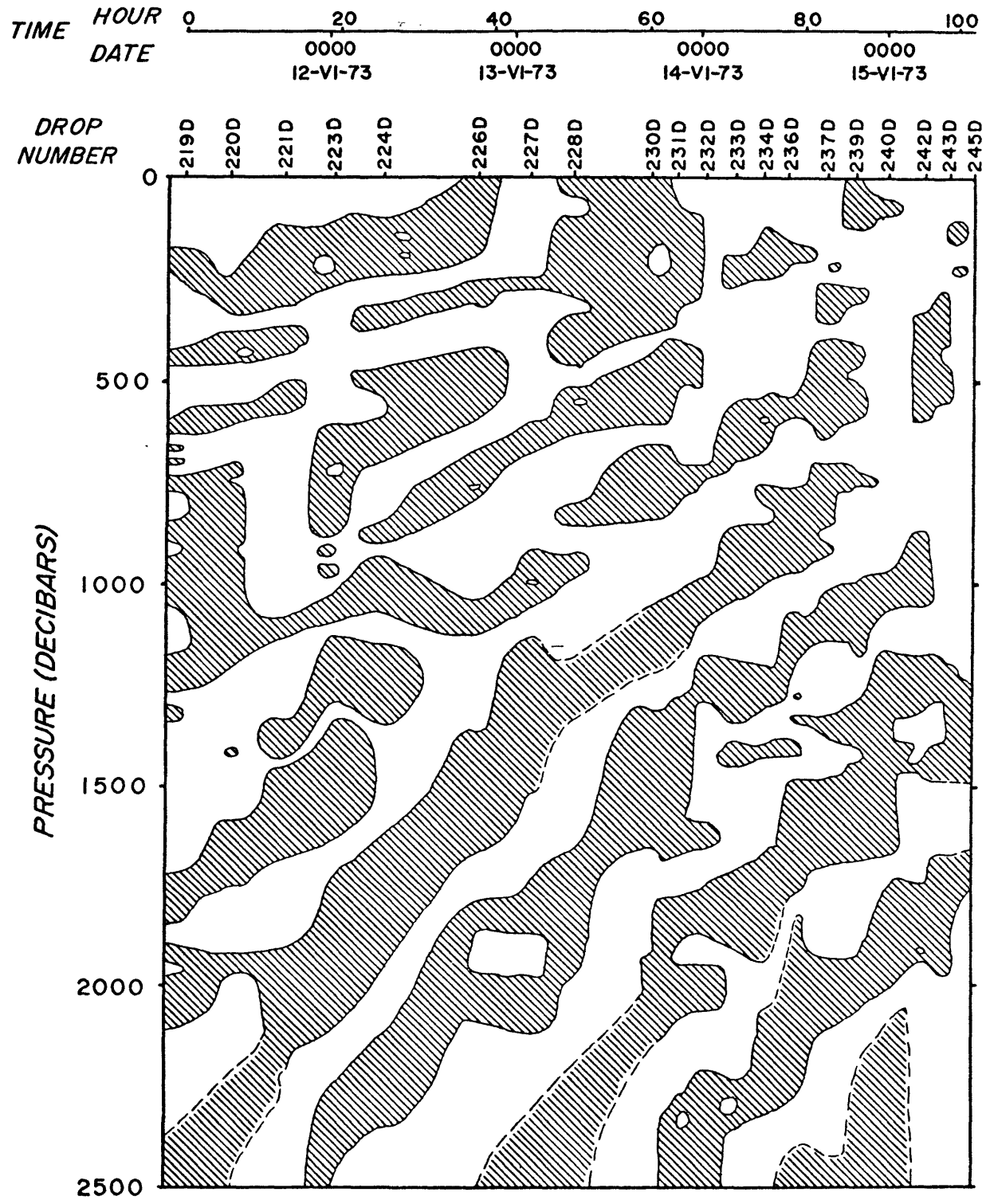


Figure 7. Contours of the north velocity component during the five-day time series. Negative north components are indicated by hatched regions.

other vertical profilers, and these inter-comparison drops were not done at the central mooring. Hence, gaps in the time series resulted. Also, the time interval between profiles in the second half of the series (after 2300) is generally less than it is for profiles in the first half. This uneven time distribution allows some regions of the plots to be contoured more easily than others.

Second, only the 0 cm/sec contour line is shown. Since the main intent in drawing the contour plots was to attempt to see vertical phase propagation of the near-inertial waves, a more detailed contouring was not required. Regions with negative velocity components are indicated by oblique hatching in Figures 6 and 7.

Finally, features for which contouring was ambiguous are denoted by dashed-line contours. There are two main reasons for this ambiguity. One is that as the depth increases, the overall energy level of the profiles decreases (see Figure 8). Thus, at depths of 2000 dbar to 2500 dbar, the true behavior of the zero-crossing lines becomes clear. Below 2500 dbar it is very difficult to draw contours with any confidence. The other reason is that, even at shallow depths, certain profiles have regions where a velocity component is close to zero without being clearly positive or negative. In cases where it appeared that structures on either side of this ambiguous region were clearly negative, dashed-line contours were used to join these negative-velocity-component features together. In other cases, there are regions on one drop which are clearly positive, while adjacent drops have

negative structures at the same depth. Such a case occurs at 500 dbar, around drop 242D in the contour plot for the north component. In these cases, no attempt was made to join adjacent negative-velocity-component features. Taking note of these difficulties, we can now point out some of the significant features in these plots.

Perhaps the most striking characteristic is the tendency for regions of negative velocity to move upward in time. If we assume that we can connect contours through regions where a velocity component is not clearly positive or negative, then most of the structures with negative velocity can be followed across much of the 103 hours over which the time series lasted. If, on the other hand, we assume that this connecting of structures is not valid, these negative-velocity regions will be divided into a series of "hot-dogs," with gaps of weakly positive velocity in between. In either case, the upward motion is evident.

In a few cases, features do appear to move downward in time. An example occurs at about 1000 dbar in the north plot, around drop 228D. It should be noted that this occurs in a region where the profiles are widely spaced in time, and the contouring there is not clear.

Several other points can be made concerning these two figures. First, if we follow the negative-velocity-component structures as they move upward in time, we see that, at a given depth, it usually takes about a day for two successive negative-velocity zones to pass through a given depth. This indicates that these

structures have a period of about a day, which is near the local inertial period at this latitude.

Second, if Figures 6 and 7 are overlaid, it is found that, in general, negative-velocity-component zones in the east plots occur at depths which are somewhat greater than the depths for the corresponding zones in the north plots. In other words, the east and north velocity components are not in-phase with respect to depth.

Third, the speed with which the negative-velocity-component zones move upward is about 2 mm/sec at 500 dbar, and this speed increases to about 6 mm/sec at 2000 dbar. We will consider these observations in more detail in later chapters.

d.) The average perturbation kinetic energy profile, and a smoothed profile of Brunt-Väisälä frequency

The 20 high-frequency profiles (with vertical averages and the low-frequency or "geostrophic" shear flow removed) were then used to calculate profiles of high-frequency, or "perturbation," kinetic energy. This was done for each profile simply by squaring the horizontal velocity values at each depth. These horizontal kinetic energy profiles were then averaged, at each depth, over the 20 drops and a mean kinetic energy profile resulted. This profile is shown in Figure 8. To simplify plotting, this mean, high-frequency, horizontal kinetic energy profile was averaged in the vertical by taking centered averages 50 dbar long around the points 50 dbar, 100 dbar, 150 dbar, and so on. Plotted along with the

MEAN PERTURBATION KINETIC ENERGY

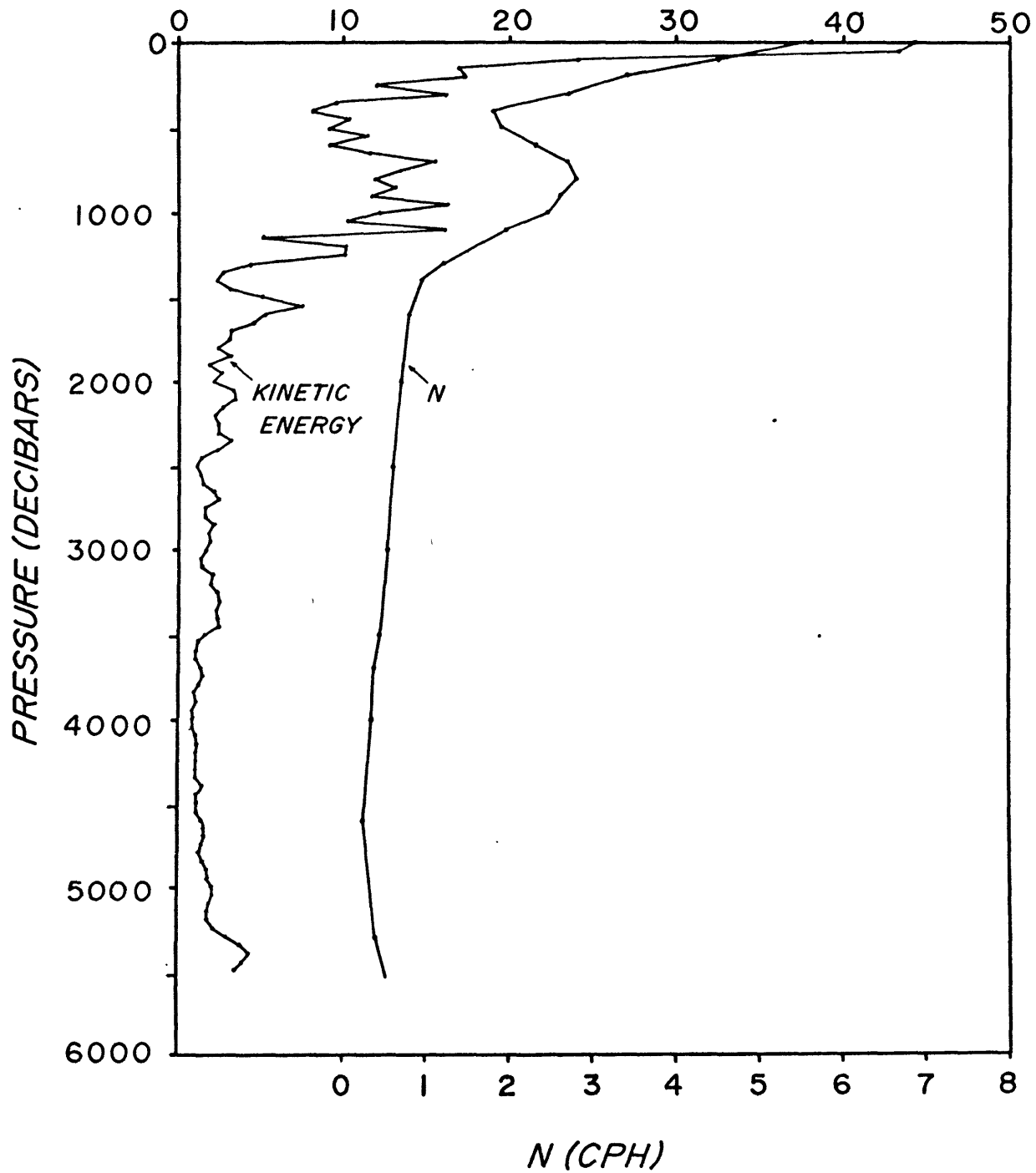
KINETIC ENERGY (ERGS/CM³)

Figure 8. Average profiles of high-frequency horizontal kinetic energy and Brunt-Väisälä frequency.

mean horizontal perturbation kinetic energy profile of Figure 8 is a smoothed Brunt-Väisälä frequency profile, obtained from CTD (conductivity-temperature-depth) stations made at roughly the same time and location as the time series. Because of difficulties with measuring velocities by EMVP near the surface (to depths of about 70 dbar), the points at 0 dbar and 50 dbar, showing rather high kinetic energies, are probably not accurate.

It is possible to calculate an error bar for Figure 8. We assume: the variance of the noise signal is $0.25 \text{ cm}^2/\text{sec}^2$ for either velocity component (Appendix C); noise at a given depth is uncorrelated with the signal and is uncorrelated between profiles, but the noise of points in the 50 dbar averages may be correlated as may the noise in the east and north velocity components. The contribution of the noise (if it is Gaussian) will then, for each point in Figure 8, be distributed as a Chi-square random variable with (at least) 19 degrees of freedom (Jenkins and Watts, 1969). The result of applying the Chi-square distribution law is that the difference between the measured and actual kinetic energy may be expected to be between .18 and .43 erg/cm^3 95% of the time (the measured kinetic energy being greater than the actual kinetic energy). This error estimate has not been plotted in Figure 8, since it is rather difficult to see (it is about three times the width of the line depicting the kinetic energy profile). We emphasize that this error estimate only takes into account instrumental noise. It does not take into account other sources of error, such as

contamination of the high-frequency profiles due to leakage of high-frequency energy into the low-frequency profiles (Figures 4 and 5).

We see from Figure 8 that the profiles of mean horizontal perturbation kinetic energy and mean Brunt-Väisälä frequency are very similar. The horizontal kinetic energy decreases from the surface down to about 400 dbar, increases in the main thermocline to about 1000 dbar, and then steadily decreases down to about 4500 dbar. This parallels the behavior of the Brunt-Väisälä frequency. It is interesting to note that while the Brunt-Väisälä frequency slowly increases from about 4500 dbar to the bottom, the mean kinetic energy profile increases similarly to about 100-150 dbar off the bottom, but then decreases again. This near-bottom decrease of energy may be indicative of the presence of a bottom boundary layer. The possible existence of a bottom boundary layer will be considered in more detail in Chapter IV.

We recall that the time series lasted for only 103 hours. This means that the mean kinetic energy profile was obtained by averaging over approximately four wave cycles for the inertial waves. It is not surprising, then, that there is considerable structure in the mean kinetic energy profile. Presumably, if the time series of profiles were of longer duration, the average perturbation horizontal kinetic energy profile would follow the mean Brunt-Väisälä profile more closely, particularly in the main thermocline.

- e.) The stretching of the vertical coordinate and the normalization of velocity by the mean Brunt-Väisälä profile

Figures 6 and 7 suggest that the high-frequency motions observed are dominated by internal waves of near-inertial period which are moving vertically through the water column. An important quantity which could be calculated from the high-frequency profiles is the horizontal kinetic energy spectrum as a function of vertical wave number. However, the data on which we would like to perform these calculations (that data being the ensemble of profiles in the time series) is clearly a nonhomogeneous process. Figure 8 shows that the overall variance (or horizontal perturbation kinetic energy) of the high-frequency profiles is a function of depth. Also, an examination of Figure 3 shows that the most energetic waves have vertical length scales which appear to be shorter in the thermocline than in the deep water. This means that the statistical properties of the wave field are functions of the Brunt-Väisälä frequency, which in turn is a function of pressure. Some method must be found which will at least partially convert the process represented by the ensemble of profiles into a homogeneous one. Figure 8 gives an idea of the method to be used. Since the horizontal kinetic energy tends to follow the mean Brunt-Väisälä profile, we could make the variance more uniform with depth by normalizing the horizontal velocity at a given depth with the square root of the Brunt-Väisälä frequency at that depth. But this type of normalization is what would be expected if the waves were obeying a WKB approximation (Phillips, 1966), since in this approximation the

horizontal velocity components of an internal wave are proportional to $(N)^{1/2}$, where N is the local Brunt-Väisälä frequency. Therefore, we chose to normalize the high-frequency velocity profiles using:

$$u^*(\tilde{z}) = u(\tilde{z}) / (N(\tilde{z})/N_0)^{1/2} \quad \text{II-1}$$

where u is an original velocity component, u^* is a normalized velocity component (both functions of pressure, \tilde{z}), $N(\tilde{z})$ is the Brunt-Väisälä frequency at pressure \tilde{z} and N_0 is a reference Brunt-Väisälä frequency, $N_0 = 3$ cph. N_0 has been given this value to facilitate comparison with theoretical vertical wave number spectra presented later (see Chapter V).

We have also pointed out that the scale of the dominant waves appears to change, being shorter in the main thermocline than in the deep water. This is also in accord with the WKB approximation, which predicts that the vertical wave length of an internal wave should be shorter in regions of greater N . Thus, it is also possible to use the WKB approximation to normalize wave lengths in the vertical. This has been done by stretching the pressure coordinate according to the following differential law:

$$\Delta \tilde{z}^* = \left(\frac{N(\tilde{z})}{N_0} \right) \Delta \tilde{z} \quad \text{II-2}$$

where \tilde{z} is the original pressure coordinate, and \tilde{z}^* is the stretched pressure coordinate.

Figure 9 gives \tilde{z}^* as a function of \tilde{z} , where \tilde{z} is in decibars and \tilde{z}^* is in "stretched decibars." Below about 2000 dbar, $\tilde{z}(\tilde{z}^*)$ is approximately a straight line. This, along with the fact that the high-frequency perturbation kinetic energy is roughly constant with depth below 2000 dbar, indicates that vertical wave number spectra of the profiles below 2000 dbar could be approximately calculated without use of the above normalization and stretching procedures. But to include the thermocline in these calculations requires the use of the above procedures.

Figures 10 and 11 show an example of a profile which has had the above procedures (equations II-1 and II-2) applied to it. Figures 10 and 11(a) show the velocity profile 219D as it was originally obtained. Figures 10 and 11(b) show the same profile after the "geostrophic" shear flow has been removed. Finally, Figures 10 and 11(c) show 219D after the above procedures for stretching and normalizing the profile have been used. With the exception of values in the top 100-200 stretched decibars, these profiles present a much more uniform appearance than do the profiles of the east and north components of 219D before stretching and normalizing. The departure from uniformity in the top 200 stretched decibars could be explained either by the fact that the WKB approximation breaks down near the surface, where N is changing rapidly, or by the fact that the shear of the mean horizontal velocity increases near the surface. This shear is not taken into account by the above WKB normalization.

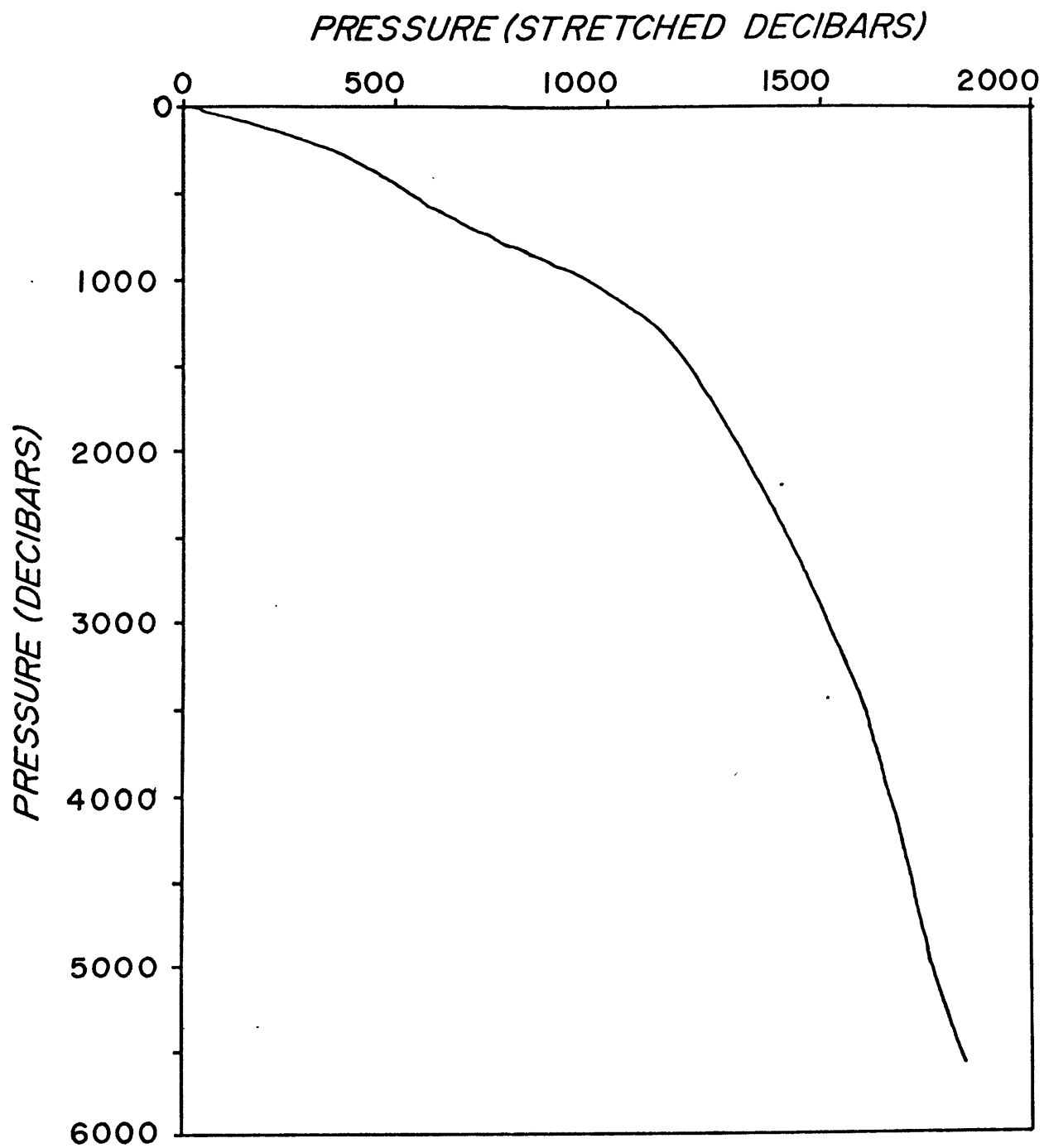


Figure 9. Stretched and unstretched vertical pressure coordinates.

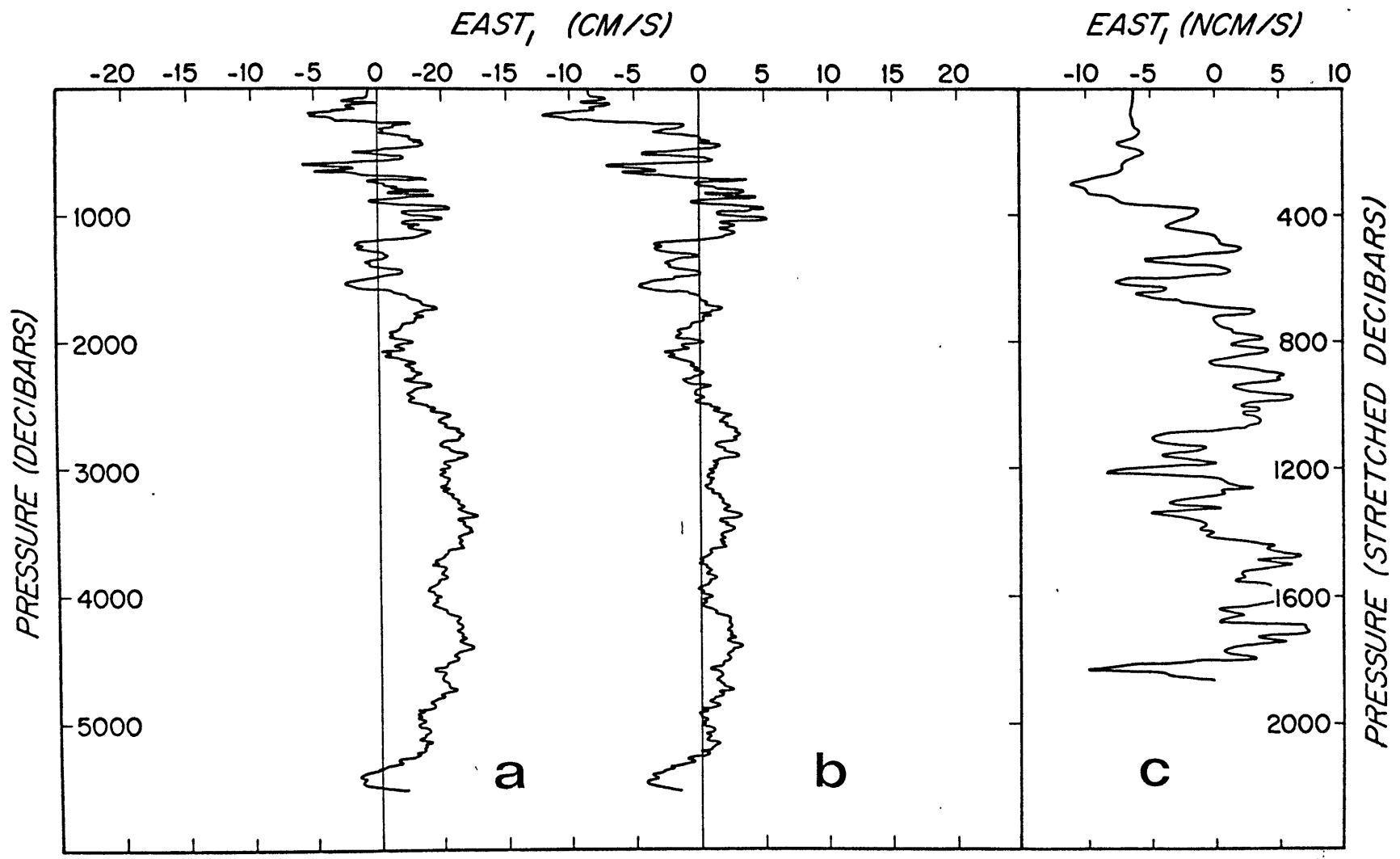


Figure 10. East component of profile 219D as originally obtained (a), after removal of the mean profile (b), and after stretching and normalizing (c).

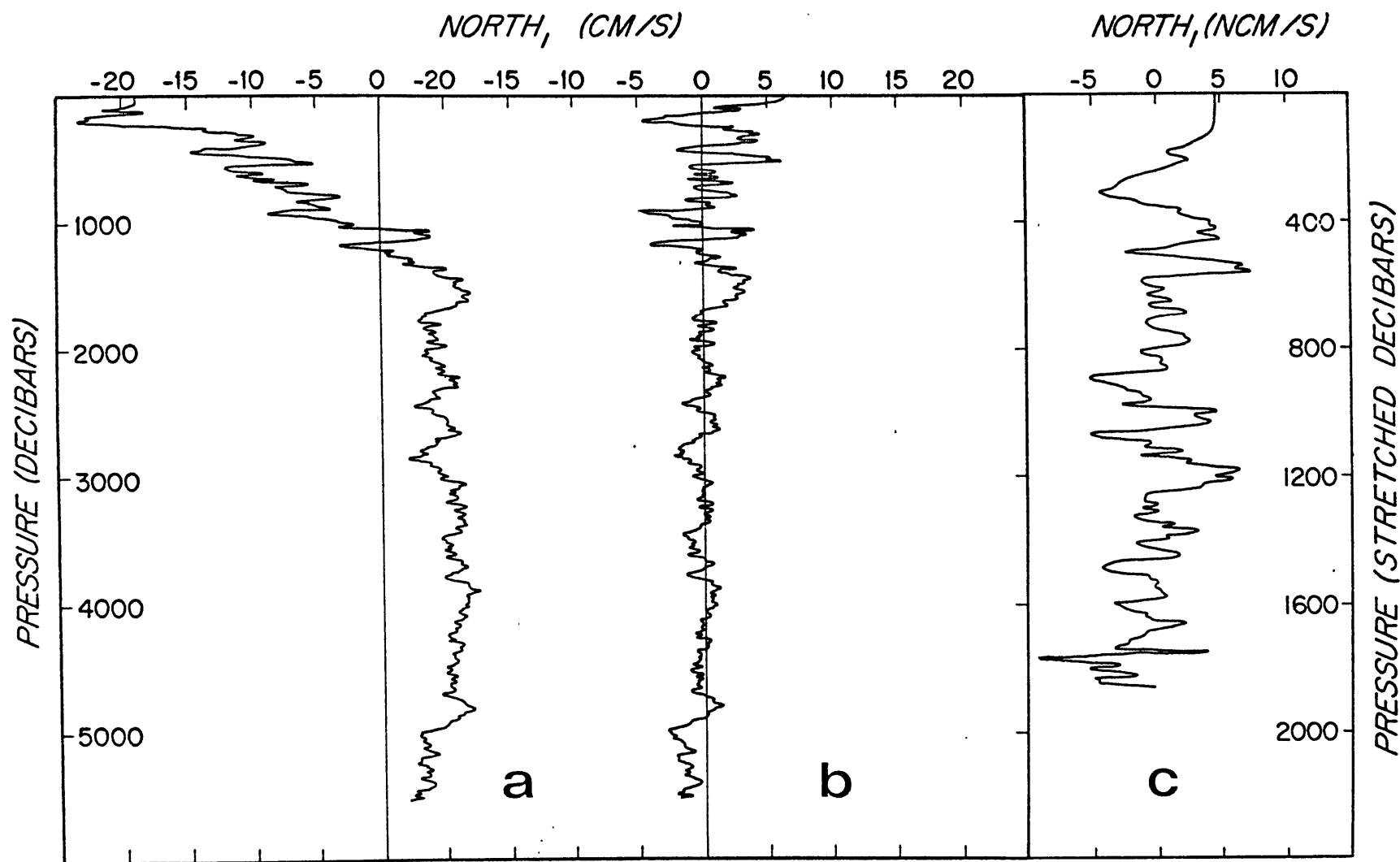


Figure 11. North component of profile 219D as originally obtained (a), after removal of the mean profile (b), and after stretching and normalizing (c).

f.) Spectral decomposition of stretched profiles

The time series of profiles is now in a form (the stretched and normalized profiles, such as 219D in Figures 10 and 11(c)) in which the vertical wave number spectrum of horizontal high-frequency kinetic energy can be calculated. We now describe and present several different types of spectra which have been obtained.

The first type, shown in Figure 12, is the simple autospectrum, or the total energy of the east and north components as a function of stretched vertical wave number. For this spectrum, a subset of nine down profiles out of the original 20 was selected. The only reason for this selection was that some profiles have better data near the surface than others. The EMVP quite often does not obtain accurate velocity values for the first 50-70 dbar below the surface. Since the WKB procedure described above tends to weight values near the surface more heavily than values in deeper water, it was important to choose those stretched profiles which have the best data near the surface. Thus, the best nine down profiles were chosen for the calculations. The top 50 dbar in the stretched profiles were also ignored when calculating the spectrum. This further reduced the influence of near-surface measurement errors. The 95% confidence limits were calculated using an assumed 36 degrees of freedom (Jenkins and Watts, 1968). Each final spectral estimate is formed by averaging the original estimates over four adjacent wave number bands in each profile, and then averaging over the nine profiles. This would give 72 degrees of

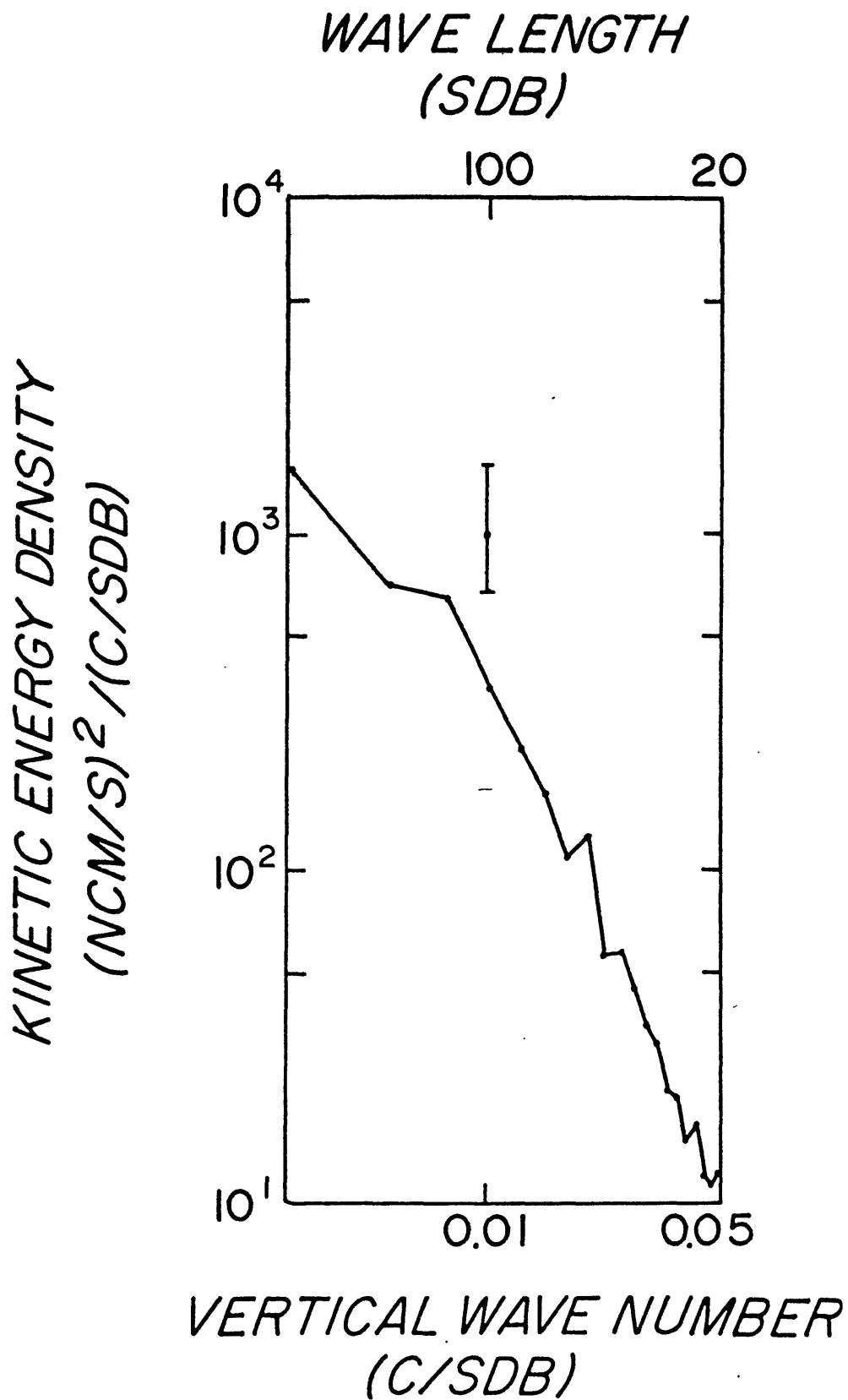


Figure 12. Total spectrum (east and north energy) for 9 down profiles.

freedom to each estimate, if east and north velocities are statistically independent. However, Figure 13 indicates that the east and north velocity components are not independent. Therefore, 36 degrees of freedom appears to be more realistic.

The somewhat unusual units in the spectrum of Figure 13 arise because of the normalization by $N(\tilde{z})$. Thus NCM/S means "normalized cm/sec," and C/SDB means "cycles per stretched decibar." If m and m' are vertical wave numbers in the unstretched and stretched coordinates, respectively, then the relation between them is

$$m = \left(\frac{N(\tilde{z})}{N_0} \right) m' . \quad \text{II-3}$$

Normalized cm/sec are the units obtained when equation II-1 is applied to an original velocity profile.

The most interesting characteristic of the autospectrum is that at high wave numbers it has a slope of about -2.5 on a log-log plot. At smaller vertical wave numbers this slope decreases. This spectral shape will be compared in Chapter V with a theoretical vertical wave number spectrum derived by Garrett and Munk (1972, 1975).

The second type of spectrum which is presented is a form which treats the horizontal velocity vector (u,v) as a complex vector, $u + iv$, (Gonnella, 1972; Mooers, 1973). At any vertical wave number, m' , the Fourier transform of u and v separately gives sinusoids for each component. These two sinusoids, taken together, will form an ellipse in the u, v plane, the position of the velocity

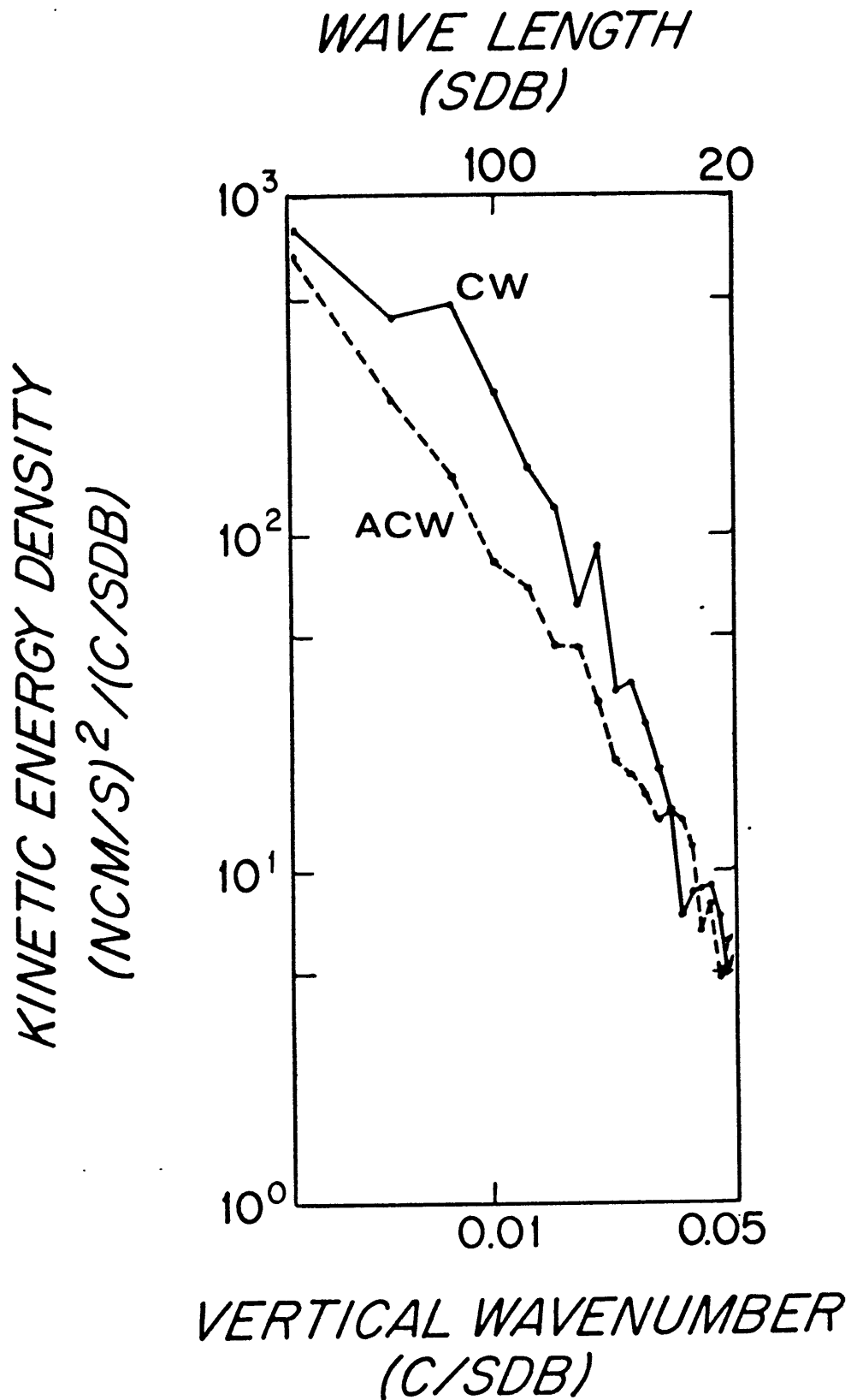


Figure 13. Clockwise (CW) and counterclockwise (ACW) spectra for 9 down profiles. In the text, CW is C(m') and ACW is A(m').

vector on the ellipse being a function of \tilde{z}^* , the pressure in stretched decibars (increasing downward). Since any ellipse can be represented as the sum of two complex vectors rotating in opposite directions, but with the same frequency, the complex vector $u_{m'} + iv_{m'}$ can be represented by

$$u_{m'} + iv_{m'} = u_+ e^{im'\tilde{z}^*} + u_- e^{-im'\tilde{z}^*} \quad \text{II-4}$$

where m' is always considered to be positive, and u_+ and u_- are complex. The energy spectrum is then given as a decomposition between the clockwise energy, $C(m')$, and the counterclockwise energy, $A(m')$, defined by:

$$C(m') = 1/2 \bar{R} u_- \cdot u_-^* ; \quad \text{II-5}$$

$$A(m') = 1/2 < u_+ \cdot u_+^* > \bar{r}, \quad \text{II-6}$$

where the brackets denote an average over realizations (in this case, profiles) and possibly over m' , the stretched vertical wave number. The total energy, $T(m')$, is given by

$$T(m') = A(m') + C(m'). \quad \text{II-7}$$

$T(m')$ is plotted in Figure 12, and $A(m')$ and $C(m')$ for the same nine drops are plotted in Figure 13.

Probably the most striking aspect of Figure 13 is the fact that clockwise energy is greater than counterclockwise energy over much of the stretched vertical wave number range. Only in the high wave number region of the spectrum, where the energy is relatively

low, do we find points where counterclockwise is greater than clockwise energy. This means that the waves are elliptically polarized in the clockwise sense, or in other words, that there is a distinct tendency for the horizontal current vector to rotate in a clockwise sense with depth, as seen by an observer looking down from above. This has important implications for the theory of internal waves, which will be discussed in the next chapter.

The third type of spectrum that we present here is simply that obtained by plotting the energy of the east and north components separately. This spectrum is given in Figure 14 for the same nine down drops as in Figure 12. We see that, in contrast to the difference in Figure 13 between the clockwise and counterclockwise spectra, Figure 14 shows that there is almost no difference between the energy of the east and north velocity components. This is an indication of isotropy; that is, that in the mean there is as much energy in the east-west as in the north-south direction.

Finally, we present in this section results of spectral calculations performed on nine up profiles from the same time series. It often happens that on a single drop (up and down) the down part will have good near-surface data while the up part will not. For this reason, the nine best up profiles chosen do not coincide with the nine best down profiles. These spectra are shown in Figures 15, 16 and 17. Each spectral estimate represents an average over four adjacent wave number bands and over nine up profiles. The major reason for performing the same calculations for up and down

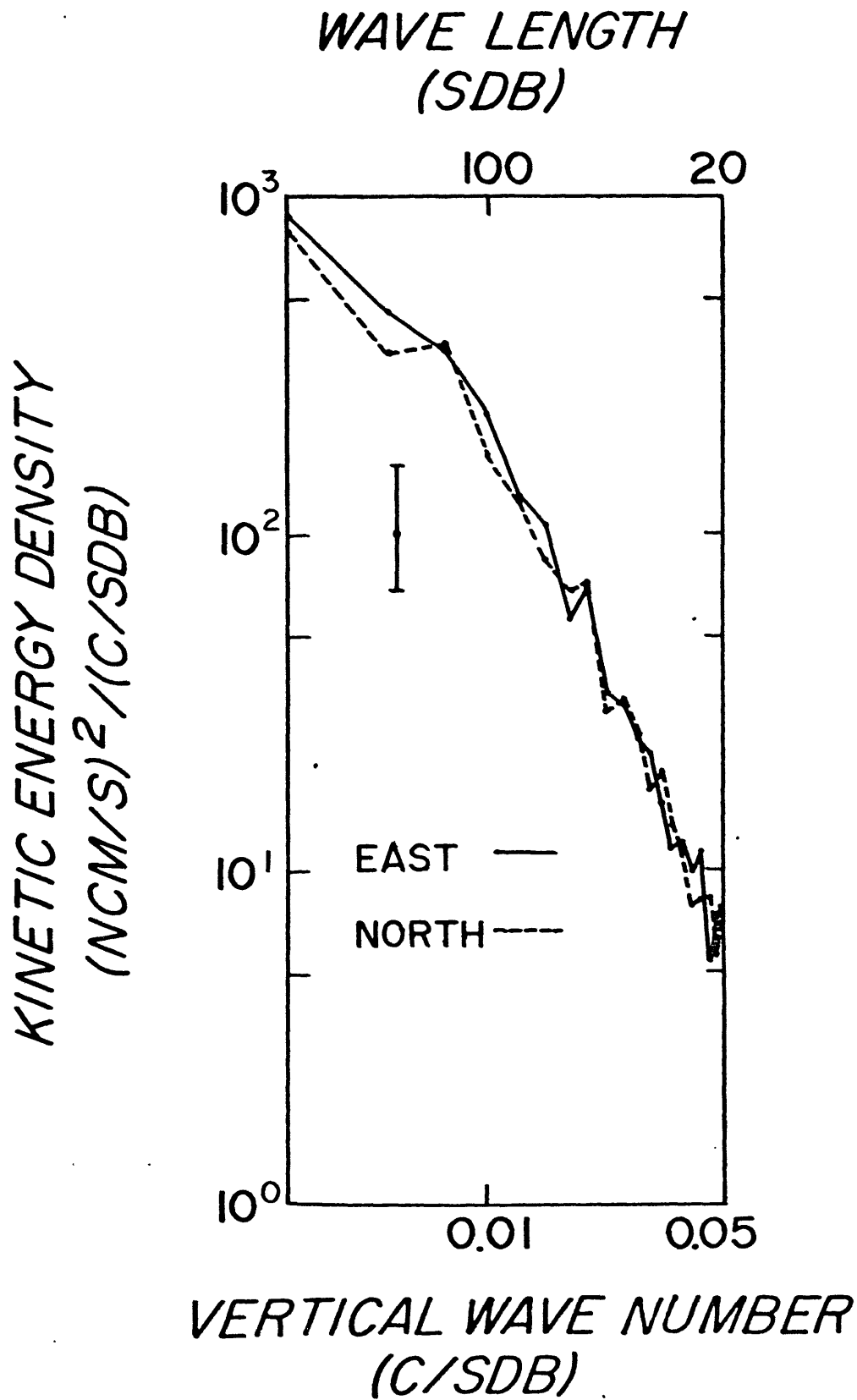


Figure 14. Spectra of east and north velocity components for 9 down profiles.

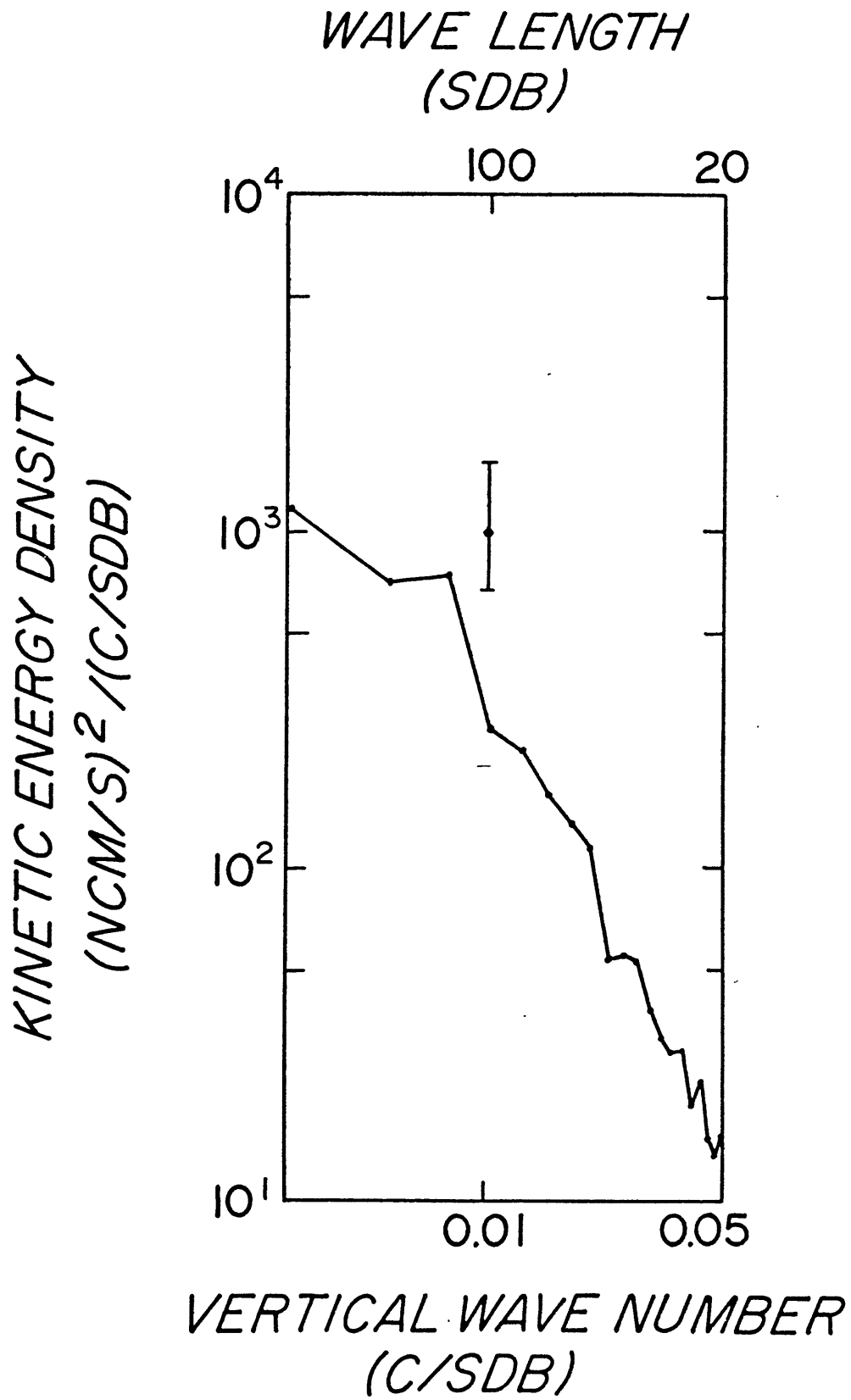


Figure 15. Total spectrum (east and north energy) for 9 up profiles.

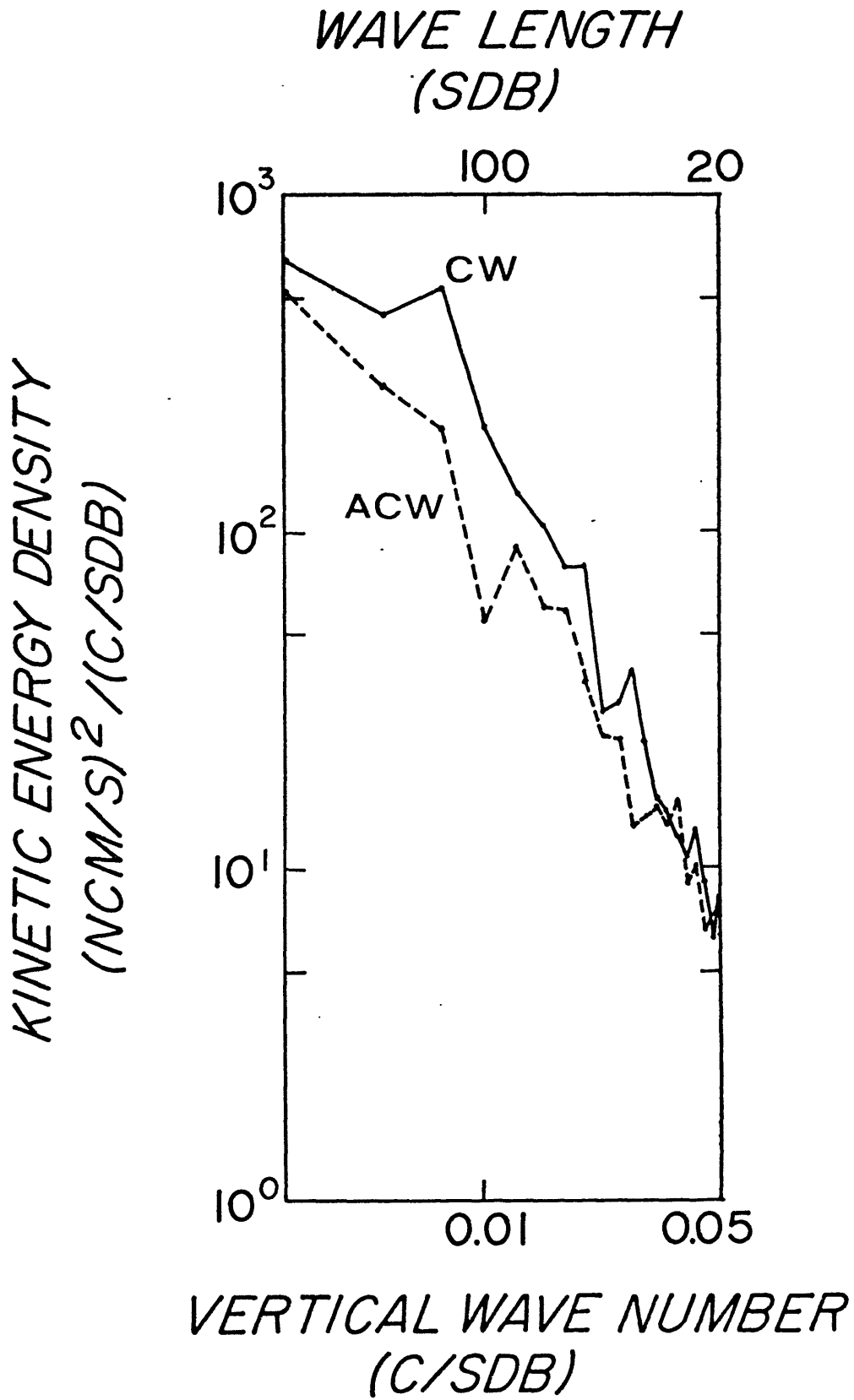


Figure 16. Clockwise (CW) and counterclockwise (ACW) spectra for 9 up profiles.

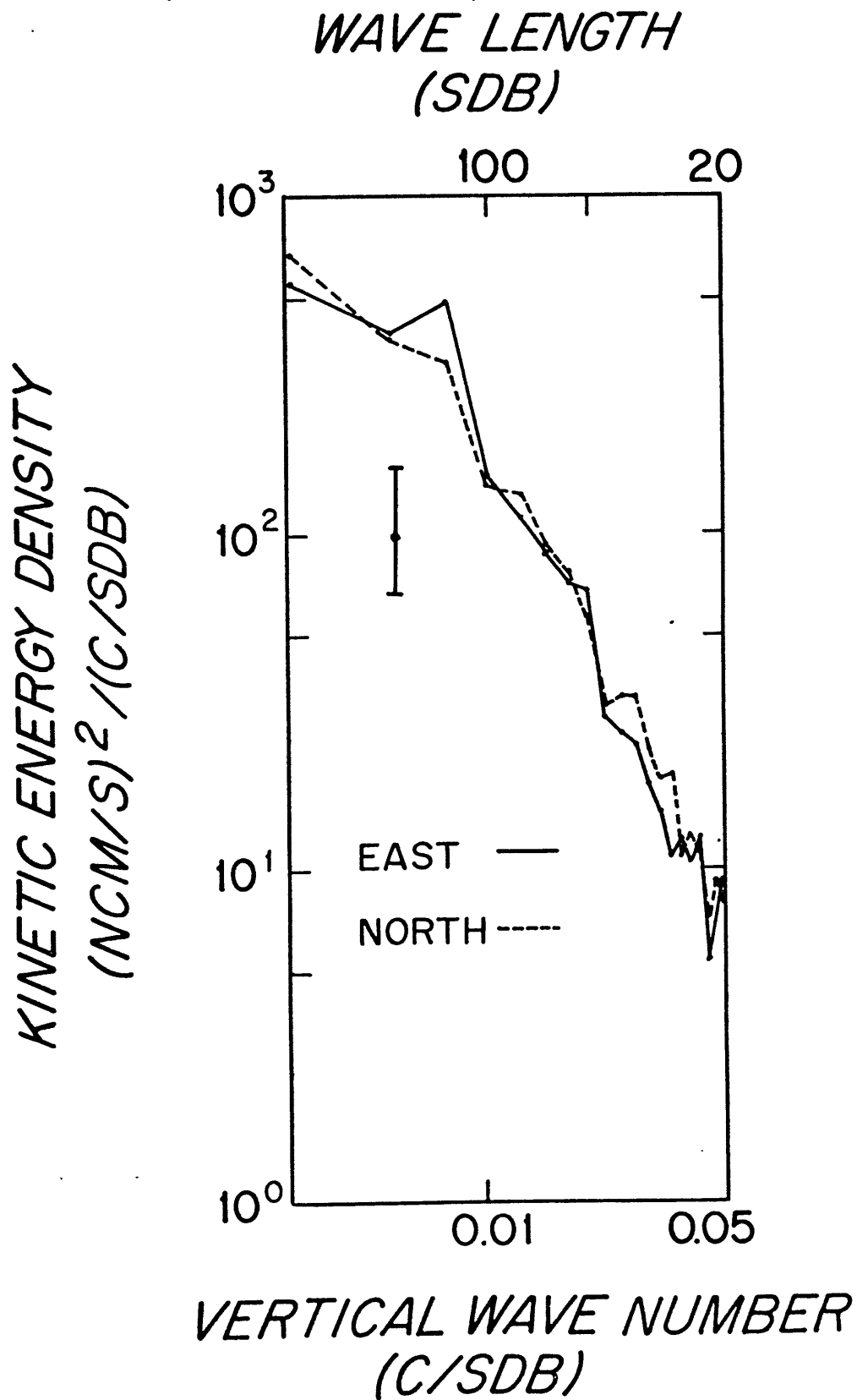


Figure 17. Spectra of east and north velocity components for 9 up profiles.

profiles was to show that there is very little difference between them (even though all of the same profiles were not used in both calculations). That the two computations are very similar can be seen from comparing Figures 12 and 15, 13 and 16, and 14 and 17.

The 95% confidence limits (with 36 degrees of freedom) have been included for the total vertical wave number spectra (Figures 12 and 15) and for the spectra of east and north velocity components (Figures 14 and 17). These confidence limits should be used with caution, however, since they strictly apply only to a white noise spectrum. The spectra presented in this section are clearly "red." Even though the original profiles were pre-whitened (by taking first differences) before applying the Fourier transform, and the above spectra were then produced by re-coloring the spectra obtained from the first-difference profiles, it is likely that the pre-whitening did not completely convert the profiles into ones with flat spectra. This means that the actual number of degrees of freedom could be less than 36. We have also not plotted confidence limits for the clockwise and counterclockwise spectra. The clockwise and counterclockwise energy estimates depend not only on the probability distribution of the autospectra for the east and north velocity components, but also on the probability distribution of the quadrature spectrum between east and north velocity components (Appendix D). Instead of deriving a theoretical estimate for the probability distribution of the clockwise and counterclockwise spectra, it is probably more important to point out that, as

indicated below, clockwise and counterclockwise spectra calculated from four-drop groups in the time series always showed that clockwise energy was greater than counterclockwise energy over most of the stretched vertical wave number range. Furthermore, while averaging the spectra of two four-drop groups together gave clockwise and counterclockwise spectra very similar to those of Figures 13 or 16, averaging three four-drop groups together did not appreciably change the spectra. This indicates that nine profiles are enough to give stable estimates of the clockwise and counterclockwise spectra.

Before the spectrum of Figure 12 was calculated, five preliminary autospectra were obtained by using four-drop groups in the series of 20 down profiles. That is, drops 219D-223D were used to obtain a spectrum, then drops 224D-228D, and so on. All four-drop groups showed a dominance of clockwise over counterclockwise energy. Each of the five preliminary spectra also showed a tendency for the energy to peak at vertical wave lengths of 100-130 sdb. Drops 230D-233D, in particular, showed a strong energy peak there. However, in some cases (for example, 219D-223D) this peak did not show up as clearly. The fact that the energy spectra did appear to have some dependence on time indicates that the spectra calculated from the nine best profiles out of the 20 will tend to smooth out peaks in the energy spectra.

On the other hand, it is clear that energy contributed at vertical scales of 100-130 sdb is an important part of the stretched

profiles. From Figure 3 we see that the most apparent visual variability in this profile occurs in the above range of vertical scales. (In the original pressure coordinate, the above scales correspond to 100-150 dbar in the main thermocline, and reach 1000 dbar in the deep water.) A comparison of drops 219D and 221D in the stretched vertical coordinate also shows that much of the "mirror-imaging" that occurs between these profiles is caused by waves with the above vertical length scales.

g.) Paired profiles

During the course of the time series experiment, several simultaneous paired profiles were made, using two EMVP's. These were done at separations of from 100 meters to about 15 kilometers. Figure 18 shows two profiles which were made simultaneously at a separation of 4.8 kilometers. Profile 235U was made to the south of profile 236U. It can be seen from this figure that many velocity features of 235U can be traced visually to corresponding features in profile 236U, although there is quite often a depth change between the more energetic features of profiles 235U and 236U. This indicates that: a.) many of the features observed in the two series (at least those with wave lengths greater than about 100 dbar) have a large ratio of horizontal to vertical length scales; and b.) the energetic features in the two profiles are not horizontal, but are slightly inclined. We will return later to a consideration of the inclination of velocity features between 235U and

VELOCITY PROFILES 235U & 236U
SIMULTANEOUS DROPS 4.8 KM APART

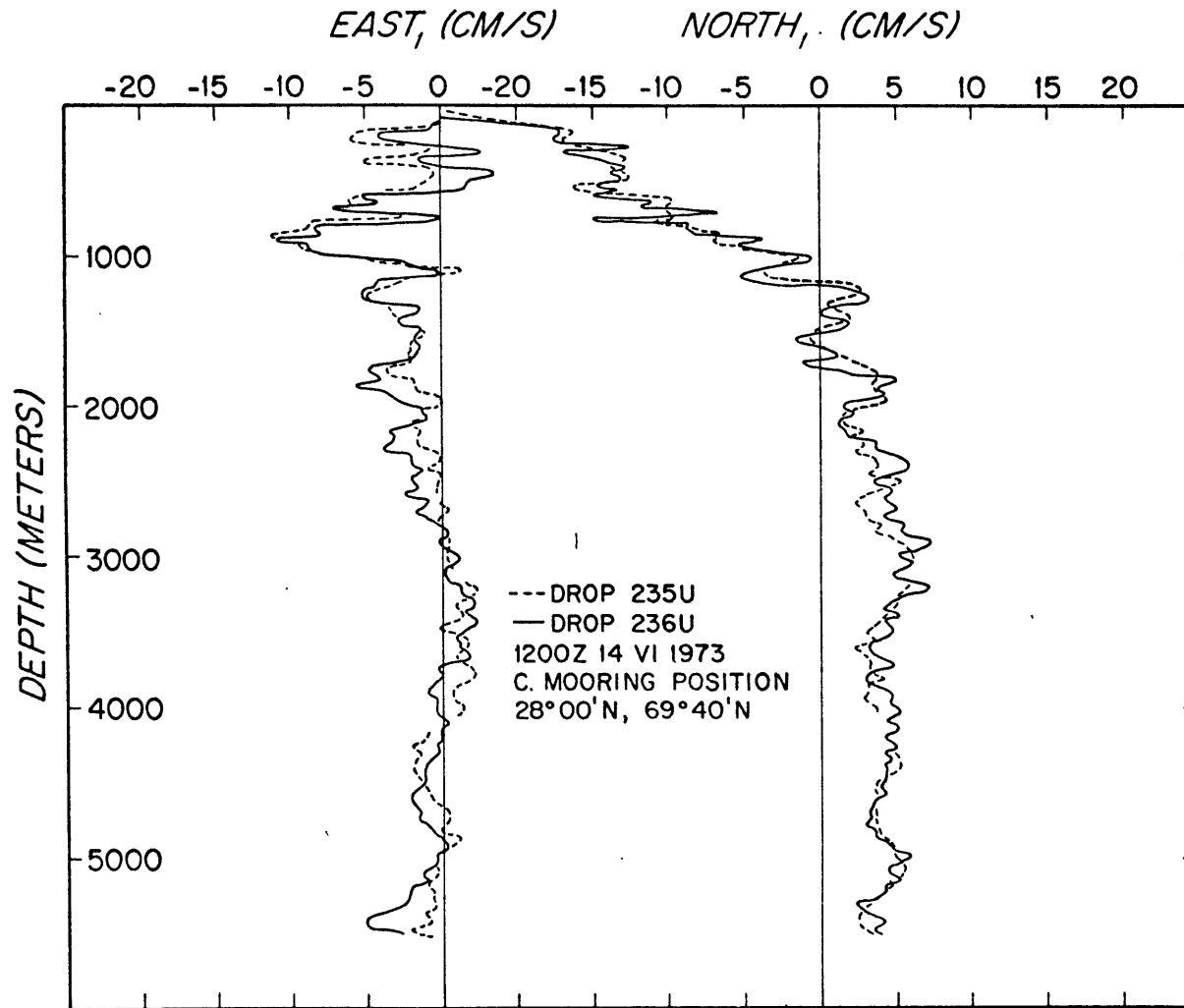


Figure 18. Simultaneous paired drops, 235U and 236U, separated horizontally by 4.8 km.

236U. We point out here, however, that waves with large ratios of horizontal to vertical wave lengths should, according to the results of Appendix B, be measured with small error by the EMVP.

Chapter III Vertical Polarization and the Vertical Propagation of Internal-inertial Waves

a.) Summary of data

Before going further, it will be useful to summarize the results of the previous chapter. Figure 3 indicates that high-frequency energy in the profiles is dominated by waves near the local inertial frequency. There is probably also energy contributed by diurnal and semidiurnal tides. Figures 6 and 7 show that the velocity structures associated with these inertial waves clearly move upward with time at the time series location. These two figures also show that the east and north components of horizontal velocity are usually not in-phase with depth, but that the east component lags behind the north component. This indicates that these near-inertial waves are polarized with depth, a fact which is born out by the clockwise and counterclockwise spectra of Figures 13 and 16. These spectra show that the waves are elliptically polarized with depth, and they show that this polarization is predominantly clockwise (the clockwise energy is greater than the counterclockwise energy over most of the observed wave number band). We note that the observed lag in Figures 6 and 7 between the east and north components also indicates that these waves are polarized clockwise with increasing depth. Finally, Figures 14 and 17 indicate that there is very little difference between the energy of the east component and that of the north component. We would now

like to see how the above observations may be related to internal wave theory.

b.) The vertical spatial behavior of horizontal internal wave velocity components

Expressions for the east and north, or u and v velocity components of a single propagating internal wave are given in the WKB approximation by:

$$\left. \begin{aligned} \bar{u} &= (\mp \omega k \mp i f l) \\ \bar{v} &= (\pm i k f \mp \omega l) \end{aligned} \right\} x A \frac{(N^2(z) - \omega^2)^{1/4}}{\omega(\omega^2 - f^2)^{1/2} (k^2 + l^2)^{1/2}} \\ x e^{\pm i \left(\frac{k^2 + l^2}{\omega^2 - f^2} \right)^{1/2} \int_z (N^2(z) - \omega^2)^{1/2} dz} x e^{i(kx + ly - \omega t)}$$

III-1

where A is the wave amplitude, and the coordinate system is chosen so that x is positive eastward, y is positive northward and z is positive upward. The coordinates \bar{z} and \bar{z}^* will be reserved for the vertical pressure coordinate (increasing downward) in decibars and stretched decibars, respectively. (The reader may refer to Chapter V for the derivation of these formulas.) In order to simplify these expressions, we rotate the coordinate system through an angle α as shown in Figure 19. In the new coordinate system:

$$\begin{aligned} \bar{u}' &= \bar{u} \cos \alpha + \bar{v} \sin \alpha ; \\ \bar{v}' &= -\bar{u} \sin \alpha + \bar{v} \cos \alpha ; \\ k' &= k \cos \alpha + l \sin \alpha ; \\ l' &= -k \sin \alpha + l \cos \alpha = 0 , \end{aligned}$$

III-2

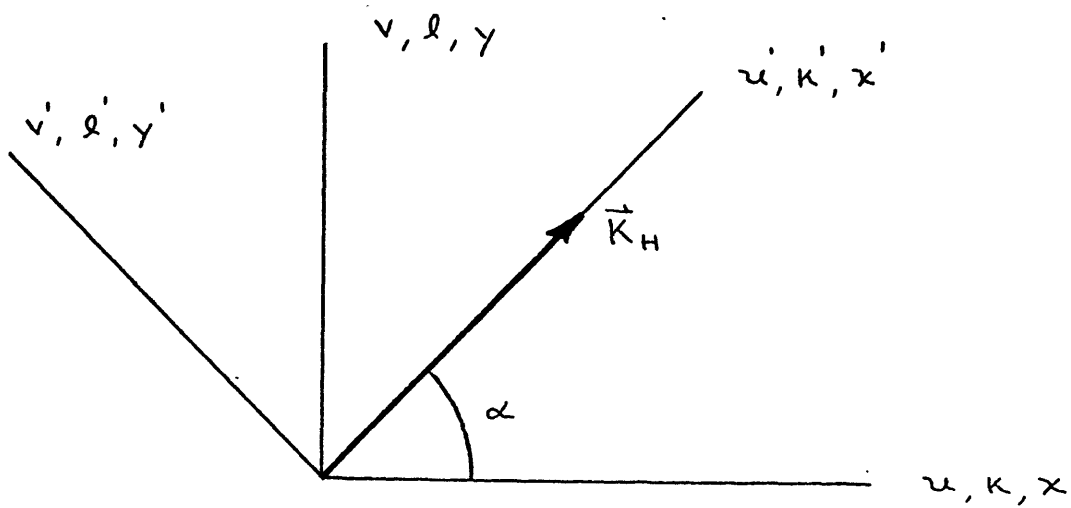


Figure 19. Horizontal coordinate rotation (see equations III-2).

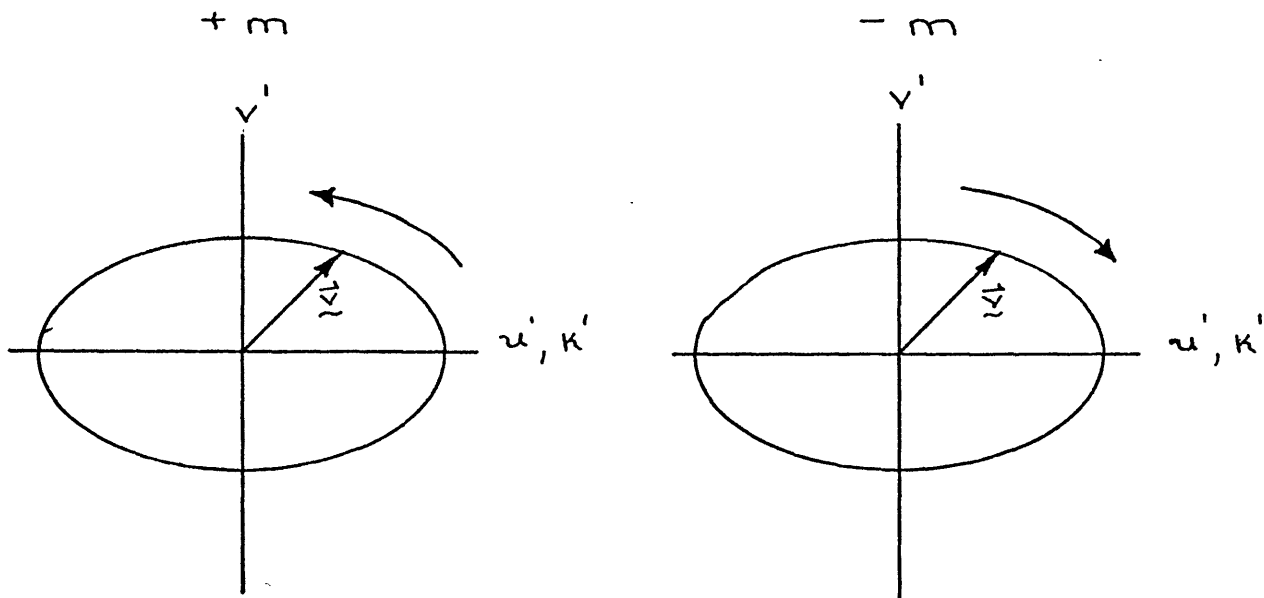


Figure 20. Direction of rotation of the horizontal velocity vector of an internal wave for positive and negative vertical wave numbers. The curved arrow shows the direction in which \vec{v} rotates with increasing z .

where

$$\cos\alpha = \frac{k}{\sqrt{k^2 + l^2}} ,$$

and

$$\sin\alpha = \frac{l}{\sqrt{k^2 + l^2}} . \quad \text{III-3}$$

In the new coordinate system, we have

$$\left. \begin{aligned} \bar{u}' &= \mp l \\ \bar{v}' &= \pm i \frac{f}{\omega} \end{aligned} \right\} \times A \frac{(N^2(z) - \omega^2)^{1/4}}{(\omega^2 - f^2)^{1/2}}$$

$$x e^{\pm i \left(\frac{k'^2}{\omega^2 - f^2} \right)^{1/2} \int_z (N^2(z) - \omega^2)^{1/2} dz} \times e^{i(k'x' - \omega t)} . \quad \text{III-4}$$

We let

$$\left(\frac{k'^2}{\omega^2 - f^2} \right)^{1/2} \int_z (N^2(z) - \omega^2)^{1/2} dz \approx m(z) \cdot z , \quad \text{III-5}$$

where $m(z)$, the local vertical wave number, is given approximately by

$$m(z) = \left(\frac{k'^2}{\omega^2 - f^2} \right)^{1/2} (N^2(z) - \omega^2)^{1/2} . \quad \text{III-6}$$

Note that $m(z)$ is a positive quantity. The choice of signs in the expressions for horizontal velocity determines whether the wave is

propagating upward or downward. Then

$$\left. \begin{aligned} \bar{u}' &= \mp 1 \\ \bar{v}' &= \pm i \frac{f}{\omega} \end{aligned} \right\} \times A \frac{(N^2(z) - \omega^2)^{1/4}}{(\omega^2 - f^2)^{1/2}} \times e^{i(k'x' \pm mz - \omega t)} \quad \text{III-7}$$

The horizontal component of the wave number vector, k' , is assumed to be in the direction of horizontal phase propagation, so $\omega > 0$. We note in passing that \bar{u}' and \bar{v}' are proportional to $N^{1/2}$, while $m(z)$ is proportional to N . This confirms the connection made in Chapter II, without proof, between the WKB approximation and the procedures used for stretching and normalizing the velocity profiles. Taking real parts of \bar{u}' and \bar{v}' :

$$\left. \begin{aligned} \text{Re}(\bar{u}') &= u' = \mp \cos(k'x' \pm mz - \omega t) \\ \text{Re}(\bar{v}') &= v' = \mp \frac{f}{\omega} \sin(k'x' \pm mz - \omega t) \end{aligned} \right\} \times A \frac{(N^2(z) - \omega^2)^{1/4}}{(\omega^2 - f^2)^{1/2}} \quad \text{III-8}$$

The upper signs are chosen if m is directed upward, and the lower signs are chosen if m is directed downward. A is assumed to be real. To observe the behavior of u' and v' as z varies, we set $x' = t = 0$. Then

$$\left. \begin{aligned} u' &= \mp \cos(\pm mz) \\ v' &= \mp \frac{f}{\omega} \sin(\pm mz) \end{aligned} \right\} \times A \frac{(N^2(z) - \omega^2)^{1/4}}{(\omega^2 - f^2)^{1/2}} \quad \text{III-9}$$

The two cases for the choice of upper or lower signs are shown in

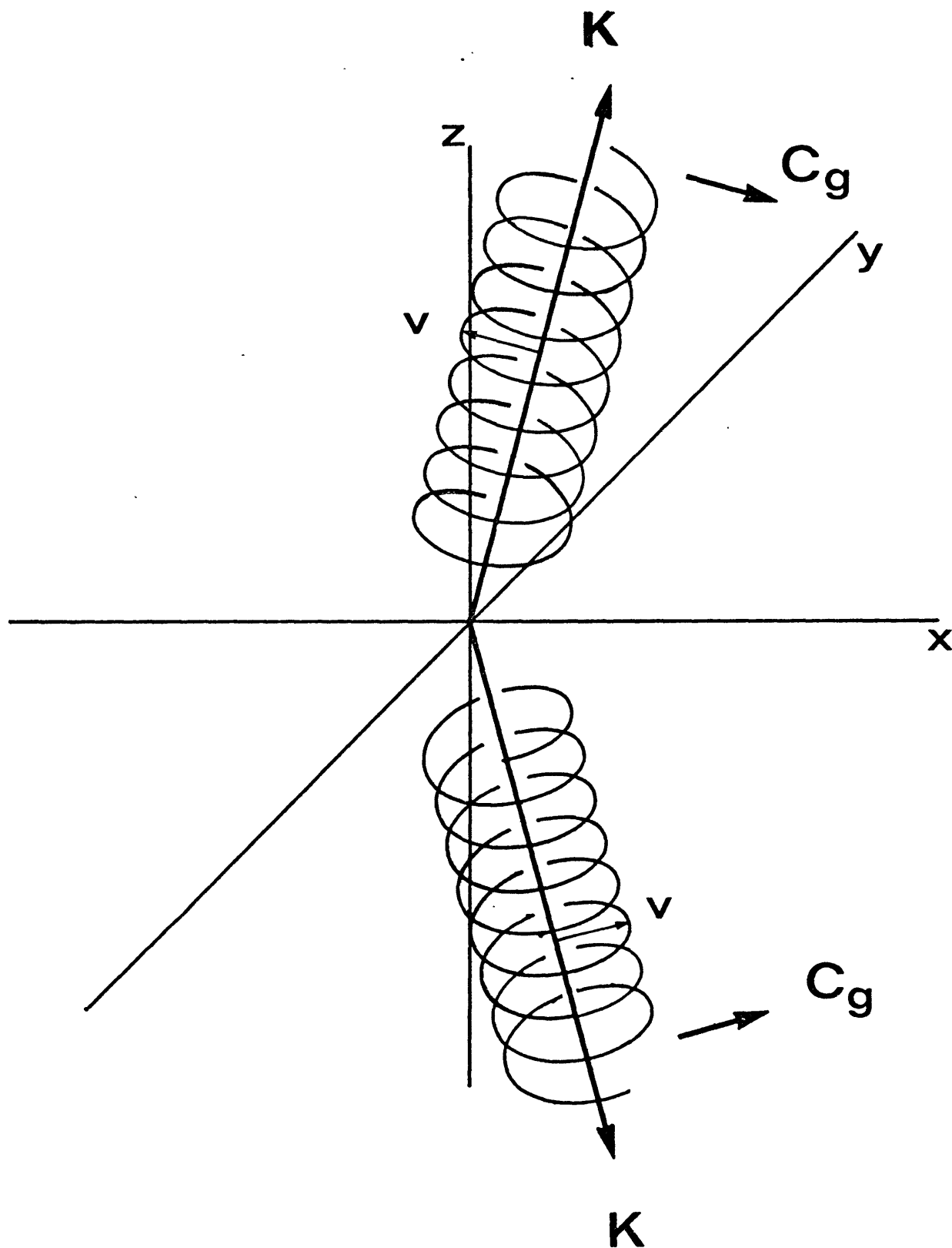


Figure 21. Propagation diagram for internal waves. \vec{C}_g is the group velocity vector, \vec{K} is the wave number vector, and \vec{v} is a vector representing water velocity.

Figure 20. We note that $\vec{x}' = \vec{v}' / (N^2(z) - \omega^2)^{1/4}$. The horizontal vector, \vec{v}' , is plotted in Figure 20 instead of \vec{v}' in order to remove variations in the horizontal velocity vector magnitude brought about by changes in $N(z)$. The ellipses represent hodographs of the horizontal velocity vector as z varies. As $\omega \rightarrow f$, the wave becomes circularly polarized. We note that although we have been writing simply A for the wave amplitude in the above expressions, the wave amplitude is more generally a function of vertical wave number, frequency, and α , the direction of horizontal phase propagation; that is, $A = A(m, \omega, \alpha)$. In the $+m$ case, the horizontal velocity vector rotates counterclockwise with increasing z , while in the $-m$ case, the sense of rotation is the opposite. The result is that there is a unique relation between the sign of m and the sense of polarization in the internal wave hodographs of Figure 20.

We can now relate the sign of $m(z)$ to the direction of the vertical group velocity component for internal waves. Figure 21 shows a propagation diagram for internal waves. The vector \vec{k} is the wave number vector for the wave and \vec{C}_g is the group velocity vector (or the direction of energy propagation).

For simplicity, only two wave number vectors have been shown, one pointing toward the sea surface (toward positive z) and the other pointing away from the sea surface: the dispersion relation gives

$$\omega^2 = N^2 \sin^2(\theta) + f^2 \cos^2(\theta), \quad \text{III-10}$$

where θ is the angle that the wave number vector, \vec{k} , makes with the z axis. For ω close to f , θ is small, and \vec{k} is almost vertical. For constant N , \vec{k} is also independent of depth. On the other hand, if N varies with depth, then θ and the vertical component, m , of \vec{k} also change with depth. If the wave propagation may be approximated by a WKB expansion, however, equations III-10 and III-11 remain true locally, except that m and N are now functions of z . The magnitude of the group velocity is given by:

$$C_g = \frac{1}{|\vec{k}|} \frac{\partial \omega}{\partial \theta} = \frac{(N^2 - f^2) \sin \theta \cos \theta}{|\vec{k}| [N^2 \sin^2 \theta + f^2 \cos^2 \theta]^{1/2}} . \quad \text{III-11}$$

The group velocity vector is perpendicular to \vec{k} and points away from the z axis if $N > f$, which it was everywhere in the water column during the time series experiment. The vector \vec{v} in Figure 21 is the water velocity due to the wave. Since the water is assumed to be incompressible, $\vec{k} \cdot \vec{v} = 0$ always. There is no dependence on horizontal direction in the above formulas, so the \vec{k} and \vec{C}_g vectors can be rotated about the z axis without change of frequency or magnitude of \vec{C}_g . We have also drawn two helices in Figure 21. These helices represent the path that the tip of the velocity vector, \vec{v} , makes as distance from the origin is increased along \vec{k} .

Looking down on this figure from above the z axis, it is readily seen that the sense of polarization of the wave (that is, the direction in which \vec{v} rotates with increasing depth) changes,

depending on whether \vec{k} is directed toward or away from the sea surface. For a vector \vec{k} directed toward the sea surface, the wave is polarized clockwise with increasing depth, while for a \vec{k} vector directed away from the sea surface, the wave is polarized counterclockwise with increasing depth. This is simply a restatement of the result expressed by equations III-8 and III-9.

We point out that polarization can be inferred easily from the behavior of internal waves in time. We assume we are observing at a fixed point within the ocean in the Northern Hemisphere. Then it is known that a velocity vector due to an internal wave propagating through that point will rotate in a clockwise sense with time, due to the influence of the Coriolis acceleration. Since the internal wave is assumed to be propagating along the direction of the wave number vector, \vec{k} , of Figure 21 (either toward or away from the sea surface), the waves have to be polarized as shown in the figure in order to give a velocity vector, \vec{v} , which rotates clockwise in time at a given point in space.

Now, Figure 21 also shows that if \vec{k} is pointed toward the sea surface, \vec{c}_g is pointed away from it, and vice versa. Therefore, if either the sense of wave polarization or the direction of the vertical phase propagation (the sign of m) can be determined, then the direction of the vertical component of the group velocity vector, and thus the direction of vertical energy propagation, can be found (Leaman and Sanford, 1975).

The data presented in Chapter II allows us to determine both the direction of the vertical component of \vec{k} (at least for the dominant waves) and the sense of wave polarization in the vertical. As already pointed out, the dominant waves in Figures 6 and 7 almost always appear to be propagating upward through the upper 2.5 kilometers of the water column. This indicates that the direction of phase propagation, or \vec{k} , for these waves is pointed toward the sea surface. If this is true, the above discussion shows that the waves should be polarized predominantly clockwise with increasing depth. Both the clockwise and counterclockwise spectra of Figures 13 and 16, and the fact that the east and north velocity components are out-of-phase in depth, with north leading, in Figures 6 and 7, show that the waves are in fact dominated by clockwise polarization.

The influence of the mean flow on the observed waves has so far been ignored. The depth dependent part of the mean flow profile has already been presented (Figures 4 and 5). Another depth independent component of the low-frequency profile may also exist, but its magnitude cannot be evaluated from EMVP data (Sanford, 1971). In order to evaluate a possible depth independent part of the mean profile, we have calculated the average horizontal current at the central mooring as measured by a current meter at 1513 dbar (1496 meters). The average horizontal velocity components over the interval of the profiler time series, as determined from the current meter record, are + 1.6 cm/sec to the west and + 2.5 cm/sec to the north. The magnitudes of the horizontal current

components at 1513 dbar in Figures 4 and 5 are ~ 1.5 cm/sec to the west and ~ 1.5 cm/sec to the north. This indicates that there is very little shift in the east component, while $\sim +1$ cm/sec should be added to the north profile to make the average north flow observed by the current meter and the profiler agree.

Since the wave number vector, \vec{k} , is not exactly vertical for waves propagating in the vertical, we expect that the advection of waves by the mean flow will cause an apparent vertical propagation. The amount and sign of this apparent propagation (upward or downward) depends on the direction of horizontal wave propagation relative to the mean flow. Figures 4 and 5 show that the main part of the mean flow is oriented north-south. Thus, for example, if the waves were propagating east-west, there would be little apparent vertical propagation due to the advection of waves past the observing point. On the other hand, if most of the waves were propagating northward (and upward), the advection would cause an apparent downward phase propagation to be added to the true upward phase propagation of the wave above 1500 dbar. In the absence of adequate information on the direction of horizontal phase propagation it is difficult to estimate the influence of the mean flow. There is some theoretical support for assuming that the near-inertial waves are propagating northward (Munk and Phillips, 1968). If this is, in fact, true, Figures 6 and 7 show that \vec{k} must be directed toward the sea surface: that is, the actual upward phase propagation of the waves is enough to overcome any apparent

downward propagation caused by advection. A strong indication that the observed waves are propagating upward can be found by examining Figures 4 and 5. It is known from tracking neutrally buoyant floats that the mean, or "low-frequency" flow is small at depths of around 1500 dbar (Voorhis, 1974). Figures 4 and 5 also show that, taking into account the shift in the north profile required to make the mean flow as observed by the profiler and current meter equal at 1513 dbar, the mean flow in the depth range 1400-1500 dbar is small (< 3 cm/sec). Therefore, there should be little advection of waves at this depth. However, Figures 6 and 7 show that the waves are moving upward at this depth. In fact, the rate of upward motion is greater at 1500 dbar than it is at lesser depths. We note that the sense of polarization is not affected by the advection of waves past the observation point. Therefore, for the purpose of determining the direction of vertical wave energy flux, observation of polarization appears to be more useful than observation of the apparent vertical phase propagation.

The behavior of wave polarization and the direction of phase propagation both appear to indicate that the vertical energy flux is directed downward, away from the sea surface. It is necessary, however, to discuss just what the partition of energy between clockwise and counterclockwise means for these waves. In particular, we have limited the above discussion to a single wave. It is more appropriate to relate the partition of clockwise and

counterclockwise energy to the energy carried by upward and downward propagating waves. This will be done in Chapter IV.

It is known from internal wave theory (see, for example, Garrett and Munk, 1972) that internal waves with frequencies near the inertial frequency are isotropic in time; that is, the magnitude of the frequency spectrum of a near-inertial wave horizontal velocity component will be independent of the direction of that velocity component. The same isotropy will be true for the vertical wave number spectra of near-inertial waves, provided only that east and north spectra for a sufficient number of profiles are averaged together.

To see why this is true, we consider a single internal wave propagating energy downward. The u' and v' velocity components are given by equations III-8:

$$\left. \begin{aligned} u'_d &= -\cos(k'x' + mz - \omega t) \\ v'_d &= -\frac{f}{\omega} \sin(k'x' + mz - \omega t) \end{aligned} \right\} \times A \frac{(N^2 - \omega^2)^{1/4}}{(\omega^2 - f^2)^{1/2}} \quad \text{III-12}$$

where A is the wave amplitude. ~~We point out that~~ the hodograph in z for this wave is given by:

$$\frac{u'^2}{1} + \frac{v'^2}{\left(\frac{f}{\omega}\right)^2} = A^2(m, \omega, \alpha) \frac{(N^2 - \omega^2)^{1/2}}{(\omega^2 - f^2)} \quad \text{III-13}$$

At any time, the ratio of semi-major to semi-minor axis is $\frac{\omega}{f}$, and as $\omega \rightarrow f$, the wave becomes circularly polarized. If we assume the presence of a second wave propagating upward with the same vertical

wave number magnitude, m , and the same frequency, ω , but with different amplitude, B , then the velocity components for this wave are given by:

$$\left. \begin{aligned} u'_u &= \cos(k'x' - mz - \omega t) \\ v'_u &= \frac{f}{\omega} \sin(k'x' - mz - \omega t) \end{aligned} \right\} \times B \frac{(N^2 - \omega^2)^{1/4}}{(\omega^2 - f^2)^{1/2}} \quad \text{III-14}$$

We assume A and B to be real now, although this is not necessary.

We also assume we are observing at the coordinate origin, so

$x' = 0$. The result of adding the two waves together gives:

$$u'_T = \frac{(N^2 - \omega^2)^{1/4}}{(\omega^2 - f^2)^{1/2}} [(B - A) \cos(mz) \cos(\omega t) - (A + B) \sin(mz) \sin(\omega t)],$$

$$v'_T = \frac{(N^2 - \omega^2)^{1/4}}{(\omega^2 - f^2)^{1/2}} [(A - B) \cos(mz) \sin(\omega t) - (A + B) \sin(mz) \cos(\omega t)].$$

III-15

We see that, for a fixed z , the magnitude of u'_T averaged over a cycle in time, becomes equal to the average of v'_T as $\omega \rightarrow f$ independently of the magnitudes of A and B . Thus, spectra of u'_T and v'_T in frequency may be expected to show the same energy when the frequency is close to f .

The same is not true, however, if vertical wave number spectra of u'_T and v'_T are considered, as can be seen by fixing t in the above expressions. If A or B is zero, the vertical wave number spectra for u'_T and v'_T will be approximately equal for ω close to f .

However, if $A = B$ (which would occur if standing waves existed in the vertical), energy in the vertical wave number spectra of u'_τ and v'_τ will depend on t , the time in the wave cycle at which the spectra were obtained. For example, in this case, at $t = 0$, the spectrum of v'_τ will contain all the energy at that particular vertical wave number, m , and the spectrum of u'_τ would, in theory, be zero.

However, if vertical wave number spectra of u'_τ and v'_τ are taken at enough different times, t , in the wave cycle, we again approach isotropy for $\omega \rightarrow f$. This is true because, at a given m , the energy in u'_τ and v'_τ will be the same if averaged over time. The average vertical wave number spectra of Figures 14 and 17 can be considered as the sum of individual wave number spectra taken at numerous different times, t , in a wave cycle. Then the fact that much of the energy in the profiles appears to be contributed by waves with frequencies close to f explains why there is an equipartition of energy between the east and north components.

c.) Polarization in the deep water

As mentioned previously, we can approximately calculate deep water spectra (below 2500 dbar) without stretching and normalizing the velocity profiles. This is possible because N does not change much in the deep water. Calculating the clockwise and counter-clockwise spectra over the depth range 2500-5500 dbar for several profiles indicates that dominance of clockwise energy over counter-clockwise energy exists in the bottom half of the water column, at least for vertical wave lengths greater than about 100 dbar. This

is important because it indicates that, even in deep water, the net flux of energy by these near-inertial waves is downward. Pollard (1970) indicated in a theoretical study that it would be difficult for near-inertial waves to propagate down into the deep water with the observed intensity. The result of the above calculations indicates that these waves are, nevertheless, coming down from regions farther up in the water column. The Pollard model assumes that inertial waves are generated at the surface by an impulsive force that acts over some time and space interval. In Chapter V we will examine the behavior of the vertical energy flux of near-inertial waves for an assumed form of the internal wave energy spectrum in frequency and vertical wave number space.

d.) Comparison with meteorological observations

As was pointed out in the introduction, meteorologists have been conducting experiments to obtain vertical profiles of atmospheric winds for many years. Their results may be compared with results obtained by the EMVP in the ocean.

Various authors have pointed out that the existence of internal waves in the atmosphere has not been proved. For example, Justus and Woodrum (1973) felt it necessary to state that: "There has been no unambiguous resolution of gravity waves in the upper atmosphere (i.e. simultaneous observations of amplitudes, phases, and frequency sufficient to verify propagation according to the theoretical dispersion equation)." They go on to state that there

is, however, strong circumstantial evidence for the occurrence of internal waves. Some of that evidence will now be presented.

In 1966 radar tracking of radar-reflective balloons was used at Cape Canaveral to obtain profiles of atmospheric winds from 0 kilometers to about 16 kilometers (Endlich, et. al., 1969). Two series of profiles were made, each series lasting between one and two days. The method allows one to sample rather rapidly in the vertical (one point each 25 meters) but, unfortunately, it can only determine the wind speed at each point, not its direction. The authors point out that there are strong velocity features in the July 4-5, 1966, experiment which progressively move downward with time. The profiles are complicated, however, and no definite time or space scales stand out (although it is known that internal waves can exist in the atmosphere at these altitudes).

Although apparent high-frequency features in the atmosphere have been observed to change altitude, there appear to have been few reports of any polarization or directional structure associated with these features. Endlich could only measure speed as a function of altitude and therefore could not observe polarization. Hines (1966) has reported polarization of atmospheric winds that is apparently related to the diurnal atmospheric tide. His data, obtained by tracking sodium vapor trails at heights of 90-130 kilometers, indicates that winds with periods appropriate to the diurnal tide rotate with altitude in a given rocket profile. If an observer is imagined to be standing above the atmosphere and looking down,

then the waves seen by Hines have horizontal velocity vectors that rotate counterclockwise with increasing "depth," or atmospheric pressure. This is the opposite of the case observed in the ocean by the EMVP over the smooth topography, in which the horizontal current vector rotates clockwise with increasing depth. As Hines points out, the atmospheric observations indicate that the wave energy of these oscillations is propagating from lower altitudes up to the 90-130 kilometers range. This appears to be one of the few cases where wave polarization has been observed in the atmosphere (C. O. Hines, 1975, personal communication).

One good reason for a lack of elliptical or circular polarization in the motions interpreted as being internal waves in the atmosphere is the fact that these motions quite often have periods much shorter than the local inertial period. Hines (1960) points out that atmospheric internal waves might be expected to be most energetic at periods of several hours. For waves of this period, the earth's rotation is not a major influence, and a single atmospheric internal wave with a three hour period would be almost linearly polarized in the vertical.

Hines also notes that some observations in the atmosphere show structures which progressively move downward in time. Using the same arguments as those put forth in describing Figure 21, he points out that because the directions of vertical phase propagation and energy flux are opposite for internal waves, these downward moving structures in the upper atmosphere could be interpreted

as internal waves carrying energy upward, away from the lower atmosphere and the surface of the earth. (The sources for atmospheric internal waves are thought by many meteorologists to be located in the lower atmosphere or at the earth's surface.)

Finally, there is some evidence from fresh water lakes that appears to indicate upward phase propagation of internal waves. Lazier (1973) obtained a series of temperature profiles in Lake Bala, Wales, over a time interval of about 12 hours. Profiles were repeated at approximately 11 minute intervals. In many cases, features in the temperature profile were observed to move progressively upward in time. Lazier attributes this upward motion of temperature features to the presence of propagating internal waves. If the energy source for these waves was located at the lake surface, they would have to propagate their energy downward. Then, as in Figure 21, the wave number vectors of the waves would be directed toward the lake surface, and the wave phase would move upward in time. Since Lazier only measured temperature profiles, however, no data on wave velocity polarization were obtained.

Chapter IV The Use of the Ratio of Clockwise to Counterclockwise
Energy as a Reflection Coefficient. Reflection of Internal Waves
From a Smooth Bottom

a.) Calculation of a reflection coefficient for the observed waves

We pointed out in Chapter III that the dominance of clockwise over counterclockwise vertical wave number spectra for horizontal kinetic energy appears to indicate that the net vertical energy flux for these waves is downward. However, a further step must be taken if we are to relate the partition between clockwise and counterclockwise energy to the energy in upward and downward propagating waves. This step is to assume that the observed waves have frequencies close enough to f so that any single wave should be almost circularly polarized in the vertical (see equation III-13). The sense of polarization is determined by whether the wave energy flux is downward (clockwise polarization) or upward (counterclockwise polarization). With this assumption, the horizontal kinetic energy of the downward propagating waves is approximately equal to $C(m')$, the clockwise energy in the vertical wave number spectrum, while the horizontal kinetic energy of the upward propagating waves is approximately equal to $A(m')$, the counterclockwise energy in the same spectrum. (Strictly speaking, $A(m')$ and $C(m')$ should be multiplied by the Brunt-Väisälä frequency to get the true energy level (see Chapter V). However, since we are finally interested only in

the ratio of clockwise to counterclockwise energy, this step has been ignored.)

We have assumed in the previous paragraph that inertial waves are the primary cause of high-frequency energy in the profiles. However, frequency spectra of horizontal velocity obtained at the central mooring (M. Briscoe, 1975, personal communication) indicate that the diurnal and semidiurnal tides also contribute to the internal wave frequency range (see Figure 29). Because of the relatively short length of the time series, it is difficult to resolve semidiurnal tidal and inertial oscillations in frequency, and it is impossible to resolve diurnal tidal and inertial oscillations. On the other hand, we can make inferences concerning the probable influence of the tides on the vertical wave number spectra computed in Chapter II. First, that part of the tidal energy which is caused by the surface or barotropic tide, since it is depth-independent, is not sensed by the EMVP. Second, work of other investigators (Hendry, 1974) appears to show that most of the tidal energy, at least for the semidiurnal tide, is concentrated in the first two or three baroclinic modes (along with the surface tide). In terms of the vertical wave number spectra of Chapter II, this means that any tidal contributions to the spectra are located in the lowest and, possibly, the second-lowest wave number estimates. We may then infer that above the first one or two vertical wave number estimates, the primary contributions to the spectra come from inertial-internal waves. There is also direct evidence from

the profiles to indicate that most of the semidiurnal tidal energy is contributed by waves with small vertical wave numbers. This evidence will be presented in Chapter V.

We now assume that the observed waves are generated at or near the surface and propagate their energy downward. Upon reaching the bottom, some fraction of their energy is reflected upward toward the surface, while the remainder of the energy is lost in a frictional boundary layer at the bottom. There may also be some energy loss as the waves propagate through the interior. We also assume that the smooth bottom does not act as an energy source for these waves (that is, a boundary layer at the bottom will remove energy from the incoming waves, but other processes do not act to put energy into waves that are reflected from the bottom). The theoretical model presented later in this chapter will hopefully indicate how reasonable the above assumptions are.

If we accept these assumptions, then the ratio $A(m')/C(m')$ can be thought of as a reflection coefficient for these waves. This ratio is shown in Figure 22, using the spectra of Figures 13 and 16. Since the bottom, by assumption, cannot act to put energy into the waves, a good test of the above model is that $A(m')/C(m')$ should always be less than one. An examination of Figure 22 shows that this is substantially true, although at high wave numbers (or low energy), the ratio $A(m')/C(m')$ behaves erratically. This erratic behavior at low energy levels may be an indication that the signal-to-noise ratio of the EMVP is becoming small. A low

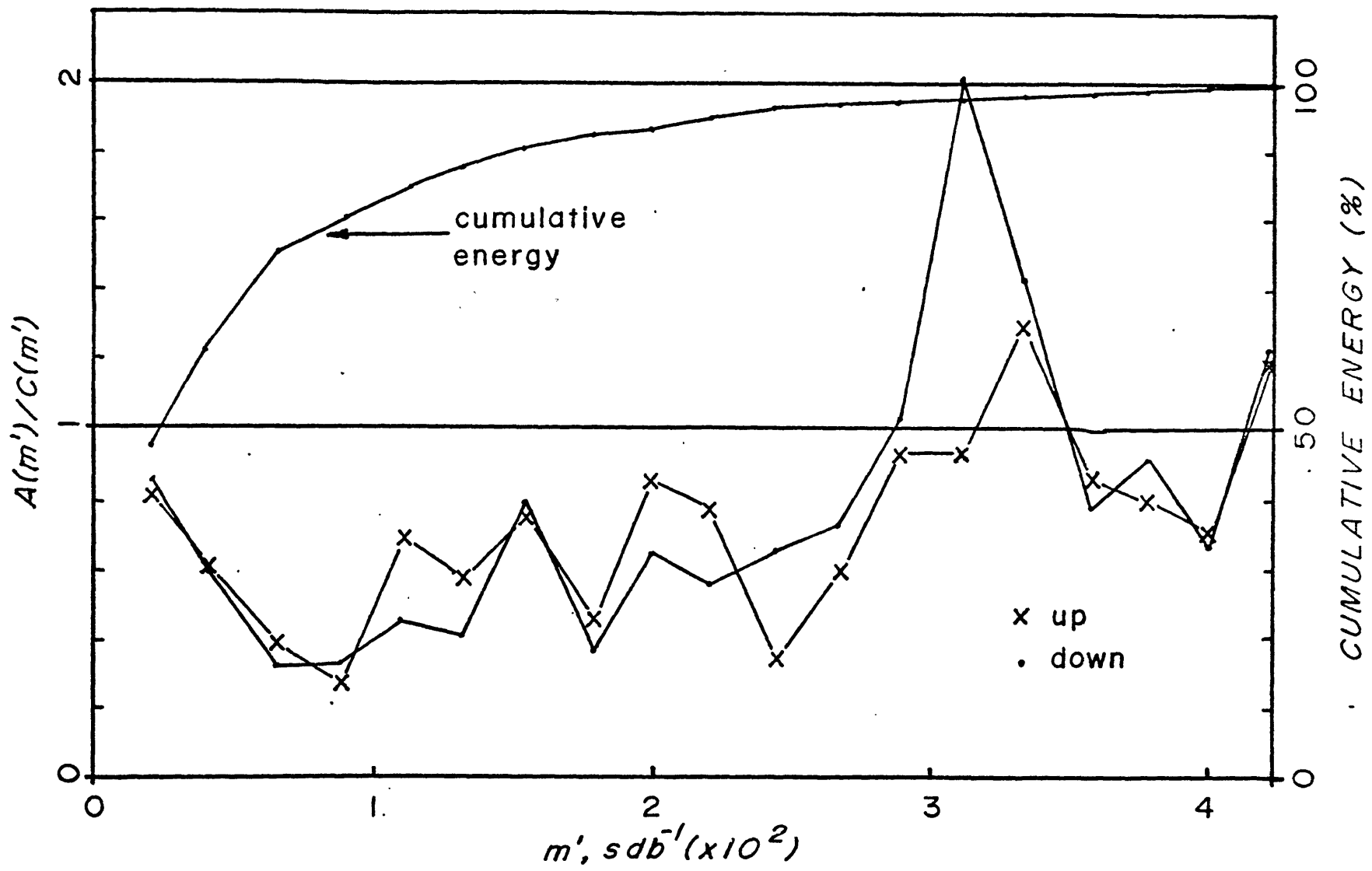


Figure 22. Reflection coefficient $A(m')/C(m')$.

signal-to-noise ratio will cause the east and north velocity components to lose correlation (or coherence). Therefore, the quadrature spectrum of the east and north components will decrease. Since this quadrature spectrum (in stretched vertical wave number) is proportional to the difference between $A(m')$ and $C(m')$ (see Appendix D), the clockwise and counterclockwise spectra will tend to become equal as the signal-to-noise ratio falls. Also shown in Figure 22 is the cumulative energy of the stretched vertical wave number spectrum, expressed as percent of total energy. It can be seen that about 97% of the total energy is contained in waves whose ratios of $A(m')/C(m')$ are less than one.

It is important to emphasize that the above interpretation of the reflection coefficient depends strongly on the assumption that most of the waves observed in the profiles have frequencies close to the inertial frequency. The short length of the time series does not permit good frequency resolution. We have already pointed out that the lowest wave number estimates appear to be heavily influenced by the semidiurnal tides (see Chapter V). At larger vertical wave numbers it is also likely that waves with frequencies appreciably greater than f are contributing to the profiles. We know that a wave with ω greater than f is not circularly, but elliptically, polarized, with a ratio of semi-major to semi-minor axes of ω/f . The presence of such waves in the profiles would presumably cause the ratio $A(m')/C(m')$ to increase (the addition of a circularly polarized wave to one which is strongly elliptically

polarized results in an elliptically polarized wave). This argument indicates that $A(m')/C(m')$ is probably an over-estimate of the reflection coefficient for the near-inertial waves. The reader may refer to Appendix D for a more complete discussion of the influence of higher frequency waves on the clockwise and counterclockwise spectra.

b.) A model for the reflection of internal waves from a smooth bottom

A theoretical model for internal wave reflection can be developed that supports some of the assumptions made in the previous section. This model is a variation of one studied by Phillips (1963) that analyzes the reflection of purely inertial waves from a flat boundary. The present model includes buoyancy effects but otherwise gives much the same results as Phillips' model.

We start with the usual equations for internal waves, with buoyancy and rotation:

$$\frac{\partial u}{\partial t} - fv = -\frac{\partial p}{\partial x} + \nu \nabla^2 u$$

$$\frac{\partial v}{\partial t} + fu = -\frac{\partial p}{\partial y} + \nu \nabla^2 v$$

$$\frac{\partial w}{\partial t} = -\frac{\partial p}{\partial z} + b + \nu \nabla^2 w$$

$$\frac{\partial b}{\partial t} + N^2 w = 0$$

$$\frac{\partial u}{\partial x} + \frac{\partial v}{\partial y} + \frac{\partial w}{\partial z} = 0$$

The reader can refer to Appendix B for definitions of the quantities in the above equations. The only additional terms in the above equations are the frictional terms $\nu \nabla^2 u$, $\nu \nabla^2 v$ and $\nu \nabla^2 w$, where ν is the kinematic viscosity coefficient. The Brunt-Väisälä frequency, N , is assumed to be constant. This is not a serious assumption, since near the bottom where we expect the model to apply, N is fairly constant with depth.

If all variables are independent of the y coordinate, a stream function, ψ , can be introduced that satisfies continuity:

$$u = \frac{\partial \psi}{\partial z} \quad \text{and} \quad w = - \frac{\partial \psi}{\partial x} . \quad \text{IV-2}$$

If ψ is substituted into equations IV-1, these equations can be reduced to two equations in ψ and v :

$$\left[\frac{\partial}{\partial t} \nabla^2 \left(\frac{\partial}{\partial t} - \nu \nabla^2 \right) + N^2 \frac{\partial^2}{\partial x^2} \right] \psi - f \frac{\partial^2 v}{\partial t \partial z} = 0 ;$$

$$f \frac{\partial \psi}{\partial z} + \left[\frac{\partial}{\partial t} - \nu \nabla^2 \right] v = 0 . \quad \text{IV-3}$$

The coordinate origin is assumed to be located at the bottom, so that $z = 0$ there, and the coordinates form a right hand system. Then equations IV-3 must satisfy the boundary conditions $u(z = 0) = v(z = 0) = w(z = 0) = 0$ or:

$$\psi = \frac{\partial \psi}{\partial z} = v = 0 \quad \text{at} \quad z = 0 . \quad \text{IV-4}$$

We look for solutions of the form:

$$\begin{aligned}\psi &= A e^{k\mu z} e^{i(kx-\omega t)} \\ v &= V e^{k\mu z} e^{i(kx-\omega t)}\end{aligned}\quad \text{IV-5}$$

If these expressions for ψ and v are substituted in equations IV-3, there results a sixth order equation in μ :

$$\begin{aligned}[R^2] \mu^6 + [2i\omega'R - 3R^2] \mu^4 \\ + [1 - \omega'^2 - 4i\omega'R + 3R^2 + i\frac{N^2}{f\omega} R] \mu^2 \\ + [\frac{\omega^2 - N^2}{f^2} + 2i\omega'R - R^2 - i\frac{N^2}{f\omega} R] = 0,\end{aligned}\quad \text{IV-6}$$

where $\omega' = \frac{\omega}{f}$ and $R = \frac{vk^2}{f}$. If we assume that $R = 0$, the characteristic equation for μ becomes:

$$\begin{aligned}\mu^2 &= -\frac{N^2 - \omega^2}{\omega^2 - f^2} \\ \text{or } \mu_{1,2} &= \pm i\left(\frac{N^2 - \omega^2}{\omega^2 - f^2}\right)^{1/2}.\end{aligned}\quad \text{IV-7}$$

These two roots give the z -dependence that would be expected from two internal waves propagating without friction.

If we now assume $R \ll 1$, we can factor out the above two roots to get approximate expressions for the remaining four:

$$\mu^2 = -\frac{i\omega'}{R} \pm$$

$$(1/2)\left[-\frac{4}{R^2} - \frac{4i}{R} \left(\frac{N^2}{\omega f} - 4\omega' - 2\omega' \frac{N^2 - \omega^2}{\omega^2 - f^2}\right)\right]^{1/2} \quad \text{IV-8}$$

If we assume that the $-\frac{4}{R^2}$ term dominates under the radical, then the expression for the four remaining roots becomes;

$$\mu^2 = \frac{i}{R} (-\omega' \pm 1) \quad \text{IV-9}$$

Noting that ω is assumed positive, we find that the two boundary layer roots which give solutions that decay into the interior are

$$\mu_{3,4} = \frac{i-1}{\sqrt{2R}} (\omega' \mp 1)^{1/2} \quad \text{IV-10}$$

The four roots of μ that have been obtained for the two propagating internal waves and the two boundary layer solutions are then:

$$\begin{aligned} \mu_1 &= i \left(\frac{N^2 - \omega^2}{\omega^2 - f^2}\right)^{1/2}; \\ \mu_2 &= -i \left(\frac{N^2 - \omega^2}{\omega^2 - f^2}\right)^{1/2}; \\ \mu_3 &= \frac{i-1}{\sqrt{2R}} (\omega'-1)^{1/2}; \\ \text{and } \mu_4 &= \frac{i-1}{\sqrt{2R}} (\omega'+1)^{1/2}. \end{aligned} \quad \text{IV-11}$$

We note that the thickness of the boundary layer is determined by the quantity $(\omega' - 1)^{1/2}/\sqrt{2R}$, for ω' positive and close to one. As $\omega' \rightarrow 1$, or as $\omega \rightarrow f$, the boundary layer penetrates more and more deeply into the interior.

The expressions for v and ψ are now:

$$\psi = [A_1 e^{k\mu_1 z} + A_2 e^{k\mu_2 z} + A_3 e^{k\mu_3 z} + A_4 e^{k\mu_4 z}] e^{i(kx - \omega t)}$$

$$v = [V_1 e^{k\mu_1 z} + V_2 e^{k\mu_2 z} + V_3 e^{k\mu_3 z} + V_4 e^{k\mu_4 z}] e^{i(kx - \omega t)} \quad \text{IV-12}$$

where μ_1 through μ_4 are given above. The A's and V's must be determined from the boundary conditions at the bottom (equations IV-4).

The terms with V_1 and A_1 in the expressions for ψ and v give the amplitude of the incoming wave, while the terms involving V_2 and A_2 give the amplitude of the reflected wave. The average horizontal kinetic energy for the incoming wave is given by:

$$E_i = |V_1|^2 \left(1 + \frac{\omega^2}{f^2}\right) \quad \text{IV-13}$$

The average horizontal kinetic energy for the reflected wave is:

$$E_o = |V_1|^2 \left(1 + \frac{\omega^2}{f^2}\right) \left|\frac{A}{B}\right|^2 \quad \text{IV-14}$$

where

$$A = \omega' \alpha - \frac{i\sqrt{2R}}{(i-1)(\omega'-1)^{1/2}} - \frac{i\sqrt{2R}(\omega'-1)}{2(i-1)} \left\{ \frac{1}{(\omega'-1)^{1/2}} + \frac{1}{(\omega'+1)^{1/2}} \right\} \quad \text{IV-15}$$

and

$$B = \omega' \alpha + \frac{i \sqrt{2R}}{(i-1)(\omega'-1)^{1/2}} + \frac{i \sqrt{2R}(\omega'-1)}{2(i-1)} \frac{1}{(\omega'-1)^{1/2}} + \frac{1}{(\omega'+1)^{1/2}}$$

IV-16

and

$$\alpha = \frac{(\omega^2 - f^2)^{1/2}}{N^2 - \omega^2}$$

IV-17

Using E_i and E_o , we can form a reflection coefficient for the horizontal kinetic energy:

$$\frac{E_o}{E_i} = 1 - \frac{\sqrt{2R} (N^2 - \omega^2)^{1/2}}{\omega(\omega'^2 - 1)^{1/2}} \left\{ \frac{\omega' + 1}{(\omega' - 1)^{1/2}} + \frac{\omega' - 1}{(\omega' + 1)^{1/2}} \right\} + O(R).$$

IV-18

This reflection coefficient has several characteristics that are relevant to the present data. First, although for dimensionless frequencies ω' much greater than one, $E_o/E_i \sim 1$, as $\omega' \rightarrow 1$ this reflection coefficient decreases rapidly (E_o/E_i does not limit to zero as $\omega \rightarrow f$ due to the approximations made in the above derivation). This shows that energy in waves near the inertial frequency may be greatly reduced as these waves reflect off the bottom. Most of the energy loss suffered by these waves takes place in the bottom frictional boundary layer (a boundary layer, we recall, that grows in thickness as $\omega \rightarrow f$). For frequencies close to f , E_o/E_i is very

sensitive to ω . Since we cannot resolve ω as closely as would be required to test the above theory, we can only say that the observed "reflection coefficients" (Figure 22) and the possible boundary layer thickness (described below) can be accounted for if the frequencies of the observed waves are close enough to f .

Figure 8 appears to indicate that, from 2000 dbar to about 5300 dbar, at least, the average perturbation horizontal kinetic energy follows closely the average profile of N . This would seem to imply that the waves are not undergoing strong frictional losses as they propagate through the water column, and therefore that most of the energy loss from these waves takes place as they reflect off the bottom.

There is also a suggestion in Figure 8 that the mean perturbation kinetic energy decreases within about 100-150 dbar above the bottom. This may indicate the presence of a frictional boundary layer at the bottom. In theory, the horizontal kinetic energy must go to zero at the bottom. However, the EMVP only measures horizontal velocity to about 10 dbar above the bottom. Thus, it probably would not see that part of the frictional boundary layer nearest the bottom, where the greatest energy loss takes place. The error estimate (Chapter II) calculated for the mean perturbation kinetic energy profile of Figure 8 indicates that the decrease in energy near the bottom is significant. We again must emphasize, however, that this error estimate only takes into account the influence of instrumental noise.

Figure 8 also shows an apparent bulge in the mean perturbation horizontal kinetic energy at about 200 dbar above the bottom. This bulge remains even if the kinetic energy profile is normalized by the mean Brunt-Väisälä profile (N also increases as the bottom is approached). The theory presented above predicts only that the mean perturbation horizontal kinetic energy should increase smoothly from zero at the bottom to values appropriate to the incoming and outgoing waves beyond the frictional boundary layer. Therefore, this apparent bulge in the kinetic energy near the bottom is not explained by the above theory. The possible existence of small bottom slopes may be crucial here. The above theory assumes a flat, horizontal bottom. Wunsch (1969) has shown that if the group velocity vector for the reflected wave has an inclination angle to the horizontal which is close to the bottom slope, an intensification of the internal wave energy near the bottom can take place. Since the group velocity vectors for waves near the inertial frequency are only slightly inclined to the horizontal, the near-bottom behavior of these waves may depend strongly on small bottom slopes.

Chapter V Comparison of Vertical Wave Number Spectra with Theoretical Models. Computation of Dropped, Time-lagged, Rotary Coherence (DLRC). The Vertical Energy Flux of Internal-inertial Waves.

a.) Vertical wave number spectra

Recently, several models have been derived which describe the amount of energy contributed to a region of the ocean by internal waves of various length and time scales. Perhaps the primary model of this type is that of Garrett and Munk (1972, 1975). These authors have constructed an internal wave energy density spectrum, $E(\alpha, \omega)$, as a function of horizontal wave number, α , and frequency, ω . The energy spectrum is assumed to be isotropic; that is, the magnitude of E is independent of the direction of α . The general form of $E(\alpha, \omega)$ is (Garrett and Munk, 1972, eq. 6.3):

$$E(\alpha, \omega) = C\mu^{-1}A(\lambda)\Omega(\omega). \quad \text{V-1}$$

This is a dimensionless equation. Time has been made dimensionless by a reference Brunt-Väisälä frequency,

$$N_0 = 3 \text{ cph}, \quad \text{V-2}$$

and distance by a reference cyclical wave number,

$$M_0 = 0.122 \text{ cpm}. \quad \text{V-3}$$

C is a constant. μ is called the " α -bandwidth of the spectrum" as

a function of frequency. The parameter λ is given by:

$$\lambda = \alpha/\mu . \quad \text{V-4}$$

The form chosen for $\Omega(\omega)$ was:

$$\Omega(\omega) = \omega^{-p+2s} (\omega^2 - \omega_i^2)^{-s}, \quad \text{V-5}$$

where ω_i is the (non-dimensional) local inertial frequency. The constants p and s were chosen to be 2 and 1/2, respectively. Then

$$\Omega(\omega) = \frac{1}{\omega(\omega^2 - \omega_i^2)^{1/2}} . \quad \text{V-6}$$

In the 1972 version of the model, $A(\lambda)$ was chosen to have the form of a "top hat":

$$\begin{aligned} A(\lambda) &= 1, \text{ for } 0 \leq \lambda \leq 1 \\ \text{and } A(\lambda) &= 0, \text{ for } \lambda > 1. \end{aligned} \quad \text{V-7}$$

Finally, $\mu(\omega)$ was chosen to be:

$$\mu(\omega) = j_* \pi (\omega^2 - \omega_i^2)^{1/2}, \quad \text{V-8}$$

where j_* is an integer. In the 1972 model, j_* was called the "equivalent number of modes at the inertial frequency" by the authors. (It should be emphasized that their model does not really depend on the existence of modes in the vertical. The parameter j_* can be thought of as characterizing the maximum vertical wave number found to contain significant energy in the internal wave energy

density spectrum). We would now like to see how this theoretical model compares to vertical wave number spectra observed by the EMVP.

In order to proceed further we must introduce the dimensional forms of the above equations. In what follows, a hat (^) above a quantity will indicate that it is dimensional. A prime (') will indicate that vertical wave numbers in the stretched coordinate are being used.

The dispersion relation for internal waves (under a WKB approximation) gives:

$$\hat{\alpha} = \hat{m}(z) \frac{(\hat{\omega}^2 - \hat{f}^2)^{1/2}}{\hat{N}(z)} \quad \text{for } \hat{\omega} \ll \hat{N}(z) \quad \text{V-9}$$

where \hat{m} is the local vertical wave number. Also,

$$\mu = j_* \pi (\omega^2 - \omega_i^2)^{1/2} = j_* \pi \frac{(\hat{\omega}^2 - \hat{f}^2)^{1/2}}{N_0} \quad \text{V-10}$$

Then

$$\lambda = \alpha/\mu = \frac{\hat{\alpha}}{\mu M_0} = \frac{\hat{m}(z) N_0}{(j_* \pi) M_0 \hat{N}(z)} \quad \text{V-11}$$

However, since in the stretched vertical coordinate

$$\hat{m}' = \hat{m}(z) (N_0/\hat{N}(z)), \quad \text{V-12}$$

we have

$$\lambda = \frac{\hat{m}'}{(j_* \pi) M_0} \quad \text{V-13}$$

Then the dimensional form of $\Omega(\omega)$ becomes

$$\Omega(\hat{\omega}) = \frac{N_0}{\hat{\omega}(\hat{\omega}^2 - f^2)^{1/2}}, \quad \text{V-14}$$

and

$$E(\hat{\omega}, \hat{m}') = C A(\lambda) \frac{N_0^3}{(j_* \pi) \hat{\omega}(\hat{\omega}^2 - \hat{f}^2)}. \quad \text{V-15}$$

The total energy in horizontal velocity is given by

$$E_{\text{total}} = \int_{\alpha} \int_{\omega} E(\alpha, \omega) \overline{U^2} d\alpha d\omega \quad \text{V-16}$$

where

$$\overline{U^2} = \frac{\hat{N}(z)}{N_0} \left(\frac{\omega^2 + \omega_i^2}{\omega^2} \right) \quad (\text{Garrett and Munk, 1972}). \quad \text{V-17}$$

However, since velocity in the profiles has been normalized by $N(z)/N_0$, we must use

$$\overline{U^2}' = \frac{\overline{U^2}}{(\hat{N}(z)/N_0)} \quad \text{V-18}$$

instead of $\overline{U^2}$ in equation V-16. Converting α and ω to their dimensional counterparts, where

$$\alpha = \hat{\alpha}/M_0 \quad \text{and} \quad \omega = \hat{\omega}/N_0, \quad \text{V-19}$$

we have

$$E_{\text{total}} = \frac{1}{M_0 N_0} \int_{\hat{\alpha}} \int_{\hat{\omega}} \overline{U^2}' E(\hat{\alpha}, \hat{\omega}) d\hat{\alpha} d\hat{\omega} \quad \text{V-20}$$

Instead of integrating over $\hat{\alpha}$, we wish to carry out the integration over \hat{m}' . Since

$$d\hat{\alpha} = \frac{(\hat{\omega}^2 - \hat{f}^2)^{1/2}}{\hat{N}(z)} d\hat{m} \quad \text{V-21}$$

and

$$d\hat{m}' = (N_0/\hat{N}(z)) d\hat{m}, \quad \text{V-22}$$

the integral becomes

$$\begin{aligned} E_{\text{total}} &= \frac{1}{M_0 N_0} \int_{\hat{m}'} \int_{\hat{\omega}} U^2 E(\hat{m}', \hat{\omega}) \frac{(\hat{\omega}^2 - \hat{f}^2)^{1/2}}{N_0} d\hat{m}' d\hat{\omega} \\ &= \frac{1}{N_0 M_0} \int_{\hat{m}'} \int_{\hat{\omega}} E(\hat{m}', \hat{\omega}) \frac{(\hat{\omega}^2 + \hat{f}^2)}{\hat{\omega}^2} \frac{(\hat{\omega}^2 - \hat{f}^2)^{1/2}}{N_0} d\hat{m}' d\hat{\omega} \\ &= \frac{CN_0}{(j\star\pi)M_0} \int_{\hat{m}'} \int_{\hat{\omega}} \frac{(\hat{\omega}^2 + \hat{f}^2)}{\hat{\omega}^3(\hat{\omega}^2 - \hat{f}^2)^{1/2}} A\left(\frac{\hat{m}'}{j\star\pi M_0}\right) d\hat{\omega} d\hat{m}'. \quad \text{V-23} \end{aligned}$$

E_{total} must be multiplied by $\hat{\rho}N_0^2M_0^{-3}$ to obtain the dimensional energy spectrum, where $\hat{\rho}$ is sea water density (assumed equal to 1 gm/cm³). Removing the integral over \hat{m}' leads to the following dimensional form of the energy density spectrum in stretched vertical wave number, \hat{m}' :

$$\begin{aligned} \hat{E}_{\hat{m}'}(\hat{m}') &= \frac{\hat{\rho}CN_0}{j\star\pi M_0} A\left(\frac{\hat{m}'}{j\star\pi M_0}\right) \int_{\hat{\omega}} \frac{\hat{\omega}^2 + \hat{f}^2}{\hat{\omega}^3(\hat{\omega}^2 - \hat{f}^2)^{1/2}} d\hat{\omega} \\ &= \frac{N_0^2}{M_0^3} \frac{3E_0}{2j\star\pi} A\left(\frac{\hat{m}'}{j\star\pi M_0}\right) \quad \text{V-24} \end{aligned}$$

(C. Garrett, 1974, personal communication).

E_0 is a dimensionless constant which is related to C by

$$E_0 = C \int_{\omega_f}^{\lambda} \Omega(\omega) d\omega \quad \text{V-25}$$

To obtain the actual energy levels at a given depth, z_0 , $\hat{E}_{\hat{m}'}(\hat{m}')$ is multiplied by $(\hat{N}(z)/N_0)$. At that level

$$\hat{m}' = \hat{m}(z_0) (N_0/\hat{N}(z_0)). \quad \text{V-26}$$

The quantity $\hat{E}_{\hat{m}'}(\hat{m}')$, as obtained by observations, has been given already in Figures 12 and 15. Clearly, the form of the stretched vertical wave number spectrum depends on $A(\lambda)$. In the 1972 model, $A(\lambda)$ was chosen to be a top hat. Comparing equations V-7 and V-13, we see that $A(\lambda) = 1$ for $\hat{m}' \leq j_* \pi M_0$ and $A(\lambda) = 0$ for $\hat{m}' > j_* \pi M_0$. (Again we see that in the top hat model j_* controls the maximum vertical wave number that contributes energy to the spectrum). This means that the theoretical $\hat{E}_{\hat{m}'}$ is independent of \hat{m}' for $\lambda \leq 1$, and is zero for $\lambda > 1$. It is clear from Figures 12 or 15 that $\hat{E}_{\hat{m}'}$ is not independent of \hat{m}' , but in fact decreases with increasing \hat{m}' .

In a revised form of their model (Garrett and Munk, 1975), these investigators chose a new form for the function $A(\lambda)$:

$$A(\lambda) = (t - 1) (1 + \lambda)^{-t} \quad \text{V-27}$$

where t is chosen to fit observation. Garrett and Munk picked

$$t = 2.5. \quad \text{V-28}$$

(The choice of $t = 2.5$ appears to agree reasonably well with vertical displacement spectra obtained by Hayes, et. al. (1975)). For $N_0 = 3$ cph, $M_0 = 0.122$ cphkm, $E_0 = 2\pi \times 10^{-5}$ and $j_* = 6$ (in the 1972 model, j_* was 20), the vertical stretched wave number spectrum becomes

$$\hat{E}_{\hat{m}'}(\hat{m}') = 19.1 A(\lambda) \frac{(\text{cm/sec})^2}{\text{cphkm}} \quad \text{V-29}$$

and

$$\lambda = 0.435 \hat{m}' \quad \text{V-30}$$

We have repeated the stretched vertical wave number spectrum of Figure 12 in Figure 23. Figure 23 also shows the theoretical stretched vertical wave number spectrum, $\hat{E}_{\hat{m}'}(\hat{m}')$, using the form of $A(\lambda)$ given by equation V-27, for three choices of j_* : $j_* = 6$, $j_* = 15$ and $j_* = 20$. (The cyclical frequency has been converted from cycles per kilometer to cycles per sdb). The value of the constant for the spectral energy level, $E(j_*)$, (corresponding to E_0 in the above derivation) has been adjusted to make the three theoretical curves have the same energy levels at large stretched vertical wave numbers. If $E(j_*)$ is the actual value of the constant used for a given j_* , and $E_0 = 2\pi \times 10^{-5}$, we have the following values for $E(j_*)$: $E(j_* = 6) = 2 \times E_0$; $E(j_* = 15) = 0.6 \times E_0$; $E(j_* = 20) = 0.4 \times E_0$. The theoretical curve for a j_* of 15 appears to best represent the observed stretched vertical wave number spectrum, both in the general shape of the spectrum and in the total energy level.

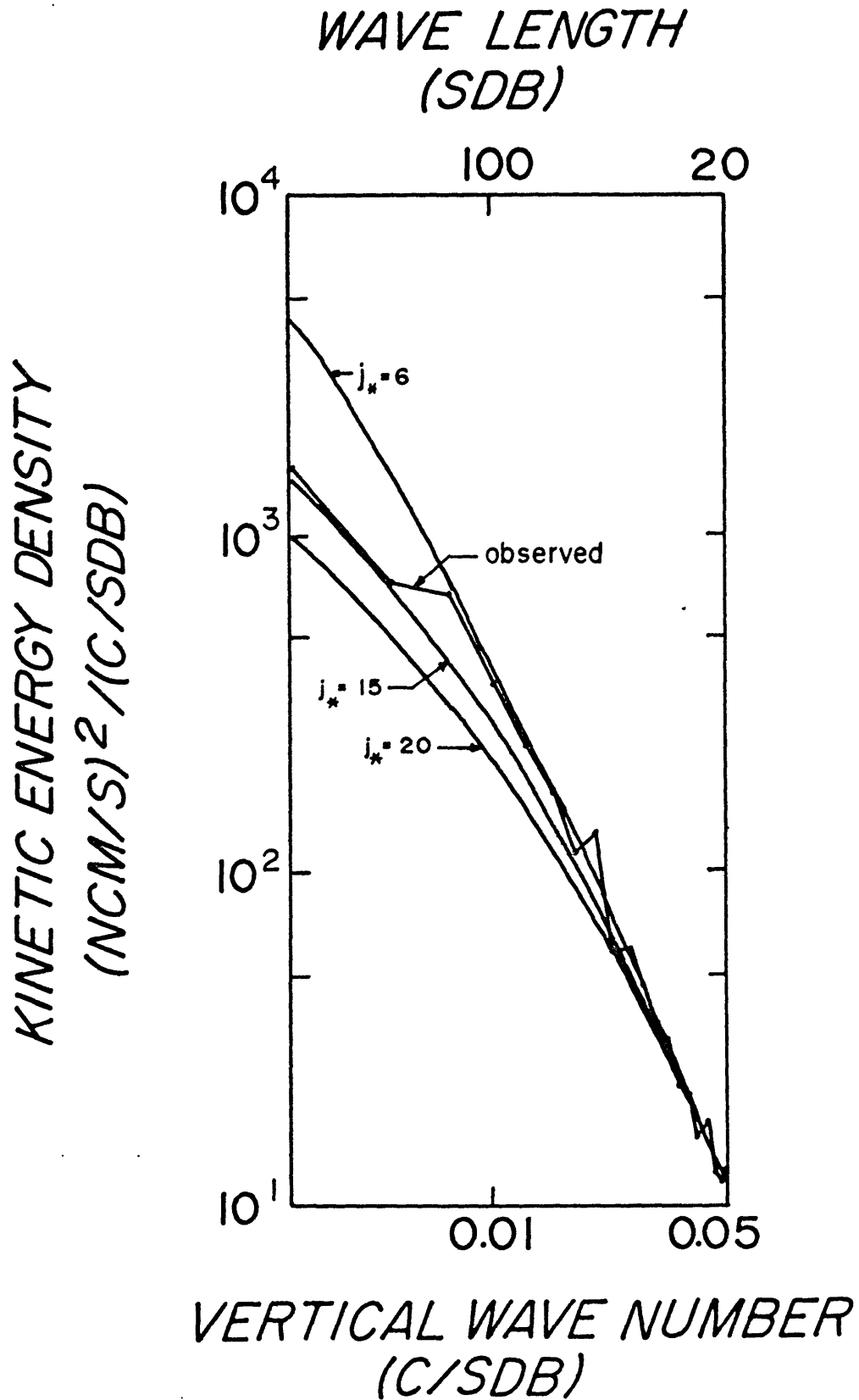


Figure 23. Comparison of theoretical and observed total energy spectra in stretched vertical wave number (see text).

A value of 15 for j_* is larger than the value of 6 assumed in the 1975 model. If we return for the moment to a consideration of Figures 10 and 11, the reason why $j_* = 6$ is apparently too small becomes clearer. Visually, Figures 10 and 11 show that waves containing relatively high energy have wave lengths as short as 100 sdb. The total depth in the stretched vertical coordinate is 1860 sdb. If we now assume that j_* is in some sense representative of the greatest number of stretched vertical wave lengths that "fit" into 1860 sdb (and contain significant energy), we find that, for 100-130 sdb vertical wave lengths, j_* should be at least 15.

It is also interesting to note that the value of E required to make the theoretical ($j_* = 15$) and observed stretched vertical wave number spectra contain (roughly) the same total energy is about 60% of the constant, E_0 , chosen by Garrett and Munk. The fact that high-frequency internal waves (those with frequencies near N) are probably not energetic enough to be sensed by the EMVP may partially explain this. However, it is also likely that the total energy of the internal wave field at the MODE central mooring is less than the total energy at other locations (at Site D ($39^\circ 20' N, 70^\circ 00' W$), for example). Since observations at Site D were used (at least in part) to determine E_0 , the fact that $E(j_* = 15)$ is less than E_0 may also reflect an actual decrease in internal wave energy at the central mooring, relative to other locations in the ocean where measurements have been made.

b.) Dropped, time-lagged, rotary coherence of profiles

The following calculations were carried out in order to compare profiler horizontal velocity data with some theoretical results based on the Garrett and Munk model presented in section a. (C. Garrett, 1974, personal communication). Since we have a time series of profiles, it is possible to calculate the velocity coherence between two profiles separated by a time interval, T , for any stretched vertical wave number. This is called the dropped, lagged, coherence (or DLC) by Garrett and Munk. However, we know that much of the variability in the profiles is associated with waves having periods near the local inertial period. For this reason, instead of the DLC we have calculated the coherence between two profiles when the horizontal velocities of the second profile have been rotated through an angle γ :

$$\begin{aligned}\gamma &= \omega T, \\ \omega &= 2\pi f,\end{aligned}\tag{V-31}$$

where f is the inertial frequency and T is the time interval between the two profiles. This is called the dropped, lagged, rotary coherence (or DLRC). If the first velocity profile is

$$W_1(\tilde{z}^*) = U_1(\tilde{z}^*) + iV_1(\tilde{z}^*),\tag{V-32}$$

and the second profile is given by

$$W_2(\tilde{z}^*) = U_2(\tilde{z}^*) + iV_2(\tilde{z}^*),\tag{V-33}$$

then the coherence is calculated between W_1 and

$$W_3 = W_2 e^{i\gamma} = U_3(\tilde{z}^*) + iV_3(\tilde{z}^*)\tag{V-34}$$

We then obtain the following four quantities:

$$\hat{P}U_1U_3 = \frac{PU_1U_3}{[PU_1U_1]^{1/2}[PU_3U_3]^{1/2}} ,$$

$$\hat{P}V_1V_3 = \frac{PV_1V_3}{[PV_1V_1]^{1/2}[PV_3V_3]^{1/2}} ,$$

$$\hat{Q}U_1U_3 = \frac{QU_1U_3}{[PU_1U_1]^{1/2}[PU_3U_3]^{1/2}} ,$$

$$\hat{Q}V_1V_3 = \frac{QV_1V_3}{[PV_1V_1]^{1/2}[PV_3V_3]^{1/2}} ,$$

V-35

where $\hat{P}U_1U_3$ is the normalized cospectrum between velocity components U_1 and U_3 , $\hat{Q}U_1U_3$ is the normalized quadrature spectrum between the same components, and $\hat{P}V_1V_3$ and $\hat{Q}V_1V_3$ are the same quantities for the velocity components V_1 and V_3 . PU_1U_1 , PU_3U_3 , PV_1V_1 and PV_3V_3 are the autospectra for U_1 , U_3 , V_1 and V_3 , respectively. All of the above quantities are functions of stretched vertical wave number and the time lag between profiles.

We now describe the actual method of computation. Time lags, T , were calculated for all pairs of drops in the time series. These pairs were then sorted in such a manner that all pairs with lags within $\pm 1/2$ hour of a given whole hour were assigned a lag equal to that whole hour. For example, all pairs with time lags of from $2\ 1/2$ to $3\ 1/2$ hours were given a lag equal to 3 hours for the calculation. Calculations were done only for those lags which had four or more pairs of drops. The results of these calculations are

shown in Figures 24, 25, 26 and 27 for lags up to almost two days. For any lag at which the calculation was made, there are three points shown for each of the four normalized spectral quantities given above. Each of these points represents an average over all pairs available at that time lag. In addition, estimates have been averaged over several stretched vertical wave number bands. The number n represents the number of the stretched vertical wave number estimate; that is, the vertical wave length is given by $1800/n$ sdb, where 1800 sdb is the total length of the series. Thus, the three points (at a given lag and for a given quantity) are averages over stretched vertical wave number estimates $n = 1-5$, $n = 6-10$, and $n = 11-15$.

It is somewhat difficult to put error bars on $\hat{P}U1U3$, $\hat{P}V1V3$, $\hat{Q}U1U3$ and $\hat{Q}V1V3$ since each point may be the result of averaging over a different number of pairs of drops. In an attempt to estimate the error we have calculated $\hat{P}U1U3$, $\hat{P}V1V3$, $\hat{Q}U1U3$ and $\hat{Q}V1V3$ separately for each pair of profiles in a case when four pairs of profiles were used to give the estimates shown in Figures 24-27. (We recall that the smallest number of pairs used was four.) The resulting values of $\hat{P}U1U3$, $\hat{P}V1V3$, $\hat{Q}U1U3$ and $\hat{Q}V1V3$ have an average standard deviation about their mean values of about ± 0.2 . Presumably, points which are obtained by averaging over more than four pairs of drops are even more stable; that is, the scatter of points about their mean values is less than ± 0.2 standard deviation.

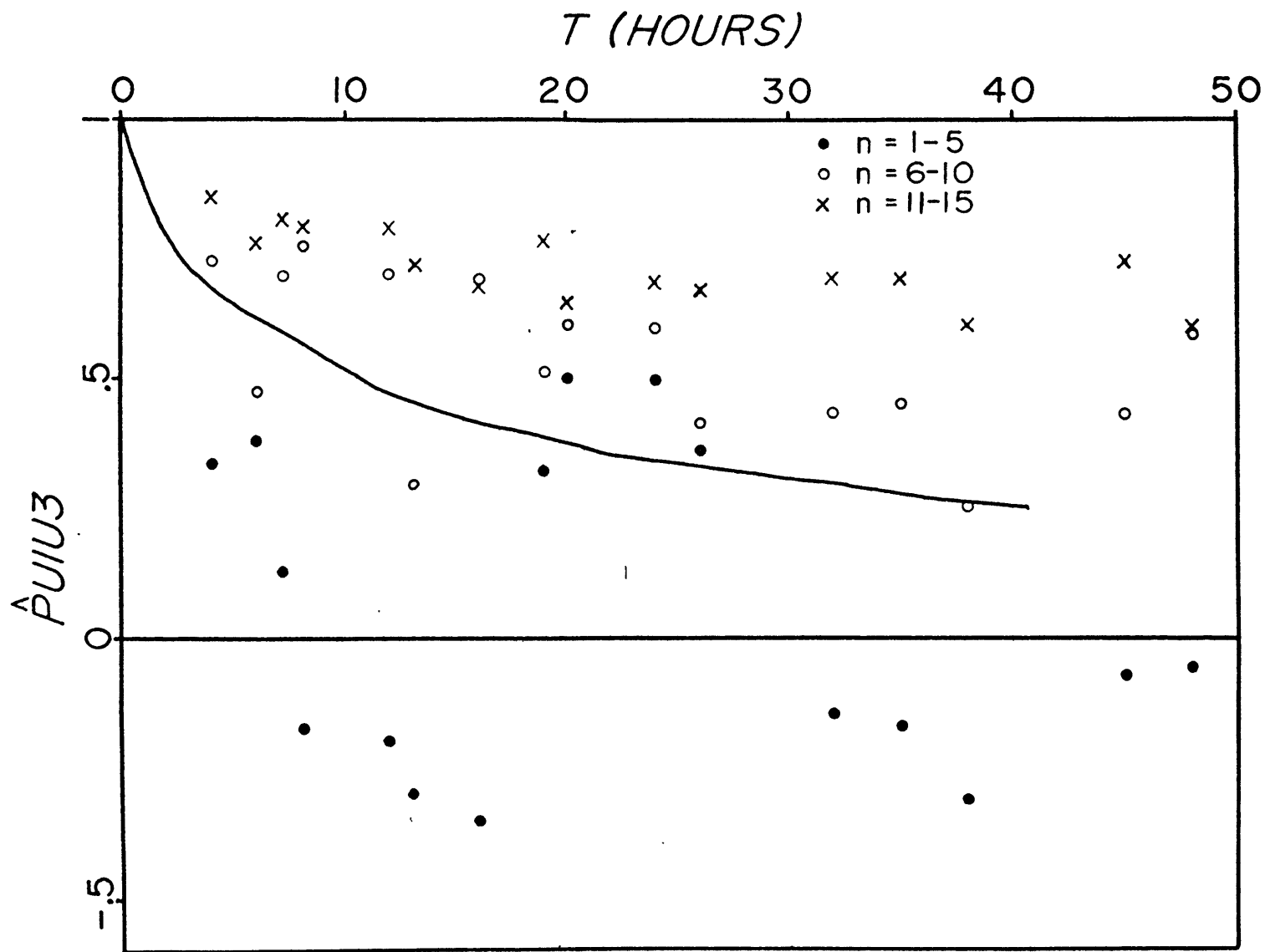


Figure 24. Dropped, lagged, rotary cospectrum (normalized) between velocity components U_1 and U_3 (see text for a further description of Figures 24 to 27).

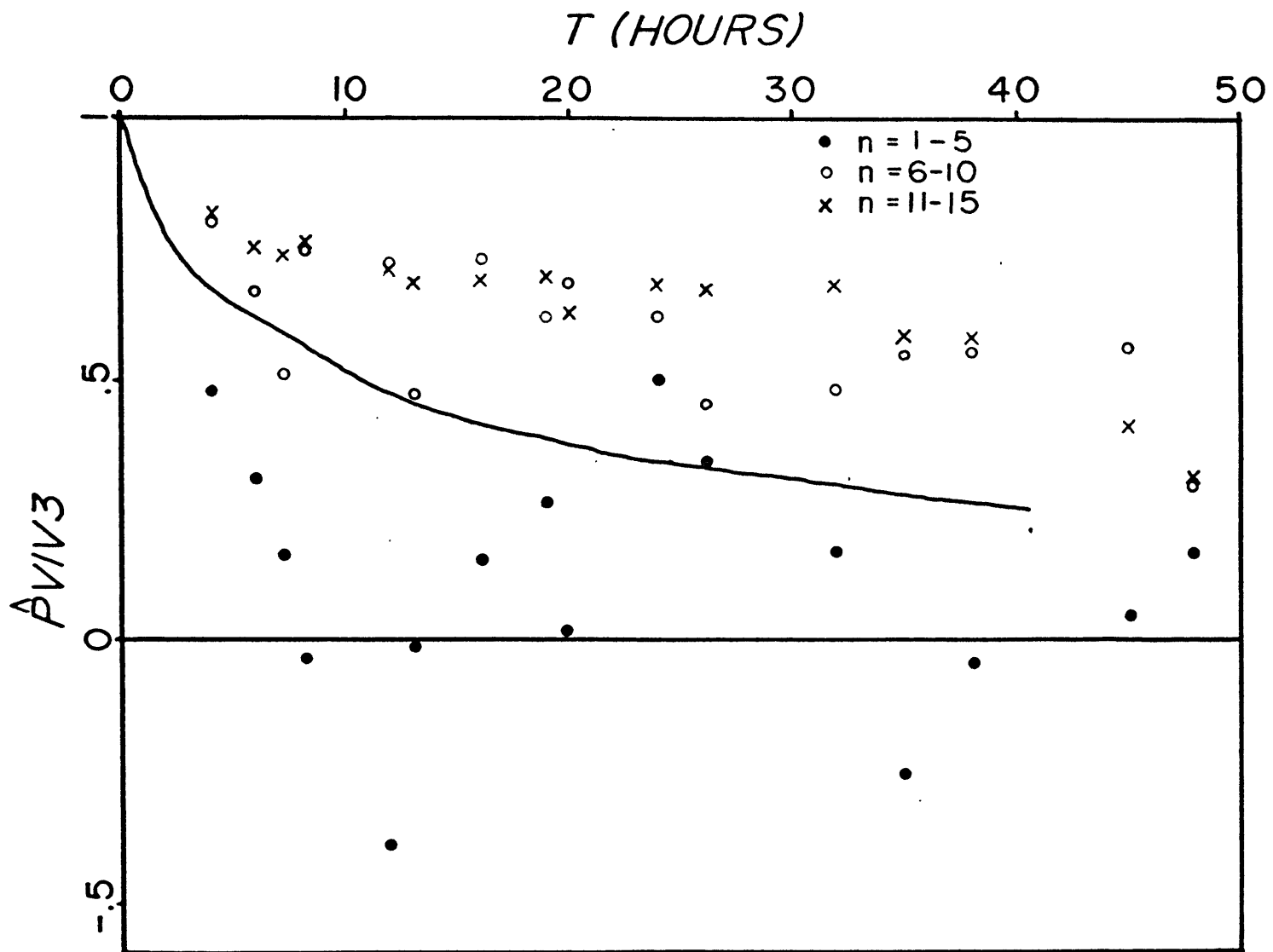


Figure 25. Dropped, lagged, rotary cospectrum (normalized) between velocity components V_1 and V_3 .

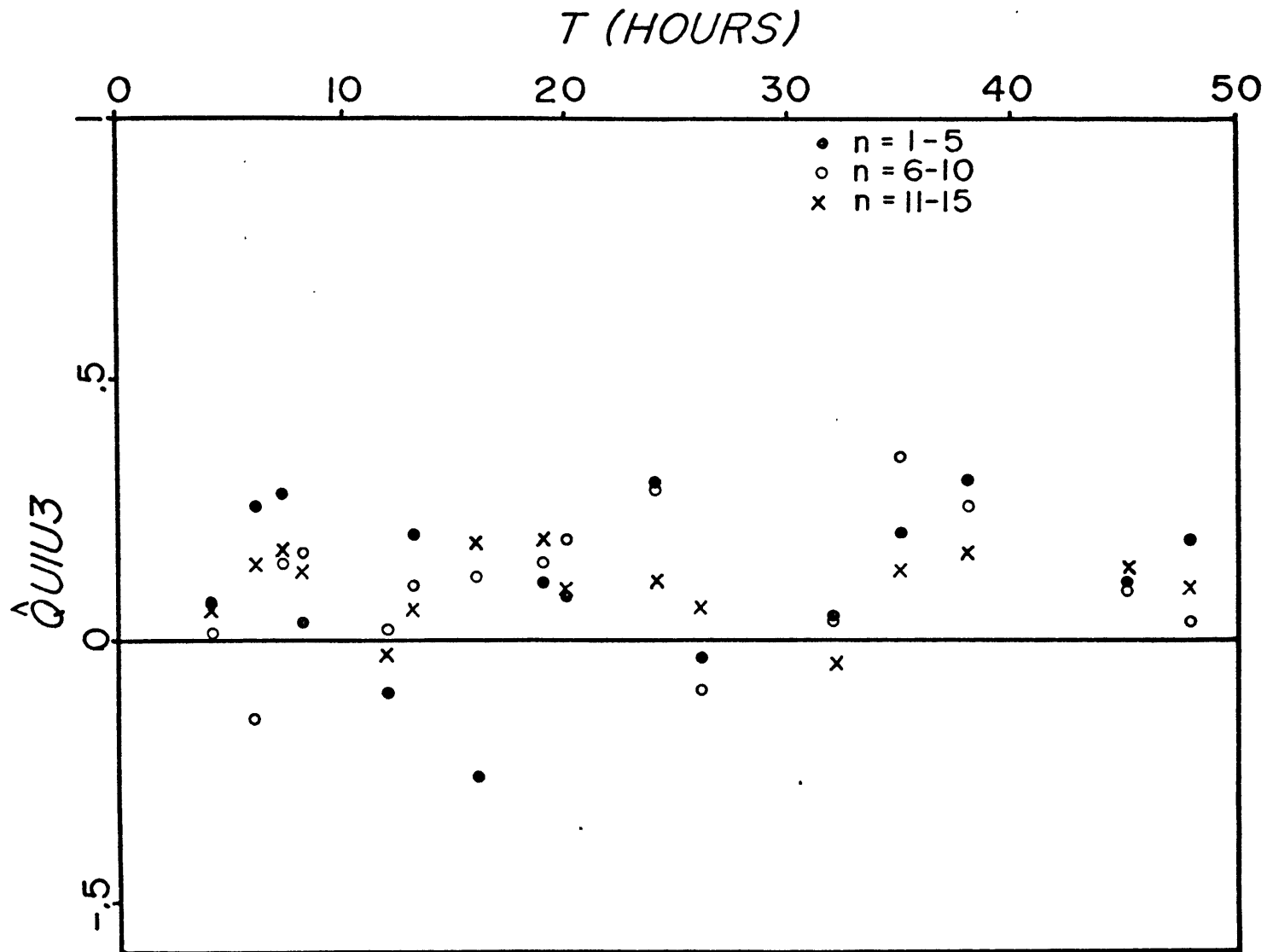


Figure 26. Dropped, lagged, rotary quadrature spectrum (normalized) between velocity components U_1 and U_3 .

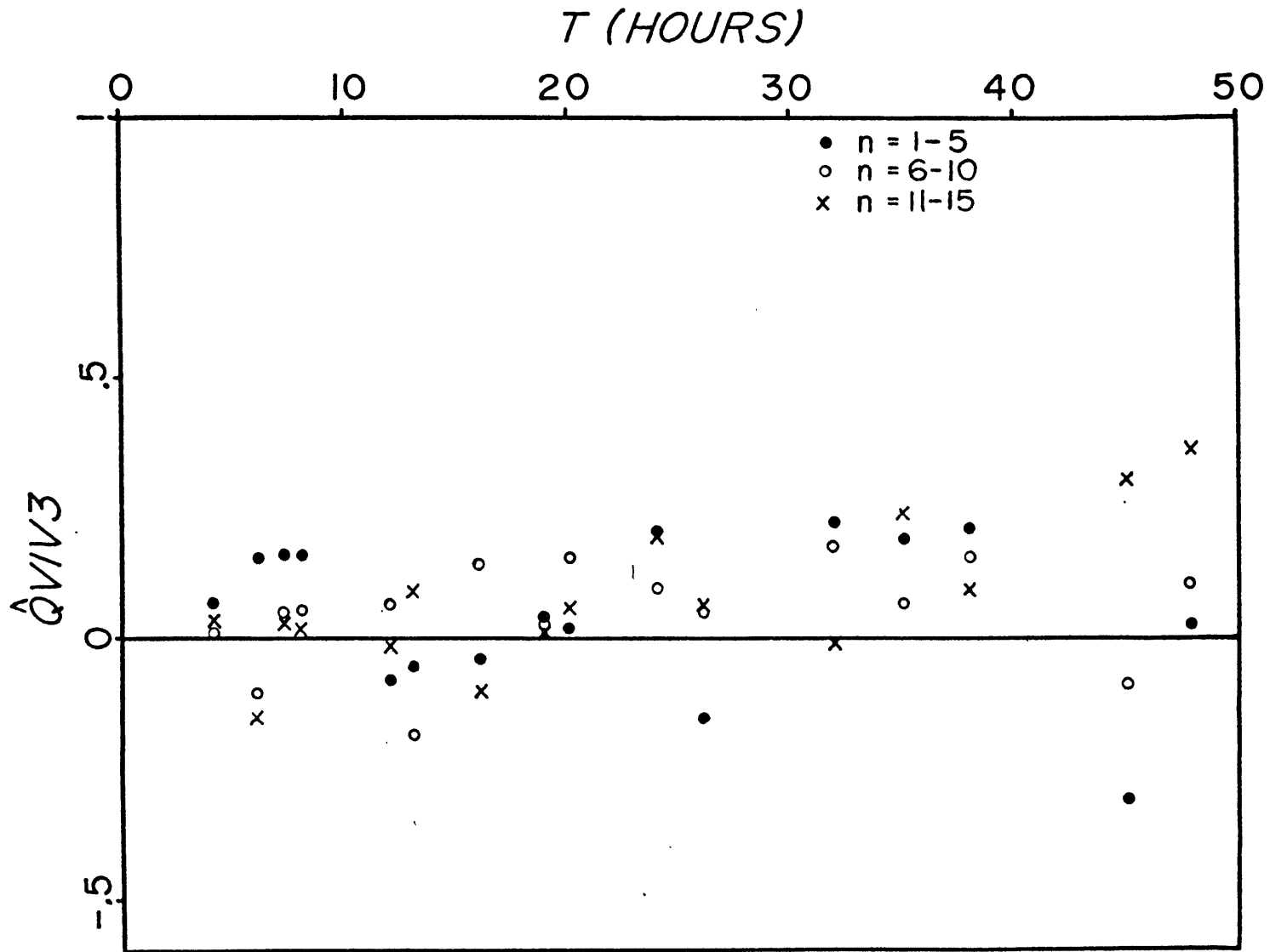


Figure 27. Dropped, lagged, rotary quadrature spectrum (normalized) between velocity components V_1 and V_3 .

Figures 24 and 25 also show the curve of $\hat{P}U1U3$ or $\hat{P}V1V3$ obtained theoretically (C. Garrett, 1974, personal communication) from the Garrett-Munk model under the assumption of an isotropic spectrum. The curve for $\hat{P}U1U3$ or $\hat{P}V1V3$ does not depend on wave propagation in the vertical. In contrast, $\hat{Q}U1U3$ and $\hat{Q}V1V3$ do depend on vertical propagation. If only vertical modes exist, $\hat{Q}U1U3$ and $\hat{Q}V1V3$ are theoretically always equal to zero. On the other hand, if all waves are propagating energy downward, the theoretical curve for $\hat{Q}U1U3$ or $\hat{Q}V1V3$ starts out at zero for zero lag and slowly increases to about + 0.25 for a lag of 50 hours. If we accept the above "confidence limit" of ± 0.2 , it is difficult to say whether the observed values of $\hat{Q}U1U3$ and $\hat{Q}V1V3$ are significantly different from zero. Therefore, the following paragraphs will be limited to a discussion of the observed behavior of $\hat{P}U1U3$ and $\hat{P}V1V3$. These quantities appear to contain the most interesting information on the behavior of the DLRC with varying time lag and stretched vertical wave number.

Using the above error estimate, it is possible to say several things about $\hat{P}U1U3$ and $\hat{P}V1V3$. First, the behavior of $\hat{P}U1U3$ or $\hat{P}V1V3$ for estimates containing the largest vertical wave lengths ($n = 1-5$) is significantly different from the behavior of these quantities for shorter vertical wave lengths ($n = 6-10$ and $11-15$). The estimates for $n = 1-5$ decrease much more rapidly with increasing lag than the estimates for higher n . In fact, the observed $\hat{P}U1U3$ and $\hat{P}V1V3$ curves for $n = 1-5$ have an oscillatory

character with minima (greatest negative values) for lags of about 12 hours, and again for lags of about 30-40 hours. This is a strong indication that the longest vertical wave lengths have significant energy contributions from waves with periods near 12 hours. The most obvious candidate for this energy contribution is, of course, the baroclinic semidiurnal tide. In contrast, the estimates for higher n show little evidence of energy contributions at approximately 12 hour periods. This implies that most of the semidiurnal tidal energy is in the longest vertical wave lengths. Other work (Hendry, 1974) has shown that the baroclinic, semidiurnal tide has most of its energy in the lowest three vertical modes. The above result appears to confirm this.

Second, $\hat{P}U1U3$ and $\hat{P}V1V3$ for higher n ($n = 6-10, 11-15$) follow the theoretical curve more closely. Given the above "error" estimate, $\hat{P}U1U3$ and $\hat{P}V1V3$ curves for $n = 6-10$ and $n = 11-15$ cannot, in general, be distinguished. The theoretical curve does not depend on stretched vertical wave number, but the error is probably large enough so that dependence on vertical wave number cannot be tested adequately. It is interesting to note that $\hat{P}U1U3$ and $\hat{P}V1V3$ for $n = 6-10, 11-15$ are almost always greater than the theoretical curve. A possible explanation for this is that while the theoretical curve takes into account all internal wave frequencies (from inertial to Brunt-Väisälä), the sensitivity of the profiles is such that higher frequency internal waves are "filtered out." These higher frequencies tend to make $\hat{P}U1U3$ or $\hat{P}V1V3$ decrease more

rapidly with increasing lag than would be true if only near-inertial waves were being observed. The results of this section may be summarized as follows: 1.) The behavior of $\hat{P}U1U3$ and $\hat{P}V1V3$ for wave lengths outside of the region in which semidiurnal tidal energy is significant does not appear to refute the theoretical calculations, taking into account the possible sources of error described above. 2.) The result of other calculations, showing that most of the semidiurnal tidal energy is confined to the largest vertical wave lengths, is also obtained from the present calculations.

c.) The vertical energy flux of near-inertial waves

We have pointed out that, because of the relatively short time interval over which the time series was obtained, it is difficult to obtain good frequency resolution for the observed waves. However, there are several independent characteristics of the data which lead us to believe that the waves which we have been calling "inertial" actually have periods somewhat shorter than the inertial period.

First, Figures 6 and 7 indicate that the phases of the dominant waves are moving upward in time. If these waves were of exactly inertial frequency, internal wave theory indicates that the phase should remain at the same depth, independently of time. In order to propagate upward, these waves must have frequencies greater than f .

Second, consideration of Figure 18 shows that many of the more energetic velocity features which can be identified between drops 235U and 236U (these drops being separated by 4.8 kilometers) do not occur at the same depth in both profiles, but rather are offset slightly. This depth offset is too large to be accounted for by errors in the EMVP pressure calibration. The implication is that the phase planes of these waves are tilted slightly away from horizontal. Figure 21 then indicates that the wave number vector, \vec{k} , for these waves must be tilted at a small angle to the vertical, and equation III-10 shows that the wave frequency, $\hat{\omega}$, has to be slightly greater than \hat{f} .

The third indication that the wave frequencies are somewhat greater than \hat{f} comes from attempts to least-squares fit sinusoidal waves to the data. At any pressure, \tilde{z}_n , it is possible to fit sinusoids of the form:

$$\begin{aligned} u_{\text{fit}}(\tilde{z}_n, t_i) &= A(\tilde{z}_n) \sin(\phi(\tilde{z}_n) + \hat{\omega}t_i) , \\ v_{\text{fit}}(\tilde{z}_n, t_i) &= B(\tilde{z}_n) \sin(\psi(\tilde{z}_n) + \hat{\omega}t_i) \end{aligned} \quad \text{V-36}$$

over a group of profiles. t_i is the time of a given profile. u and v are east and north velocity components. Then the quantities

$$U(\tilde{z}_n) = \sum_i (u_{\text{fit}}(\tilde{z}_n, t_i) - u_{\text{obs}}(\tilde{z}_n, t_i))^2 \quad \text{V-37}$$

and

$$V(\tilde{z}_n) = \sum_i (v_{\text{fit}}(\tilde{z}_n, t_i) - v_{\text{obs}}(\tilde{z}_n, t_i))^2 \quad \text{V-38}$$

give an estimate of the residual error in the fit at depth \tilde{z}_n . These fits can then be calculated over a range of depths, \tilde{z}_n . The quantity

$$D = \sum_{z_n} U(\tilde{z}_n) + V(\tilde{z}_n) \quad \text{V-39}$$

represents a measure of the total residual error of the fit over the time and depth interval studied. Attempts to do such fits in the main thermocline, where the strongest signal is found, indicate that the total residual, D , is minimized if the period, T , used in the above formulas ($\hat{\omega} = 2\pi/T$) is slightly less than the inertial period. In fact, the best fit occurs if we choose $\hat{\omega}$ so that $T = 22$ - 23 hours. The inertial period is 25.56 hours at the latitude of the profiler time series.

We have argued in previous chapters that the near-inertial waves are propagating their energy downward from the surface. Since waves with frequencies close to \hat{f} have group velocity vectors that are only slightly inclined to the horizontal, it is at first glance surprising that these waves appear to make significant contributions to the energy even in the deep water. It could be argued that those waves which have the maximum (downward) vertical energy flux will be able to penetrate from the surface to the deep ocean most efficiently. This vertical energy flux is given by

$$\hat{F}_z = \hat{C}g_z \cdot \bar{E} \quad \text{V-40}$$

where $\hat{C}g_z$ is the vertical component of the group velocity vector,

and \bar{E} is the total (kinetic and potential) wave energy. It is of interest to obtain the local \hat{c}_{g_z} , as a function of z , and use it, along with the theoretical energy spectrum of the previous section, to calculate \hat{F}_z as a function of frequency and vertical wave number.

Because the derivation of the Garrett-Munk spectrum assumes that a WKB-type description of the wave behavior is adequate, we will assume in what follows that this is again true. The equations to be solved are the same as equations B-6, except that now \hat{N} is a function of depth. The equation for the vertical velocity, \hat{w} , is:

$$\frac{d^2 \hat{w}}{dz^2} + \beta^2 (\hat{N}^2(z) - \hat{\omega}^2) \hat{w} = 0 \quad \text{V-41}$$

with

$$\beta^2 = \frac{\hat{k}^2 + \hat{\gamma}^2}{\hat{\omega}^2 - \hat{f}^2} \quad \text{V-42}$$

To obtain the WKB solution, we let

$$\hat{w} = e^{\beta \int \chi(z) dz} \sum_{n=0}^{\infty} \frac{\hat{A}_n(z)}{\beta^n} \quad \text{V-43}$$

The solutions for $n = 0$ and $n = 1$ give, respectively, χ and \hat{A}_0 :

$$\chi = \pm i [\hat{N}^2(z) - \hat{\omega}^2]^{1/2} \quad \text{V-44}$$

and

$$\hat{A}_0 = \frac{1}{[\hat{N}^2 - \hat{\omega}^2]^{1/4}} \quad \text{V-45}$$

Then

$$\hat{w} = \frac{1}{[\hat{N}^2(z) - \hat{\omega}^2]^{1/4}} e^{\pm i \sqrt{\frac{\hat{k}^2 + \hat{\gamma}^2}{\hat{\omega}^2 - \hat{f}^2}} \int_{z_0}^z (\hat{N}^2 - \hat{\omega}^2)^{1/2} dz} \quad \text{V-46}$$

where the region of integration is over an interval of z for which $\hat{N}^2(z) > \hat{\omega}^2$. From continuity, we get \hat{u} and \hat{v} :

$$\begin{aligned} \hat{u} &= (\mp \hat{\omega} \hat{k} \mp i \hat{f} \hat{l}) \\ \hat{v} &= (\pm i \hat{k} \hat{f} \mp \hat{\omega} \hat{l}) \end{aligned} \left. \vphantom{\begin{aligned} \hat{u} \\ \hat{v} \end{aligned}} \right\} \frac{(\hat{N}^2(z) - \hat{\omega}^2)^{1/4}}{\hat{\omega}(\hat{\omega}^2 - \hat{f}^2)^{1/2}(\hat{k}^2 + \hat{l}^2)^{1/2}} e^{\pm \beta \int_{z_0}^z \chi(z) dz} \quad \text{V-47}$$

The buoyancy is

$$\hat{b} = \frac{1}{i \hat{\omega} (\hat{N}^2 - \hat{\omega}^2)^{1/4}} e^{\pm \beta \int_{z_0}^z \chi dz} \quad \text{V-48}$$

The total energy, \bar{E} , is given by

$$\begin{aligned} \bar{E} &= 1/2 \left(\langle |\hat{u}|^2 + |\hat{v}|^2 + |\hat{w}|^2 + \frac{|\hat{b}|^2}{\hat{N}^2} \rangle \right) \\ &= 1/4 \frac{(\hat{N}^2 - \hat{\omega}^2)^{1/2}}{\hat{\omega}^2} \frac{\hat{\omega}^2 + \hat{f}^2}{\hat{\omega}^2 - \hat{f}^2} + \frac{\hat{\omega}^2 + \hat{N}^2}{\hat{\omega}^2 (\hat{N}^2 - \hat{\omega}^2)^{1/2}}, \quad \text{V-49} \end{aligned}$$

where the angle brackets denote an average over time. The ratio of vertical kinetic energy plus potential energy to horizontal kinetic energy is:

$$\frac{\text{vert. K.E.} + \text{P.E.}}{\text{horiz. K.E.}} = \frac{(\hat{N}^2 + \hat{\omega}^2) (\hat{\omega}^2 - \hat{f}^2)}{(\hat{N}^2 - \hat{\omega}^2) (\hat{\omega}^2 + \hat{f}^2)} \quad \text{V-50}$$

For frequencies close to \hat{f} , almost all of the energy appears as horizontal kinetic energy. The vertical component of the group velocity vector at depth z is

$$\hat{c}_{g_z}(\hat{m}, \hat{\omega}, z) = \left. \frac{\partial \hat{\omega}}{\partial \hat{m}} \right|_z = - \frac{(\hat{\omega}^2 - \hat{f}^2) (\hat{N}^2 - \hat{\omega}^2)}{\hat{m}(z) \hat{\omega} (\hat{N}^2 - \hat{f}^2)} \quad \text{V-51}$$

The theoretical spectrum of Garrett and Munk has already been given (equation V-24). This spectrum contains only horizontal kinetic energy. However, equation V-50 shows that for frequencies close to \hat{f} , most of the wave energy is horizontal kinetic energy. From equation V-24, the energy density spectrum is

$$\hat{E}_{\hat{m}', \hat{\omega}}(\hat{m}', \hat{\omega}) = \hat{\rho} C \frac{N_0^2}{M_0^3} A \left(\frac{\hat{m}'}{j_* \pi M_0} \right) \frac{\hat{\omega}^2 + \hat{f}^2}{\hat{\omega}^3 (\hat{\omega}^2 - \hat{f}^2)^{1/2}} \quad \text{V-52}$$

The vertical energy flux for waves in a small interval of frequency-stretched vertical wave number space $\Delta \hat{m}' \Delta \hat{\omega}$ is

$$\hat{F}_z = \hat{C} g_z \frac{\hat{N}(z)}{N_0} \hat{E}(\hat{m}', \hat{\omega}) \Delta \hat{m}' \Delta \hat{\omega}, \quad \text{V-53}$$

where \hat{m}' and $\hat{\omega}$ are taken to be in the middle of the element $\Delta \hat{m}' \Delta \hat{\omega}$. The vertical group velocity can be expressed in terms of $\hat{\omega}$ and \hat{m}' by using equation V-12

$$\hat{C} g_z (\hat{\omega}, \hat{m}', \tilde{z}) = - \frac{N_0}{\hat{N}(\tilde{z})} \frac{(\hat{\omega}^2 - \hat{f}^2) (\hat{N}^2 - \hat{\omega}^2)}{\hat{m}' \hat{\omega} (\hat{N}^2 - \hat{f}^2)} \quad \text{V-54}$$

Then

$$\hat{F}_z = - \hat{\rho} C \frac{N_0^2}{M_0^3} A \left(\frac{\hat{m}'}{j_* \pi M_0} \right) \frac{(\hat{\omega}^2 + \hat{f}^2) (\hat{N}^2 - \hat{\omega}^2) (\hat{\omega}^2 - \hat{f}^2)^{1/2}}{\hat{m}' \hat{\omega}^4 (\hat{N}^2 - \hat{f}^2)} \Delta \hat{m}' \Delta \hat{\omega}. \quad \text{V-55}$$

We note that for $\hat{\omega}$ close to \hat{f} , \hat{F}_z is almost independent of \tilde{z} .

From the WKB approximation, it can be shown that

$$\frac{\partial \hat{F}_z}{\partial z} = \frac{\partial}{\partial z} (C g_z \cdot \bar{E}) = 0. \quad \text{V-56}$$

However, since we are only considering horizontal kinetic energy, $\partial F_z / \partial z$ is not equal to zero but approaches zero as $\hat{\omega}$ approaches \hat{f} .

We are particularly interested in examining \hat{F}_z as a function of $\hat{\omega}$, for fixed \hat{m}' . The frequency dependence of \hat{F}_z is given by

$$g(\hat{\omega}) = \frac{(\hat{\omega}^2 + \hat{f}^2) (\hat{\omega}^2 - \hat{f}^2)^{1/2} (\hat{N}^2 - \hat{\omega}^2)}{\hat{\omega}^4 (\hat{N}^2 - \hat{f}^2)}$$

$$\approx \frac{(\hat{\omega}^2 + \hat{f}^2) (\hat{\omega}^2 - \hat{f}^2)^{1/2} (1 - \frac{\hat{\omega}^2}{\hat{N}^2})}{\hat{\omega}^4}, \quad \text{V-57}$$

since $\hat{N} \gg \hat{f}$. If $\hat{\omega}$ and \hat{N} are made non-dimensional by

$$\tilde{\omega} = \frac{\hat{\omega}}{\hat{f}}, \quad N = \frac{\hat{N}}{\hat{f}} \quad \text{V-58}$$

then

$$\underline{f}(\tilde{\omega}) = \hat{f}g(\tilde{\omega}) = \frac{(\tilde{\omega}^2 + 1) (\tilde{\omega}^2 - 1)^{1/2} (1 - \frac{\tilde{\omega}^2}{N^2})}{\tilde{\omega}^4} \quad \text{V-59}$$

$\underline{f}(\tilde{\omega})$ is plotted in Figure 28, with $\hat{N} = 5\hat{f}$. It can be seen that $\underline{f}(\tilde{\omega})$ increases rapidly with increasing $\tilde{\omega}$ until $\tilde{\omega} = 1.2$, and then decreases. This implies that, for fixed \hat{m}' , \hat{F}_z reaches a maximum for $\hat{\omega} = 1.2\hat{f}$. For an inertial period of 25.56 hours, the vertical flux of horizontal kinetic energy reaches a maximum (at a given \hat{m}') for waves with periods of around 21 hours. This period appears to be somewhat shorter than that which might have been expected. (We recall that the least-square fit indicated that the dominant waves in the profiles seemed to have periods of 22-24 hours in the main

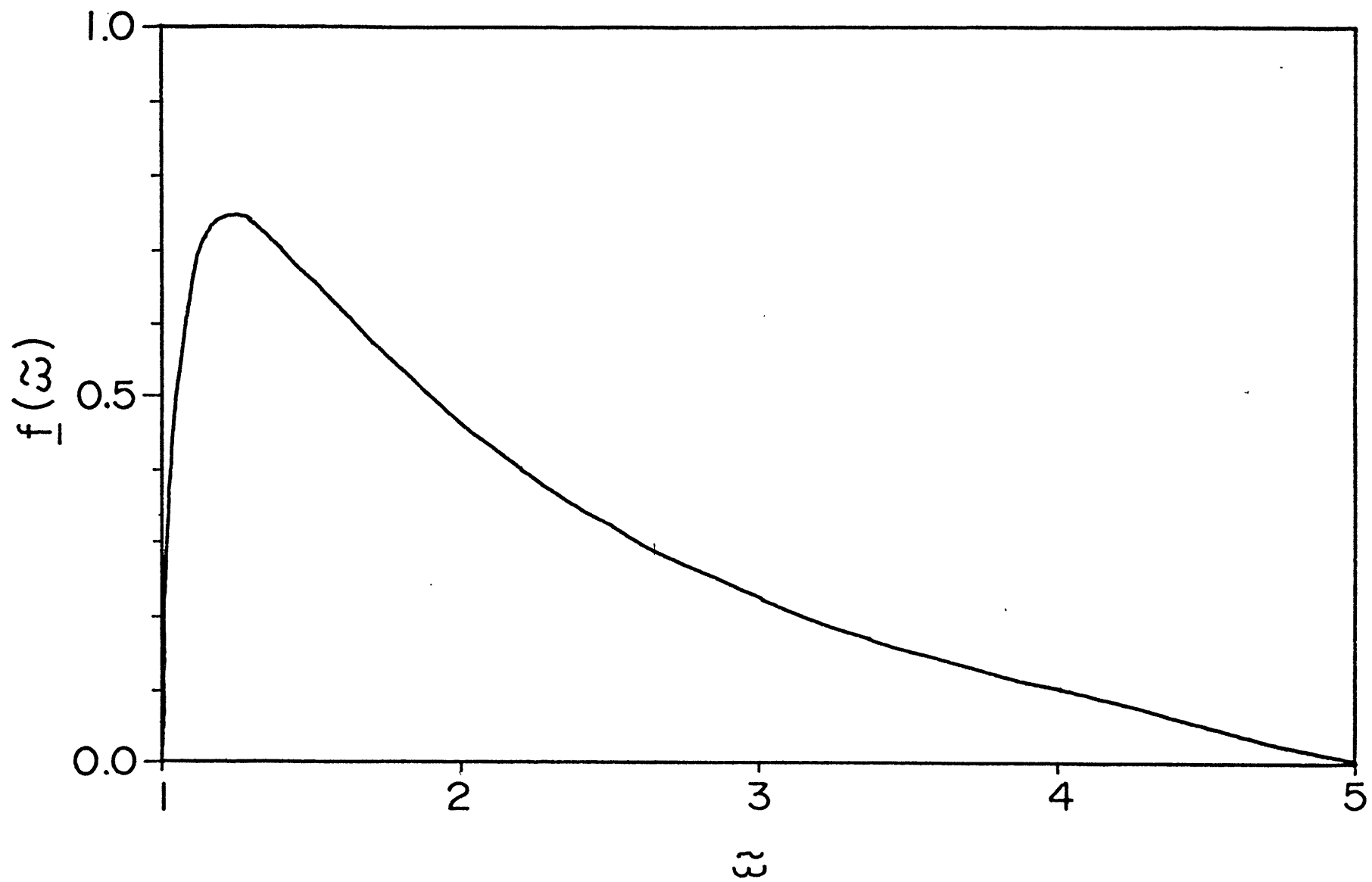


Figure 28. Frequency dependence of the vertical flux of horizontal kinetic energy, using a theoretical form for the energy spectrum of the internal wave field.

thermocline.) However, it is significant that the downward energy flux appears to have its maximum value close to the local inertial frequency in this model.

A certain amount of inconsistency is inherent in using a spectrum such as the Garrett-Munk model to calculate energy flux. The first point of inconsistency, of course, is that the true spectrum will not have an infinity at the inertial frequency. This problem could be removed by assuming, for example, that there should really be an energy cut-off near the inertial frequency; that is, instead of the infinity at the inertial frequency, the spectrum could be altered locally (at and near f) so that a simple peak occurs at the inertial frequency. This alteration would not change the flux curve of Figure 28 appreciably. In fact, it would force the observed flux maximum to be concentrated even more about periods of 21-22 hours. The second problem is more subtle, and involves the question of why one would expect the spectral peak to be exactly at the inertial frequency. In a case (such as the Garrett-Munk model) where vertical modes have been assumed to have been established a priori, it seems that a peak at the inertial frequency would not be inconsistent, since the waves are not required to be supported by energy sources located, for example, at the surface or bottom boundaries. However, once we require that the waves be supported by a flux of energy into the ocean from the surface (or bottom) boundary it is not consistent to expect that the peak in the observed energy spectrum at some depth will be

found at that frequency (f) where the vertical energy flux becomes zero. Both of the above points argue that the "inertial peak" should actually appear at frequencies somewhat greater than f .

Figure 29 shows a frequency spectrum obtained from averaging spectra of current meter records at 1500 meters at 12 different locations in the MODE region (M. Briscoe, 1975, personal communication). The average inertial frequency of the 12 locations is also shown. (The maximum and minimum inertial frequencies of the 12 locations are about ± 0.002 cph about the average inertial frequency.) It is clear from Figure 29 that the inertial "peak" is displaced toward frequencies greater than f . The center of this wide peak is in the period range 22-23 hours, in agreement with the above discussion.

It is possible to use the above expression for the vertical group speed (equation V-54) along with the observed stretched vertical wave number spectrum (Figure 16) to calculate a rough estimate of the vertical energy flux (downward and net), integrated over all vertical wave numbers. In the absence of accurate frequency information, we have assumed that the clockwise and counterclockwise spectra are dominated by waves with periods of the calculated maximum flux (or of the center of the near-inertial "peak" in Figure 29); that is, periods of 22-23 hours. Using this period range in the expression for the vertical group speed, and assuming that roughly half the energy in the clockwise and counterclockwise energy estimate for the smallest two or three stretched vertical wave

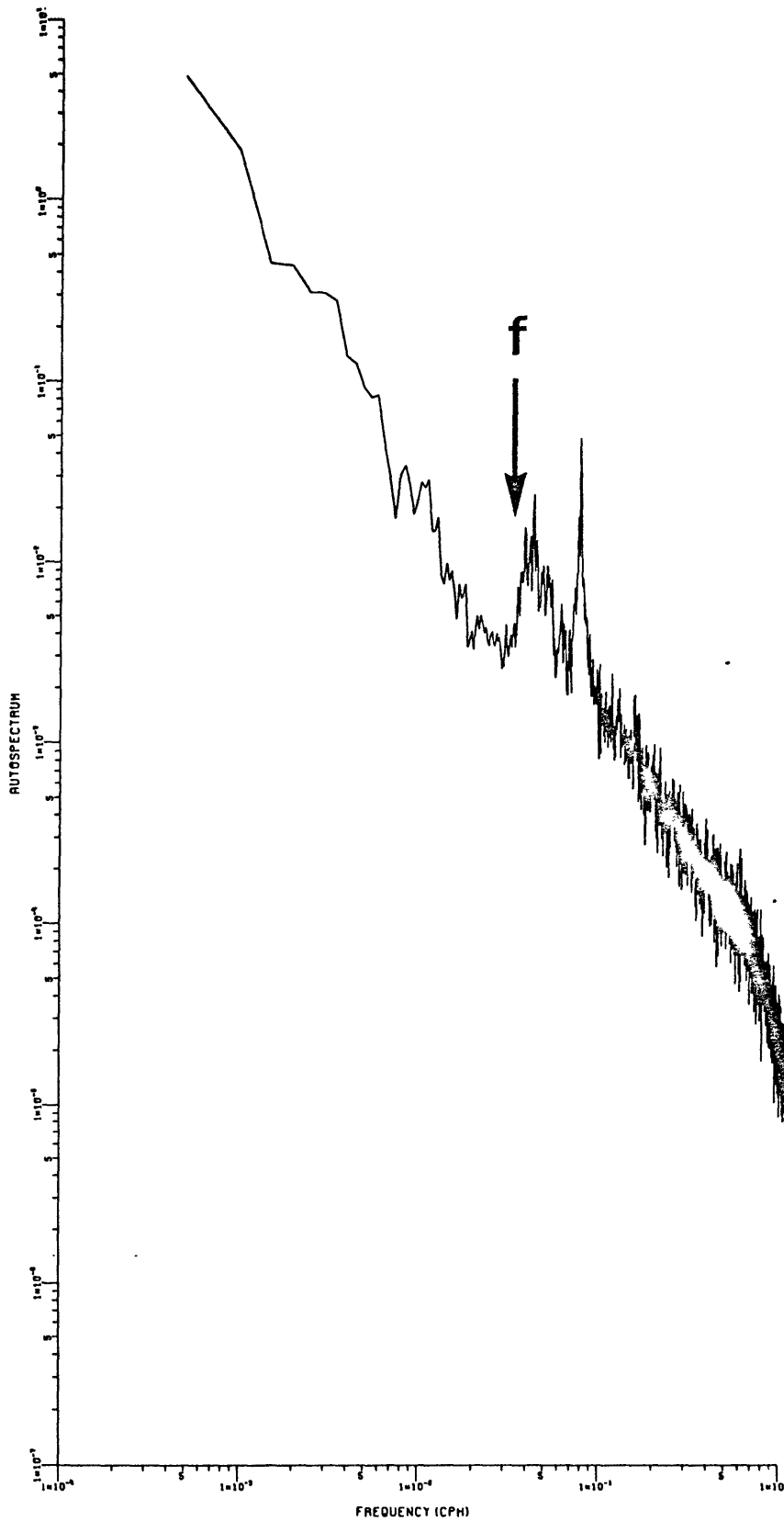


Figure 29. Frequency spectrum, obtained by averaging 12 spectra computed from current meter records at 1500 m in the MODE region. Energy density units are $(\text{cm}/\text{sec})^2/\text{cph}$. f is the inertial frequency.

number estimates is contributed by the semidiurnal tide (see Chapter V-b), we obtain estimates of the total downward wave energy flux of 0.6-1.0 erg/cm²/sec, and of the net downward wave energy flux of 0.2 - 0.3 erg/cm²/sec. The estimate of the total downward flux is consistent with other estimates of vertical energy flux by internal waves (Bell, 1975). We have suggested in previous chapters that a bottom boundary layer could be a significant energy sink for near-inertial waves. An order-of-magnitude calculation indicates that a net downward energy flux of 0.2 - 0.3 erg/cm²/sec could be matched by energy loss in a boundary layer. A measure of this possible energy loss is

$$L = 4K_v\rho\left(\left(\frac{\Delta u}{\Delta z}\right)^2 + \left(\frac{\Delta v}{\Delta z}\right)^2\right) \Delta z \text{ erg/cm}^2/\text{sec} \quad \text{V-60}$$

(Yih, 1969)

where K_v is the coefficient of vertical eddy viscosity, ρ is density, u and v are horizontal velocity components, and Δz is a scale depth of the boundary layer. Choosing values for $\Delta u^2 + \Delta v^2$ and Δz from Figure 8 ($\Delta u^2 + \Delta v^2 \sim 4 \text{ cm}^2/\text{sec}^2$, $\Delta z \sim 5 \times 10^3 \text{ cm}$), we get $L \sim (0.3 \times 10^{-2}) K_v \text{ erg/cm}^2/\text{sec}$. For $K_v = 100 \text{ cm}^2/\text{sec}$, $L \sim 0.3 \text{ erg/cm}^2/\text{sec}$. Bell (1975) quotes a value for K_v of $\sim 10 \text{ cm}^2/\text{sec}$ in the interior but notes that K_v could be at least an order of magnitude larger in a turbulent bottom boundary layer. Thus, the value of K_v needed to make L comparable to the estimated net downward energy flux is not inconsistent with other estimates of K_v .

Chapter VI Some Observations over Rough Topography

In previous chapters we have presented an analysis of data obtained over smooth topography (at the MODE central mooring). Some of the calculations presented, such as reflection coefficients, depend on the assumption that the bottom is not acting as a wave source. Over the smooth topography this does not appear to be an unreasonable assumption. However, it is well known from theoretical studies that a rough bottom may interact with either a mean flow, producing lee waves, or with an oscillatory flow such as a tide. Bell (1975) has discussed the possible generation of internal waves in the open ocean by rough topography. In an earlier work, Hendershott (1964) analyzed a case where inertial waves could be generated by the oscillatory flow of a diurnal-tide component over a rough bottom. His study indicated that strong inertial wave currents might be generated at latitudes slightly to the south of the critical latitude (the latitude at which the tidal and inertial periods are equal). The critical latitude for the 24-hour diurnal tide would be 30° N, for example. His theory actually predicts that there should be a somewhat complicated band structure of the inertial energy south of the critical latitude, with a primary peak in the inertial energy just south of the critical latitude, and secondary maxima farther south.

It is important to realize that there are numerous tidal lines that are called diurnal. Although the critical latitude for the 24-hour tide is 30° N, the critical latitude for the 24-hour 50-minute tide moves down to about 28.9° N. This means that the actual energy levels of the inertial waves (generated by topography) might not depend as strongly on latitude as is predicted by the theory. In any case, the fact that the major diurnal tidal components at 28° N have frequencies within the internal wave frequency range, but near the inertial frequency, indicates that it would be worthwhile to look for near-inertial energy propagating away from the bottom in the rough topography region.

During the MODE experiment, a set of profiles was obtained around a ridge in the rough topography region east of the central mooring. These drops are indicated by a dagger (\dagger) in Appendix A. The center of the ridge is located at approximately $28^\circ 04'$ N, $68^\circ 31'$ W. The main part of the ridge is oriented along the axis NNE-SSW and rises about 700-800 meters above the adjacent, smoother part of the ocean floor. Because this set was obtained in order to make a survey of the velocity structure around the ridge it is not a time series at one location. In fact, the set is made up of a series of pairs of profiles, except in a few cases where only single profiles were made. Each pair was obtained at one location around the ridge, and the second profile was usually taken at about one half of an inertial period after the first profile. Because a time series of profiles is not available over the rough topography, it

is difficult to accurately remove the low-frequency shear profile. For this reason, the results of calculating clockwise and counterclockwise vertical wave number spectra are more difficult to interpret than are the corresponding results over the smooth topography. However, some significant features in these rough topography profiles can be seen visually; that is, without recourse to spectrum calculations.

Figures 30 and 31, for example, show hodograph plots (plots of the horizontal velocity vector with depth) for profiles 190D and 192D between 3000 dbar and 4500 dbar. These two profiles were made at a time lag of one half of an inertial period. The original profiles have been smoothed by applying a running 150 dbar triangular filter to each velocity component. This makes it easier to visually follow the behavior of the longer wave length (higher energy) waves in the profiles. Smoothed points are plotted every 10 dbar, and depth is marked every 100 dbar. The most striking feature of these hodographs is that they show wave-like structures for which the horizontal velocity vector is clearly rotating counterclockwise with increasing depth. The structure is clearly time-dependent, as can be seen by comparing the hodographs for profiles 190D and 192D. Comparison of the hodographs appears to indicate that these waves have periods near the inertial period. We have already pointed out in Chapter III that such counterclockwise polarization indicates that these waves are propagating energy upward, away from the ridge.

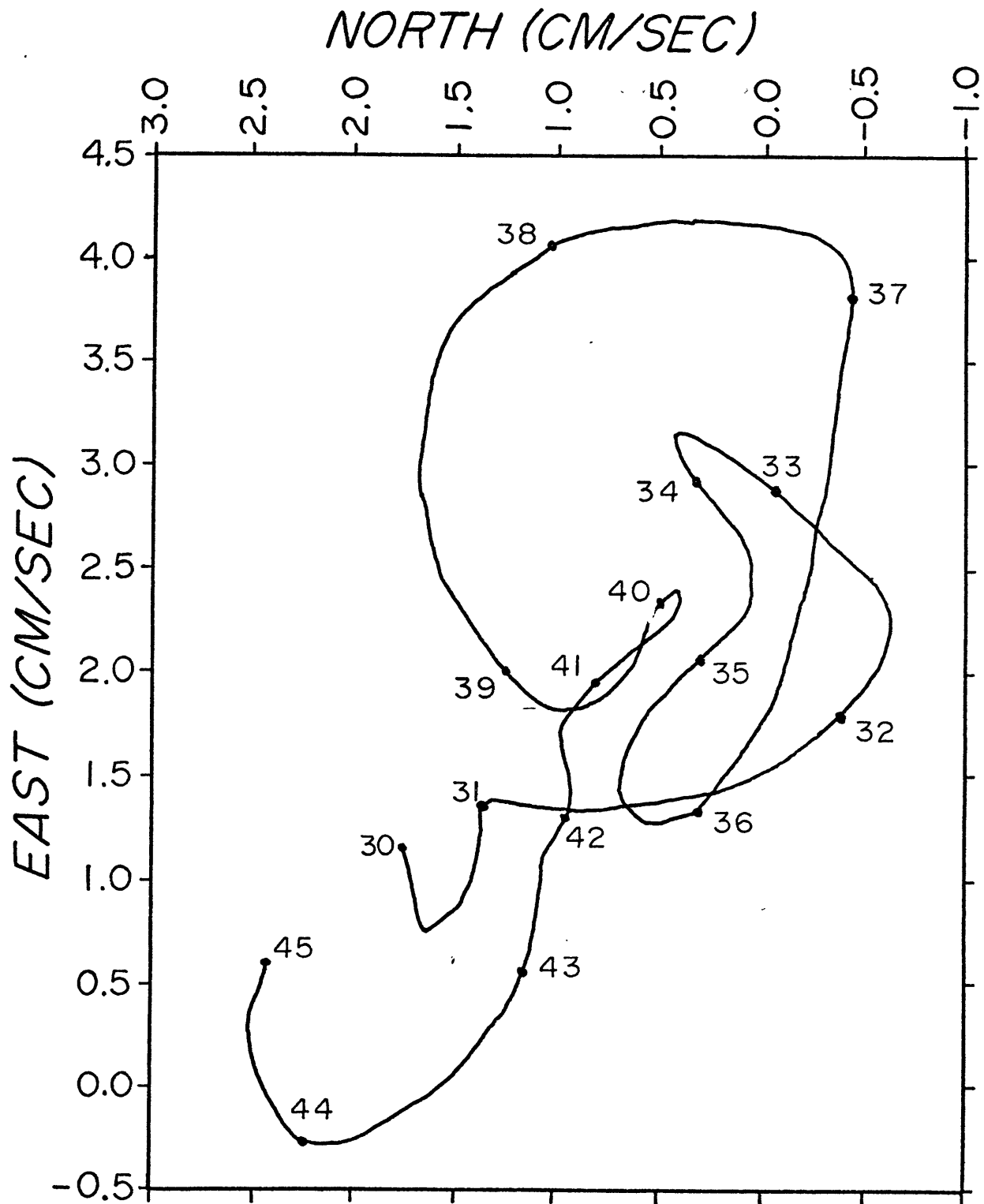


Figure 30. Smoothed hodograph of profile 190D between 3000 dbar and 4500 dbar. Depths are in hundreds of decibars.

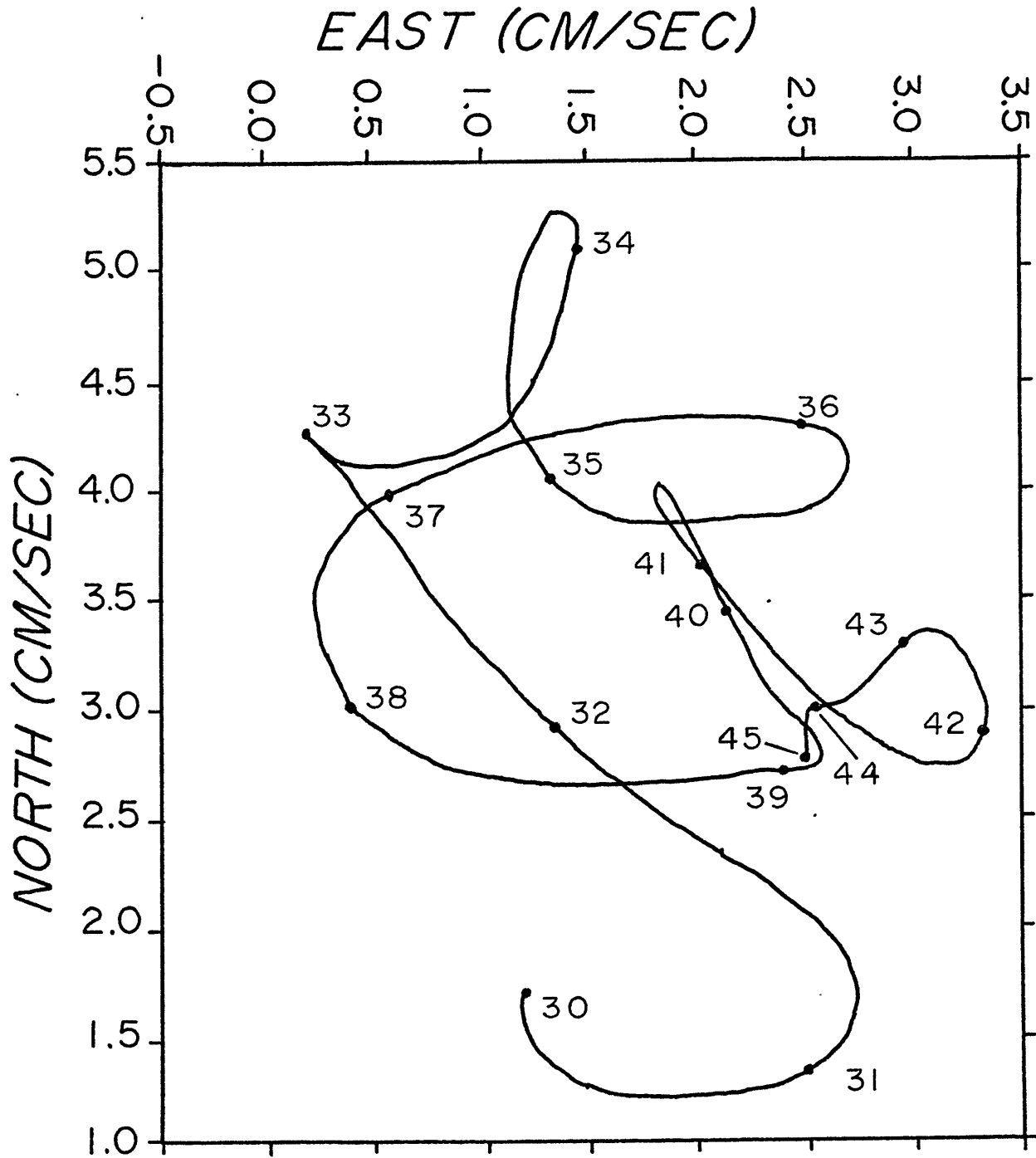


Figure 31. Smoothed hodograph of profile 192D between 3000 dbar and 4500 dbar. Depths are in hundreds of decibars.

Although spectral estimates obtained from only two profiles are probably not very stable, it should be mentioned that vertical wave number spectra (without stretching the vertical coordinate) obtained in the deep water (2000 dbar and deeper) for drops 190D, 191D, 192D and 193D show a consistent dominance of counterclockwise energy over clockwise energy. These four drops were made at the southwest end of the ridge.

In contrast, deeper water (greater than 2000 dbar) spectra and hodographs for a drop pair, 195D and 197D, that was made northeast of the ridge, do not show any strong tendency for counterclockwise rotation with depth. If anything, these drops show a tendency for the velocity vector to rotate clockwise with depth in the same manner as was observed over the smooth topography. Swallow floats located near the ridge when these profiles were made indicated that the mean flow (at 4000 dbar) was to the southwest. Since the pair 195D and 197D was located to the northeast of the ridge while 190D, 191D, 192D and 193D were to the southwest, we might speculate that if the ridge was generating near inertial waves, these waves would be advected to the southwest and therefore would be seen primarily by profiles to the southwest of the ridge. Although it is difficult to draw general conclusions from a small set of profiles, the above observations in the deep water around the ridge can be summarized as follows: profiles made to the southwest of the ridge show clear evidence of counterclockwise polarization with depth; profiles made near the ridge crest (such as 189D, for

example) do not appear to show a dominance of either polarization; two profiles (195D and 197D) made over a smoother region to the northeast of the ridge appear to have reverted to the clockwise polarization with depth characteristic of the smooth topography profiles, at least for the longer vertical wave lengths, which are most energetic.

Bell (1975) has calculated a value for the possible upward energy flux of internal waves generated by rough topography of $\sim 1 \text{ erg/cm}^2/\text{sec}$. This value is comparable to the total downward flux in the smooth topography region, as estimated in Chapter V. If the average vertical energy flux values for bottom topography and sea surface generation are comparable, it might be expected that energy input at the bottom could sometimes exceed energy input at the surface (especially since both input processes are probably intermittent in time). This would result in waves polarized counterclockwise with increasing depth, at least in the deep water over the rough topography. (We have also examined hodographs of the rough topography profiles in the upper half of the water column. In contrast to the plots in the lower half, these hodographs do not show a clear dominance of one polarization over the other, indicating that in the upper half of the water column a complicated addition of the top and bottom energy sources may be taking place.)

Chapter VII Conclusions, a Further Discussion of Some of the Data and Recommendations for Future Experiments

The previous chapters have been devoted to an analysis of internal wave data obtained by vertical profiling. It is now worthwhile to summarize the significant results of this analysis and place these results in the general framework of internal wave theory.

One of the more fruitful results of this analysis has been the ability to relate the observed characteristics of wave polarization and vertical phase propagation to the locations of energy sources for these waves; that is, to the possible existence of internal wave energy sources at the top and bottom boundaries of the ocean. As Muller and Olbers (1975) have pointed out, a two-sided, symmetric, vertical wave number spectrum (equal energy in positive and negative vertical wave numbers) is not consistent with the existence of net boundary sources at the surface and bottom. A major cause of difficulty with internal wave observations until now has been the inability to observe asymmetry of internal wave vertical wave number spectra (or, in fact, vertical wave number spectra) of horizontal velocity with the techniques that have been employed. Time series of horizontal velocity obtained from current meters at fixed locations in space cannot distinguish between an internal wave having an upward or a downward phase propagation,

since the horizontal velocity vector rotates in the same sense for either wave (clockwise in the northern hemisphere). The technique, employed in Chapter II, of decomposing vertical profiles into clockwise and counterclockwise energy contributions is a useful method for observing asymmetry in the internal wave vertical wave number spectrum and for inferring the direction of net vertical energy flux from this asymmetry. A similar instance where vertical wave polarization has been used to infer the direction of vertical energy propagation in the atmosphere has already been pointed out (Hines, 1966). A case where vertical polarization of tidal currents was apparently observed in an analysis of current records obtained from current meters on moorings has been reported by Titov and Fomin (1971). We have mentioned in Chapter III, however, that the ability to identify clockwise and counterclockwise energy with waves having upward and downward wave number vector components (that is, with the two-sided vertical wave number spectrum) requires that the observed energy be primarily contributed by waves with frequencies near the local inertial frequency. This is true because individual waves are nearly circularly polarized if their frequencies are near the local inertial frequency. If a single wave with a frequency much greater than inertial were present, for example, this wave would provide energy contributions to both the clockwise and counterclockwise vertical wave number spectra, since the wave would be elliptically polarized in the vertical. The clockwise energy would still be greater than the counterclockwise

energy if the wave were propagating energy downward. But the true, two-sided vertical wave number spectrum of this wave would contain energy only on one side of the spectrum (at the positive or negative vertical wave number of the wave, depending on which way the phase of the wave is propagating in the vertical).

Fortunately, the data presented and analyzed in previous chapters indicates that the two dominant sources of energy in the profiles are near-inertial waves (at all vertical wave numbers), and the semidiurnal tide (at the smallest vertical wave numbers). Inertial and diurnal tidal contributions to the profiles cannot, however, be resolved because of the short length of time over which the profile time series was obtained. The average frequency spectrum at 1500 meters (Figure 29) shows that a large part of the energy observed at this depth in the internal wave band comes from frequencies near the inertial-diurnal tidal frequency, and from the semidiurnal tide. The observed "mirror-imaging" of profiles (Figure 3) and the calculations of dropped, lagged, rotary coherence (Figures 24 to 27), support this.

The observation that much of the variability in the profiles was caused by the near-inertial waves (and the semidiurnal tide at the largest vertical wave lengths) led to efforts to evaluate quantitatively the total and net downward energy flux over the smooth topography. Making assumptions about the amount of energy contributed by the semidiurnal tide at the smallest vertical wave numbers, we obtained values for the total vertical energy flux downward of

$\sim .6 - 1.0 \text{ erg/cm}^2/\text{sec}$, and for the net vertical energy flux downward of $\sim .2 - .3 \text{ erg/cm}^2/\text{sec}$. Although both estimates are subject to uncertainty because of the presence of the semidiurnal tide, neither estimate seems unreasonable (see Chapter V-c). In particular, it appears that the net downward energy flux can be balanced by a rough estimate of the rate of energy loss per cm^2 in the bottom boundary layer (if we assume, of course, that the observed decrease of mean perturbation horizontal kinetic energy near the bottom is actually caused by the presence of a boundary layer).

In relation to the contour plots (Figures 6 and 7), a further statement can be made which, although somewhat obvious, is no less important. The observed relations among wave period, direction of vertical phase propagation, and vertical wave polarization in Figures 6 and 7 constitute at least a partial verification of the dispersion relation for internal waves (those near the inertial frequency). Other observations and analyses of data (from current meter records, for example) have assumed that the observed oscillations between the inertial and Brunt-Väisälä frequencies obey the dispersion relation for internal waves. In the absence of clear evidence of the propagation of oscillations in this frequency range, other investigators (Webster, 1969, for example) have argued that some other process (such as turbulence) could explain the observed oscillations. Although turbulence is difficult to define, one of its characteristics is that it does not follow a well-defined dispersion relation. In this sense, then, the results

of Figures 6 and 7 clearly argue for internal waves as being the cause of the observed variability in the profiles, at least for the near-inertial waves.

Another significant result brought out by this analysis is the fact that both profiler data and other, independent observations (Figure 29) have shown that the energy concentration in what one might call the "inertial peak" is, first, not concentrated in a well-defined peak (as is the semidiurnal tide, for example) and second, is not concentrated at exactly the inertial peak but is rather centered at a frequency about 20% greater than the local inertial frequency. Some previous observations have also shown that the inertial "peak" is quite often displaced toward frequencies somewhat greater than the local inertial frequency. Webster (1968), for example, shows a frequency spectrum of current at $38^{\circ} 28.8' N$, $70^{\circ} 00.5' W$, in 3300 meter water, with the observations made about 30 meters above the bottom. This spectrum has a clear concentration of energy near the local inertial frequency, but the center of this peak occurs at a frequency about 5% higher than the local inertial frequency. White (1972) considered temperature data obtained in the upper several hundred meters at a site in the Pacific. His temperature spectra always show an inertial "peak" at frequencies up to 30% higher than the local inertial frequency.

Various attempts have been made to explain this shift theoretically. Munk and Phillips (1968), for instance, argued that internal waves generated to the south of a given latitude of

observation (in the norther hemisphere) would propagate northward, and that as they propagated northward their frequencies would approach the local inertial frequency. A test of this idea by the use of profile data would require better information on the direction of horizontal phase propagation for the observed waves. We will return to this question later, when the possible influence of the mean vertical shear on the propagation of the waves seen in the profiles is discussed.

White (1972) pointed out that the observed frequency shift of the inertial waves could be explained as the result of a Doppler shift due to the mean flow. Because he always observed a shift toward higher frequencies, he was forced to conclude that the near-inertial waves he observed were always propagating in the direction of the mean flow. The data presented in previous chapters, however, show that it is unlikely that Doppler shifting could be the cause of the observed frequency shift. The average frequency spectrum at 1500 meters (Figure 29) shows that there is an appreciable (20%) shift of the "inertial peak" toward higher frequencies. But it is known from a calculation of the average flow observed by a current meter at 1500 meters near the location of the five-day time series (Chapter II) that the mean flow at that depth, when the time series was made, was small (< 3 cm/sec). It does not seem that such a small mean flow could account for the observed frequency shift. This does not necessarily negate White's conclusion, since he was observing at a point where the mean flow was

about five times that observed at 1500 meters in the present experiment. It would seem fortuitous, however, that the near-inertial waves would always propagate in the direction of the mean flow, especially if, as the present data indicate, they are being generated by atmospheric forcing at the ocean surface. In fact, there is a suggestion in the data (discussed below) which indicates that at least the more energetic features in the profiles have a component of propagation to the north. Since the mean flow, at least to about 1500 meters, was to the south during the present experiment, this would imply that, if anything, the inertial peak would be shifted to lower frequencies.

The results of the profiler observations now allow us to propose another mechanism to explain why the observed "inertial peak" frequency shift almost always appears to be toward higher frequencies. This explanation is that the observed waves are clearly propagating in the vertical. The contour plots (Figures 6 and 7) show that the dominant structures associated with the near-inertial waves are moving upward in time, corresponding to downward energy propagation. (Of course, these contour plots are influenced by the mean flow. However, we have already pointed out that around 1500 meters the mean flow is small, and yet the greatest speed of upward phase propagation in these contour plots is found in the 1500 dbar to 2500 dbar range.) In order to propagate vertically, these waves must have frequencies greater than the local inertial frequency. The calculations of Chapter V-c showed

that, using an assumed form of the internal wave energy spectrum, the maximum vertical flux of horizontal kinetic energy occurs at frequencies about 20% higher than the inertial frequency. We pointed out that, once the energy sources are placed at the surface (or bottom) boundary, it is inconsistent to have the peak in the energy spectrum appear exactly at the inertial frequency when waves of this frequency cannot propagate into the interior. It is consistent, however, to have an "inertial peak" that is shifted to higher frequencies. It seems likely that the waves which, when generated at the surface, have the greatest downward energy flux would be most able to penetrate through the total water column. (They would presumably be able to travel a greater distance in the vertical before losing an appreciable fraction of their energy due to friction, non-linear interactions, shear interactions, or some other cause.)

We have argued that a significant part of the energy put in by the atmosphere is lost in a bottom boundary layer, at least for the near inertial waves. Calculations of the net downward energy flux and the rate of energy loss in what we are interpreting in Figure 8 to be a bottom boundary layer show that (in terms of a rough calculation) the energy flux into the boundary layer could be accounted for by the energy loss in the boundary layer. It is certainly true that other factors can act to remove energy from the wave field. For example, it is clear that the observed waves tend to increase in amplitude and decrease in vertical wave length in

the thermocline, where the Brunt-Väisälä frequency is large. For waves shorter than some critical value, the shear caused by these waves will be large enough so that the Richardson number would be less than $1/4$, and the flow caused by the wave might become unstable. This would extract energy from the waves (possibly putting that energy into turbulence). Such a process would be most active at the high-vertical-wave number end of the vertical wave number spectrum. It is also reasonable to expect that frictional losses will be important throughout the water column (not just in a bottom boundary layer) for waves with short vertical wave lengths. As the vertical wave length decreases, the frictional term, $\nu \partial^2 \vec{v} / dz^2$, in the horizontal momentum equation (Chapter IV) for near-inertial waves grows. In terms of the boundary layer discussed in Chapter IV, we can say that (assuming the frequency is fixed and close to inertial) as the vertical wave length decreases, the horizontal wave length will also decrease. This will cause the parameter $R = \nu k^2 / f$ of Chapter IV to increase. When this occurs, frictional losses are no longer confined to a thin bottom layer, but rather become important in the interior of the water column as well. This indicates that the argument that near-inertial waves are losing most of their energy in a bottom boundary layer is probably only applicable for near-inertial waves with small vertical wave numbers. This process of energy loss due to friction in the interior of the water column would also be expected to be most active at the high-vertical-wave number end of the vertical wave number spectrum.

Another cause of energy loss by these waves would be by interaction of the waves with the mean flow. In processing the profiler data we chose to normalize the profiles by the mean Brunt-Väisälä profile. This type of normalization was used because it made the calculations easier to compare with existing theories. However, it is well known (Phillips, 1966) that a vertical shear in the mean horizontal velocity profile can also cause changes in the amplitude and wave length of internal waves as these waves propagate through the shear profile. Perhaps the greatest difficulty in evaluating the influence of the shear on the profiles is lack of data on the direction of horizontal phase propagation of the waves relative to the mean shear flow. We have made several attempts to determine the direction of horizontal phase propagation. One attempt involved calculating the coherence between temperature and horizontal velocity components as obtained by the profiler in individual drops. In theory, observed phase differences between temperature and east velocity component and temperature and north velocity component, in the case of a single dominant wave, would allow one to determine the direction of horizontal phase propagation. In practice, the observed levels of coherence between temperature and the two velocity components were too low to infer anything about horizontal phase propagation direction. Using the observed energy levels of the near-inertial waves in the main thermocline and the mean vertical temperature gradient observed there, a rough calculation indicates that a near-inertial wave with a

frequency 20% greater than the local inertial frequency would produce a temperature signal that would be measurable in the profiles, given the resolution level attainable by the EMVP temperature measurements. The fact that the coherence between temperature and velocity measurements is so low may be due to the presence of temperature variations caused by waves with frequencies much greater than the inertial frequency (the semidiurnal tide, for example). In order to use the temperature profiles to determine horizontal propagation direction, better frequency resolution of the profile data must be obtained. Comparison of drops 235U and 236U (Figure 18), both visually and by doing lagged correlations between the east components and north components of the two profiles, suggests that strong features which can be identified between the two profiles occur at a slightly greater depth in profile 236U (4.8 kilometers to the north of 235U). If this is true it implies that these waves have a component of propagation toward the north. Taking into account the fact that the mean shear flow is primarily in the north-south direction (Figure 7), it would be expected (Frankignoul, 1972) that a wave group with a component of propagation to the north and propagating energy downward would be acted upon by the shear in such a way that the vertical wave length would decrease with increasing depth. In fact, if the wave is thought to be propagating directly north (against the major part of the mean shear), an analysis of the WKB expressions for the change in vertical wave length brought about by changing N and the presence of the

shear suggests that the two influences could be of comparable magnitude. However, Figure 3 shows that the most energetic waves have wave lengths in the deep water that are longer relative to observed wave lengths in the thermocline. We have also tried to use the stretched, normalized profiles to see if there is a shift of energetic spectral peaks in the upper versus lower parts of the (stretched) water column. We chose a set of stretched profiles (230D through 233D) which contained a distinct peak at about 130 sdb. Vertical wave number spectra for the upper and lower halves of these profiles were then calculated separately. On the assumption that the stretching of these profiles has removed changes in vertical wave number and wave amplitude due to variations of N , any change in the position of the peak in the upper half relative to the lower half might reflect the influence of shear. The result showed that there is a slight shift toward higher stretched vertical wave number in the lower half relative to the upper half, but it is very small (< 5 sdb). One might expect a shift in this direction if the waves have a component of horizontal propagation to the north. The fact that the shift is so small might indicate that the waves are propagating primarily east-west, with a small propagation component to the north.

The major conclusion of the above paragraphs is that a good evaluation of the influence of the mean shear on wave propagation awaits better estimates of horizontal phase propagation directions.

A final important result of the present work is that wave structures have been observed over the rough topography which have polarization appropriate to upward energy propagation. As pointed out in Chapter VI, there is a theoretical basis for believing that rough bottom topography at the latitude of this experiment ($\sim 28^\circ\text{N}$) could generate near-inertial waves that must propagate their energy upward, away from the bottom. Bell (1975) has calculated that rough topography could support an upward energy flux of $\sim 1 \text{ erg/cm}^2/\text{sec}$. If we accept our estimate of $.6 - 1.0 \text{ erg/cm}^2/\text{sec}$ downward for the energy flux to internal waves input by some (as yet only poorly understood) atmospheric forcing, then we see that rough topography generation of upward energy flux can be comparable to atmospheric generation of downward energy flux. Some data from current meters at 4000 meters in the MODE region (D. Porter, 1975, personal communication) indicates that, in the band of periods from 37 hours to 14 hours (encompassing the inertial period), the total energy in the frequency spectra obtained at 4000 meters depth over the smooth topography is significantly less (at least by a factor of 2) than the total energy in the above frequency band in spectra obtained at the same depth over the rough topography. The above observations suggest that, at least in regions of rough topography, one might sometimes expect to see a convergence of energy toward the thermocline, due to the combined effects of atmospheric and bottom forcing. According to Frankignoul and Strait (1972), such a convergence in the near-inertial frequency band can be seen in

records obtained at Site D ($39^{\circ} 20' N$, $70^{\circ} 00' W$). We again emphasize that we have not seen any evidence of dominant upward energy propagation (i.e. counterclockwise polarization with depth) in the smooth topography time series.

The above discussion makes clear some of the problems associated with interpreting the present analysis. These problems, in turn, suggest some future experiments which could be performed in order to clarify the influence of various processes on internal wave propagation. We would now like to propose several relevant experiments. First, a time series, similar to the one obtained over smooth topography, should be performed over a rough topography region. One of the primary difficulties with interpreting vertical wave number spectra of deep water profiles over the rough topography is that the low-frequency shear profile cannot be accurately removed if only two profiles have been obtained at a given location (at a time interval of one half of an inertial period). Any remaining low-frequency components to the profiles will cause errors in the calculated magnitudes of the clockwise and counterclockwise spectra. Although the smoothed hodographs of Figures 30 and 31 are clearly rotating counterclockwise with depth, and the main features in the hodographs appear to reverse direction over the one-half inertial period time interval between the two profiles, it is difficult to put any confidence in the interpretation of spectra calculated from single or paired profiles. A time series over rough topography could result in other interesting observations as well. For

example, one might speculate that the observed semidiurnal tidal contribution to the profiles, which resides in roughly the lowest five stretched vertical wave number estimates at the smooth topography observation side, might show a change of character over the rough topography. Interaction between the rough topography and "low-mode" semidiurnal tidal waves might lead to the scattering of the "low-mode" energy into higher modes. It would be interesting in this regard to compare the DLRC calculations (Figures 24 to 27) done for the smooth topography time series with the same calculation done for a time series over the rough topography. If, as seems likely, the bottom-induced generation of near-inertial waves is intermittent in time or space, then the "quick-look" capability associated with the EMVP data processing system would be an invaluable aid in determining when and where to perform the rough topography time series.

A second experiment involves using a pair of EMVP's to perform repeated paired profiles, such as those shown in Figure 18. The single pair in Figure 18, as already pointed out, has shown that there is an apparent tilt to energetic features that seem to correspond to each other in the two profiles. Repeated paired profiles would allow one to make a much more certain estimate of this tilt and would also (if series of paired profiles were made along two orthogonal directions) allow one to make an estimate of the horizontal wave propagation direction.

A final possible experiment would involve the combined data of an EMVP time series performed at some location (at the central mooring, in smooth topography, for example) along with a current meter mooring at the same location which is densely instrumented for the first several hundred meters off the bottom. This experiment would both help to verify the indication in the present EMVP data that there is a layer near the bottom in which the average, high-frequency, horizontal kinetic energy appears to decrease toward the bottom and would also provide frequency information which, as indicated in Chapter IV, is crucial in determining the rate of energy loss undergone by near-inertial waves as they reflect off the (smooth) bottom.

Perhaps the usefulness of a set of experimental observations can best be measured by whether analysis of that set of data clearly illuminates the way along which more comprehensive theoretical and experimental work may be carried out. The present analysis has generated both significant results and significant questions which must be answered by further work, and, therefore, under the above criterion this set of observational data has been extremely useful.

APPENDIX A

Profile Locations and Times

<u>Drop</u>	<u>Date 1973</u>	<u>Drop Time (GMT)</u>	<u>Position</u>
177	April 10	1627	32°21'.0N 64°34'.5W
178	" 10	1738	32°21'.0N 64°34'.5W
179	" 10	1858	32°21'.0N 64°34'.5W
180	" 12	1539	32°21'.0N 64°34'.5W
181	" 12	1658	32°21'.0N 64°34'.5W
182	" 12	1833	32°21'.0N 64°34'.5W
183	May 14	1458	29°24'.0N 69°39'.8W
184 †	" 15	1423	28°01'.5N 68°30'.0W
185 †	" 15	2045	28°01'.9N 68°32'.8W
186 †	" 15	2238	28°02'.7N 68°33'.8W
187 †	" 16	0430	28°01'.4N 68°30'.3W
188 †	" 16	1115	28°03'.2N 68°34'.0W
189 †	" 16	1750	28°02'.9N 68°30'.9W
190 †	" 17	0029	27°56'.1N 68°44'.5W
191 †	" 17	0547	27°57'.9N 68°39'.8W
192 †	" 17	1305	27°56'.1N 68°44'.3W
193 †	" 17	1842	27°58'.0N 68°39'.0W
194 †	" 18	0132	28°08'.2N 68°28'.3W
195 †	" 18	0801	28°08'.0N 68°18'.0W
196 †	" 18	1418	28°08'.5N 68°28'.5W
197 †	" 18	2044	28°08'.6N 68°18'.3W

<u>Drop</u>	<u>Date 1973</u>	<u>Drop Time (GMT)</u>	<u>Position</u>
198 †	May 19	0231	28°02'.5N 68°33'.6W
199	" 22	0045	27°06'.6N 69°40'.12W
200	" 22	1612	28°00'.0N 69°19'.0W
201	" 23	1512	27°43'.2N 70°01'.8W
202	" 24	0737	27°59'.3N 69°39'.0W
203	" 24	1454	27°57'.0N 69°36'.2W
204	" 24	2034	27°59'.2N 69°38'.0W
205	" 25	0310	27°59'.1N 69°38'.4W
206	" 25	0915	27°58'.0N 69°38'.0W
207	" 25	2126	29°21'.7N 70°42'.2W
208 †	June 1	0204	28°02'.0N 68°30'.8W
209 †	" 1	0559	28°02'.0N 68°30'.9W
210	" 8	2257	27°23'.5N 70°01'.2W
211	" 8	2257	27°23'.5N 70°01'.2W
212	" 9	0530	27°29'.8N 70°00'.4W
213	" 9	1217	27°23'.5N 70°01'.2W
214	" 9	1217	27°23'.5N 70°01'.2W
215	" 9	1829	27°29'.8N 70°00'.5W
216	" 9	1829	27°29'.8N 70°00'.5W
217	" 10	1220	27°39'.5N 69°31'.0W
218	" 10	1220	27°39'.5N 69°31'.0W
219 *	" 11	0523	27°59'.8N 69°39'.1W
220 *	" 11	1152	27°59'.7N 69°38'.9W
221 *	" 11	1815	27°59'.8N 69°39'.2W

<u>Drop</u>	<u>Date 1973</u>	<u>Drop Time (GMT)</u>	<u>Position</u>
222	June 11	1815	27°59'.9N 69°39'.0W
223 *	" 12	0043	27°59'.7N 69°39'.3W
224 *	" 12	0714	27°59'.8N 69°39'.2W
225	" 12	1301	27°52'.0N 69°39'.2W
226 *	" 12	1945	27°59'.8N 69°39'.0W
227 *	" 13	0219	27°59'.8N 69°39'.1W
228 *	" 13	0759	27°59'.8N 69°39'.2W
229	" 13	1220	27°51'.6N 69°42'.9W
230 *	" 13	1800	27°59'.7N 69°39'.0W
231 *	" 13	2117	27°59'.7N 69°38'.6W
232 *	" 14	0102	27°59'.8N 69°38'.8W
233 *	" 14	0451	27°59'.8N 69°39'.1W
234 *	" 14	0828	27°59'.8N 69°38'.9W
235	" 14	1210	27°57'.6N 69°38'.7W
236 *	" 14	1206	27°59'.8N 69°39'.1W
237 *	" 14	1630	27°59'.8N 69°39'.1W
238	" 14	2019	28°03'.6N 69°42'.0W
239 *	" 14	2016	27°59'.9N 69°38'.8W
240 *	" 15	0034	27°59'.4N 69°39'.1W
241	" 15	0438	28°05'.7N 69°44'.7W
242 *	" 15	0438	27°59'.8N 69°39'.1W
243 *	" 15	0800	27°59'.7N 69°39'.1W
244	" 15	1219	28°00'.6N 69°39'.8W
245 *	" 15	1219	27°59'.9N 69°39'.0W

<u>Drop</u>	<u>Date 1973</u>	<u>Drop Time (GMT)</u>	<u>Position</u>
246	June 15	1935	27°52'.1N 69°39'.0W
247	" 15	2057	27°52'.2N 69°38'.8W

(+) rough topography drops

(*) time series drops

APPENDIX B

Use of Electro-magnetic Velocity Profilers
to Measure Internal Waves

As was pointed out in Chapter I, a conversion equation must be used to obtain horizontal water velocity from values of horizontal electrical current density recorded by the EMVP. This conversion equation involves not only the above variables, but also the vertical water velocity at the point of measurement, as well as the horizontal gradient of any electrical potential that exists in the water. Vertical water velocities and horizontal potential gradients, therefore, introduce errors into the calculation of horizontal water velocity. We will now solve a rather simple problem that allows us to obtain an estimate of this error.

The model chosen is that of a rotating ocean with constant Brunt-Väisälä frequency and constant depth, H , and with a rigid surface and bottom. We assume that internal wave vertical modes exist in the water column. This assumption is not crucial in estimating the error, as will be seen later.

The equation for the electrical potential, $\hat{\phi}$, and the electrical current density, $\hat{\vec{J}} = (\hat{J}_x, \hat{J}_y, \hat{J}_z)$, generated by an ocean moving with velocity $\hat{\vec{v}}(x,y,z,t) = (\hat{u}, \hat{v}, \hat{w})$ is:

$$\nabla \hat{\phi} = \hat{\vec{v}} \times \vec{F} - \hat{\vec{J}}/\sigma, \quad \text{B-1}$$

where σ is the conductivity of the sea water, which is assumed to be constant, and $\vec{F} = (0, F_y, F_z)$ is a vector representing the terrestrial magnetic field. The coordinates x , y , and z are, respectively, magnetic east, magnetic north, and vertical. The coordinate origin is located at the sea surface, and z is positive upward.

Equation B-1 will be called the full conversion equation, since it contains all terms that relate $\hat{\phi}$, \vec{v} and \vec{J} . The horizontal components of equation B-1 are:

$$\frac{\hat{J}_x}{\sigma} = \hat{v}F_z - \hat{w}F_y - \frac{\partial \hat{\phi}}{\partial x} ;$$

$$\frac{\hat{J}_y}{\sigma} = -\hat{u}F_z - \frac{\partial \hat{\phi}}{\partial y} .$$

B-2

The underlined terms make up the "applied" conversion equation, or the equation that is actually used to convert EMVP electrical current readings to horizontal water velocity. The remaining terms cause the error. (The reader should refer to Sanford, et. al. (1974) for a more comprehensive discussion of EMVP measurements.)

Since $\nabla \cdot \vec{J} = 0$ and $\nabla \times \vec{F} = 0$, the equation to be solved becomes

$$\nabla^2 \hat{\phi} = \nabla \cdot (\vec{v} \times \vec{F}) = \vec{F} \cdot (\nabla \times \vec{v})$$

B-3

with the boundary conditions:

$$\hat{w} = \hat{J}_z = 0 \quad \text{at } z = 0;$$

$$\hat{w} = \hat{J}_z = 0 \quad \text{at } z = -H. \quad \text{B-4}$$

Evaluating $\hat{v} \times \vec{F}$, these boundary conditions may be rewritten:

$$\hat{w}(z = 0) = \hat{w}(z = -H) = 0;$$

$$\frac{\partial \hat{\phi}}{\partial z}(z = 0) = F_y \cdot \hat{u}(z = 0);$$

$$\frac{\partial \hat{\phi}}{\partial z}(z = -H) = F_y \cdot \hat{u}(z = -H). \quad \text{B-5}$$

Given $\hat{v}(x, y, z, t)$ we can, at least in principle, solve for $\hat{\phi}$ and then \hat{J} .

The internal wave equations are:

$$\frac{\partial \hat{u}}{\partial t} - f\hat{v} = -\frac{\partial \hat{p}}{\partial x};$$

$$\frac{\partial \hat{v}}{\partial t} + f\hat{u} = -\frac{\partial \hat{p}}{\partial y};$$

$$\frac{\partial \hat{w}}{\partial t} = -\frac{\partial \hat{p}}{\partial z} + \hat{b};$$

$$\frac{\partial \hat{b}}{\partial t} + N^2 \hat{w} = 0;$$

$$\frac{\partial \hat{u}}{\partial x} + \frac{\partial \hat{v}}{\partial y} + \frac{\partial \hat{w}}{\partial z} = 0. \quad \text{B-6}$$

where \hat{u} , \hat{v} and \hat{w} are, respectively, the east magnetic, north magnetic and vertical velocity components, f is the Coriolis parameter,

and \hat{p} is pressure divided by a reference density, $\hat{\rho}_0$. We have used the Boussinesq approximation, in which the density, $\hat{\rho}$, is assumed to be given by three terms:

$$\hat{\rho} = \hat{\rho}_0 + \hat{\bar{p}}(z) + \hat{\rho}(x,y,z,t), \quad \text{B-7}$$

and the water is assumed to be incompressible. The water pressure is made up of two parts, $\hat{\rho}_0 \hat{p}$ and $\hat{\rho}_0 \hat{\bar{p}}$. The hydrostatic part of the pressure is given by:

$$\hat{\rho}_0 \frac{d\hat{\bar{p}}(z)}{dz} = -g(\hat{\rho}_0 + \hat{\bar{p}}(z)), \quad \text{B-8}$$

where g is the acceleration due to gravity. Then $\rho_0 \hat{p}$ is the deviation of the pressure from hydrostatic, the buoyancy, \hat{b} , is $-g\hat{p}/\rho_0$ and the Brunt-Väisälä frequency, N , is:

$$N = \left(-\frac{g}{\hat{\rho}_0} \frac{d\hat{\bar{p}}}{dz} \right)^{1/2}. \quad \text{B-9}$$

By Fourier transforming equations B-6, where

$$\tilde{u}(x,y,z,t) = u(z;k,l,\omega) e^{i(kx + ly - \omega t)}, \quad \text{B-10}$$

and similarly for the other variables, we obtain the following equation for \tilde{w} :

$$\frac{d^2 \tilde{w}}{dz^2} + (k^2 + l^2) \frac{N^2 - \omega^2}{\omega^2 - f^2} \tilde{w} = 0. \quad \text{B-11}$$

The form of w that satisfies the boundary conditions on vertical velocity at the surface and bottom is:

$$\tilde{w} = \frac{A \sin \frac{n\pi z}{H}}{\frac{n\pi}{H}} \quad . \quad \text{B-12}$$

With n an integer, and

$$\frac{n^2\pi^2}{H^2} = (k^2 + l^2) \frac{N^2 - \omega^2}{\omega^2 - f^2} \quad . \quad \text{B-13}$$

Equations for \tilde{u} and \tilde{v} are:

$$\tilde{u} = - \frac{A}{\frac{n\pi}{H}} \frac{N^2 - \omega^2}{i\omega(\omega^2 - f^2)} \frac{\cos \frac{n\pi z}{H}}{\frac{n\pi}{H}} (ilf + k\omega); \quad \text{B-14}$$

$$\tilde{v} = - \frac{A}{\frac{n\pi}{H}} \frac{N^2 - \omega^2}{i\omega(\omega^2 - f^2)} \frac{\cos \frac{n\pi z}{H}}{\frac{n\pi}{H}} (l\omega - ikf) \quad \text{B-15}$$

Then

$$\begin{aligned} \frac{d^2\tilde{\phi}}{dz^2} - (k^2 + l^2) \tilde{\phi} &= \vec{F} \cdot (\nabla \times \vec{V}) = \\ &= F_y \frac{\sin \frac{n\pi z}{H}}{\frac{n\pi}{H}} \left\{ A \frac{N^2 - \omega^2}{i\omega(\omega^2 - f^2)} (ilf + k\omega) - ikA \right\} \\ &+ F_z \frac{\cos \frac{n\pi z}{H}}{\frac{n\pi}{H}} \left\{ Bf(k^2 + l^2) \right\}, \quad \text{B-16} \end{aligned}$$

where

$$B = - \frac{A}{\frac{n\pi}{H}} \frac{N^2 - \omega^2}{i\omega(\omega^2 - f^2)} \quad \text{B-17}$$

The boundary conditions on $\bar{\phi}$ are then:

$$\frac{d\bar{\phi}}{dz} = \frac{F_y B (ilf + k\omega)}{\frac{n\pi}{H}} \quad \text{at } z = 0 \quad \text{B-18}$$

and

$$\frac{d\bar{\phi}}{dz} = \frac{F_y B (-1)^n (ilf + k\omega)}{\frac{n\pi}{H}} \quad \text{at } z = -H \quad \text{B-19}$$

The system of equations B-16, B-18 and B-19 can now be solved to give:

$$\begin{aligned} \bar{\phi} = & \left\{ \frac{F_y A}{\sqrt{k^2 + l^2} \left(\frac{n^2 \pi^2}{H^2} + k^2 + l^2 \right)} \left(\frac{N^2 - \omega^2}{\omega(\omega^2 - f^2)} (lf - ik\omega) - ik \right) \right. \\ & \left. - \frac{F_y A (N^2 - \omega^2) (lf - ik\omega)}{\sqrt{k^2 + l^2} \omega(\omega^2 - f^2) \left(\frac{n\pi}{H} \right)^2} \right\} x \\ & x \left\{ \coth \sqrt{k^2 + l^2} H - (-1)^n \operatorname{csch} \sqrt{k^2 + l^2} H \right\} x \cosh \sqrt{k^2 + l^2} z \\ & + \left\{ \frac{F_y A}{\frac{n^2 \pi^2}{H^2} + k^2 + l^2} \left(\frac{N^2 - \omega^2}{\omega(\omega^2 - f^2)} (lf - ik\omega) - ik \right) \right. \\ & \left. - \frac{F_y A (N^2 - \omega^2) (lf - ik\omega)}{\omega(\omega^2 - f^2) \left(\frac{n\pi}{H} \right)^2} \right\} \frac{\sinh \sqrt{k^2 + l^2} z}{\sqrt{k^2 + l^2}} \\ & - \frac{1}{\frac{n^2 \pi^2}{H^2} + k^2 + l^2} \left\{ F_y A \frac{N^2 - \omega^2}{\omega(\omega^2 - f^2)} (lf - ik\omega) - ik \right\} \frac{\sin \frac{n\pi z}{H}}{\frac{n\pi}{H}} \end{aligned}$$

$$+ i \left. \frac{F_z A f (N^2 - \omega^2) (k^2 + l^2) \frac{n\pi z}{\cos H}}{\frac{n\pi}{H} \omega (\omega^2 - f^2) \frac{n\pi}{H}} \right\} \quad \text{B-20}$$

The full conversion equations have been given above (equations B-2). The applied conversion equations (those actually used to convert from $\hat{\mathbf{J}}$ to $\hat{\mathbf{v}}$) are:

$$\frac{\hat{J}_x}{\sigma} = (\hat{v} - \hat{v}^*) F_z, \quad \text{B-21}$$

$$\frac{\hat{J}_y}{\sigma} = -(\hat{u} - \hat{u}^*) F_z, \quad \text{B-22}$$

where \hat{u}^* and \hat{v}^* are depth-independent terms (Sanford, 1971).

Since we are only interested in the part of $\hat{\mathbf{J}}$ that varies with depth, we set

$$\hat{u}^* = \hat{v}^* = 0.$$

If we now let \hat{u}_{true} and \hat{v}_{true} be the velocity components as given by equations B-14 and B-15 and \hat{u}_{obs} and \hat{v}_{obs} be the components calculated from the applied conversion equations B-21 and B-22, then:

$$\hat{u}_{\text{true}} - \hat{u}_{\text{obs}} = \frac{1}{F_z} \frac{\partial \hat{\phi}}{\partial y} \quad \text{B-23}$$

$$\hat{v}_{\text{true}} - \hat{v}_{\text{obs}} = \frac{1}{F_z} \left(\frac{\partial \hat{\phi}}{\partial x} + \hat{w} F_y \right) \quad \text{B-24}$$

We see that the expressions for $\hat{\phi}$ and \hat{w} can be used to estimate the error in the conversion equations. At a given depth, z , the energy

in the u error signal is given by:

$$\begin{aligned} E u_{\text{error}}(z) &= 1/2 \langle (\tilde{u}_{\text{true}} - \tilde{u}_{\text{obs}}) (\tilde{u}_{\text{true}} - \tilde{u}_{\text{obs}})^* \rangle \\ &= \frac{1}{2F_z^2} \langle \left| \frac{\partial \tilde{\phi}}{\partial y} \right|^2 \rangle \end{aligned} \quad \text{B-25}$$

where the brackets $\langle \rangle$ indicate an average over time. Similarly, the v error signal is given by:

$$\begin{aligned} E v_{\text{error}}(z) &= 1/2 \langle (\tilde{v}_{\text{true}} - \tilde{v}_{\text{obs}}) (\tilde{v}_{\text{true}} - \tilde{v}_{\text{obs}})^* \rangle \\ &= \frac{1}{2F_z^2} \langle \left| \frac{\partial \tilde{\phi}}{\partial x} + \tilde{w} F_y \right|^2 \rangle \end{aligned} \quad \text{B-26}$$

We note that:

$$E u_{\text{true}}(z) = 1/2 \langle u_{\text{true}} \cdot u_{\text{true}}^* \rangle \quad \text{B-27}$$

and

$$E v_{\text{true}}(z) = 1/2 \langle \tilde{v}_{\text{true}} \cdot \tilde{v}_{\text{true}}^* \rangle \quad \text{B-28}$$

Returning momentarily to the expression for $\tilde{\phi}$ (equation B-20) we see that the first two terms are proportional to $\cosh \sqrt{k^2 + l^2} z$ and $(\sinh(\sqrt{k^2 + l^2} z) / \sqrt{k^2 + l^2})$. We now make the assumption that the horizontal component of the wave number vector, $\sqrt{k^2 + l^2}$, is small enough so that the cosh term is independent of z and the sinh term becomes a linear function of z . Since we are only

interested in that part of $\hat{\phi}$ that is depth-dependent, we ignore the hyperbolic cosine term. The term $(\sinh \sqrt{k^2 + l^2} z)/(\sqrt{k^2 + l^2}) \rightarrow z$ as $\sqrt{k^2 + l^2} \rightarrow 0$. If we examine the coefficient multiplying $(\sinh \sqrt{k^2 + l^2} z)/(\sqrt{k^2 + l^2})$ we see that for $k^2 + l^2 \ll (n^2\pi^2)/(H^2)$ the last term in the coefficient cancels the first term, and we are left with $(-i k F_y A)/(\frac{n^2\pi^2}{H^2})$ as the coefficient of the term proportional to z . For $k = 0$ this term disappears. Even if $k \neq 0$ this term decreases rapidly as n increases; that is, for higher modes or for frequencies close to f . Since we are only interested in those terms that are sinusoidal in z , we will ignore the terms in $\hat{\phi}$ that are either independent of z or are only weakly dependent on z .

Then

$$\hat{\phi} \approx - \frac{1}{\frac{n^2\pi^2}{H^2} + k^2 + l^2} \left\{ F_y A \left\{ \frac{N^2 - \omega^2}{\omega(\omega^2 - f^2)} (lf - ik\omega) - ik \right\} \frac{\sin \frac{n\pi z}{H}}{\frac{n\pi}{H}} \right. \\ \left. + i \frac{F_y A f (N^2 - \omega^2) (k^2 + l^2)}{\frac{n\pi}{H} \omega(\omega^2 - f^2)} \frac{\cos \frac{n\pi z}{H}}{\frac{n\pi}{H}} \right\} \quad \text{B-29}$$

(The reason for this assumption has been explained in Chapter II. Any depth-independent contributions to the profiles examined in Chapter II have been removed prior to analysis. Thus, the (approximately) depth-independent contributions of $\hat{\phi}$ should not appear in the profiles.)

We are particularly interested in the relative error in u_{obs} and v_{obs} , given by $E_{u_{\text{error}}}/E_{u_{\text{true}}}$ and $E_{v_{\text{error}}}/E_{v_{\text{true}}}$,

respectively. For simplicity, we have averaged the quantities $\bar{E}_{u_{\text{error}}}$, $\bar{E}_{v_{\text{error}}}$, $\bar{E}_{u_{\text{true}}}$, and $\bar{E}_{v_{\text{true}}}$ over depth, z , from 0 to $-H$. Then

$$\bar{E}_{u_{\text{true}}} \equiv \frac{1}{H} \int_0^H \langle \tilde{u}_{\text{true}} \cdot \tilde{u}_{\text{true}}^* \rangle dz, \quad \text{B-30}$$

and similarly for the other three quantities. The final result is that $\bar{E}_{u_{\text{error}}}/\bar{E}_{u_{\text{true}}}$ and $\bar{E}_{v_{\text{error}}}/\bar{E}_{v_{\text{true}}}$ are given by:

$$T_u \equiv \frac{\bar{E}_{u_{\text{error}}}}{\bar{E}_{u_{\text{true}}}} = \frac{l^2 \left(\frac{n\pi}{H}\right)^2}{F_z^2 \left(\frac{n^2\pi^2}{H^2} + k^2 + l^2\right)} \left\{ F_y^2 + F_y^2 \frac{\omega^2 - f^2}{N^2 - \omega^2} \right. \\ \left. \times \left(\frac{2\omega^2 k^2}{k^2\omega^2 + l^2 f^2} + \frac{\omega^2 k^2 (\omega^2 - f^2)}{(N^2 - \omega^2)(k^2\omega^2 + l^2 f^2)} \right) + \frac{F_z^2 f^2 (k^2 + l^2)}{(k^2\omega^2 + l^2 f^2) \left(\frac{n\pi}{H}\right)^2} \right\};$$

B-31

$$T_v \equiv \frac{\bar{E}_{v_{\text{error}}}}{\bar{E}_{v_{\text{true}}}} = \frac{\left(\frac{n\pi}{H}\right)^2}{\left(\frac{n^2\pi^2}{H^2} + k^2 + l^2\right)^2 (l^2\omega^2 + k^2 f^2)} \times \left\{ k^2 \frac{F_y^2}{F_z^2} \right. \\ \times \left(l^2 f^2 + k^2 \omega^2 + \frac{2\omega^2 k^2 (\omega^2 - f^2)}{(N^2 - \omega^2)} + \frac{k^2 \omega^2 (\omega^2 - f^2)^2}{(N^2 - \omega^2)^2} \right. \\ \left. - \frac{2\omega^2 (\omega^2 - f^2)^2 \left(\frac{n^2\pi^2}{H^2} + k^2 + l^2\right)}{(N^2 - \omega^2)^2} \right) + \frac{F_y^2}{F_z^2} \\ \left. \times \frac{\left(\frac{n^2\pi^2}{H^2} + k^2 + l^2\right)^2 \omega^2 (\omega^2 - f^2)^2}{(N^2 - \omega^2)^2} + \frac{f^2 k^2 (k^2 + l^2)^2}{\left(\frac{n\pi}{H}\right)^2} \right\}$$

B-32

Considering first the u-component error, it can be shown that T_u is a maximum, for a given ω and n , if the wave is propagating in the north-south direction ($k = 0$). Further, for waves traveling in the east-west direction $l = 0$, and $T_u = 0$. For

$l^2 \ll (\frac{n\pi}{H})^2$, we find that $\max \{T_u\} \propto \frac{l^2}{(\frac{n\pi}{H})^2}$, if the frequency, ω ,

is close enough to f so that $(\omega^2 - f^2)/(N^2 - \omega^2)$ is small. Since

$$\frac{l^2}{(\frac{n\pi}{H})^2} = \frac{\omega^2 - f^2}{N^2 - \omega^2} \quad \text{B-33}$$

from equation B-13,

$$\max \{T_u\} \propto \frac{\omega^2 - f^2}{N^2 - \omega^2} \quad \text{B-34}$$

Equation B-33 or B-34 shows that the relative error in the u-component energy depends only on frequency, ω , or (what amounts to the same thing) on the north-south "aspect ratio" of the wave, $l/(n\pi/H)$.

Similar statements may be made about relative error in the v-component energy. In this case, T_v is a maximum, for a given ω and n , if the wave is propagating in the east-west direction ($l = 0$). However, T_v does not go to zero as k goes to zero, because of the presence of the term involving vertical velocity in the full conversion equation for v . If $(\omega^2 - f^2)/(N^2 - \omega^2)$ is small we find that

$$\max \{T_v\} \propto \frac{k^2}{(n\pi/H)^2} \quad \text{B-35}$$

As was the case for T_u , $\max \{T_v\}$ for small $(\omega^2 - f^2)/(N^2 - \omega^2)$ depends only on the frequency, or alternatively, on the east-west aspect ratio $k/(n\pi/H)$.

Using values of the Brunt-Väisälä and inertial frequencies appropriate to the MODE center at a depth of 4500 dbar, we find that the relative error terms $\max \{T_u\}$ and $\max \{T_v\}$ are both less than 5% for periods down to about one-half day. This range of periods from inertial down to one-half day contains roughly three fourths of the energy observed in internal wave spectra from the MODE area.

We have ignored vertical variations of N and the fact that the observed waves are propagating in the vertical. Since the error terms are proportional to $(\omega^2 - f^2)/(N^2 - \omega^2)$, and this would not change if waves were propagating vertically, the presence of vertically propagating waves would not change the error estimate significantly.

The influence of varying Brunt-Väisälä frequency is somewhat more difficult to determine. If N varies weakly with z , this means the forcing terms on the right hand side of equation B-17 have coefficients that are weak functions of z . If we assume that N varies on a scale that is appreciably longer than the scale of the waves and try to solve the forced problem using two depth scales, we would find that the lowest order estimate of the relative error terms would again be proportional to $(\omega^2 - f^2)/(N^2 - \omega^2)$ but that now N is a weak function of z . The value of N used above to get

relative error estimates was taken to be that at 4500 dbar because this value is close to the minimum average value in the N profile and thus presumably maximizes the relative error.

APPENDIX C

Accuracy and Precision of Observations

It is important to distinguish between accuracy and precision when interpreting velocity measurements obtained by the EMVP. This is true because of certain characteristics of the EMVP itself. A detailed description of the arrangement of sensors on the EMVP can be found elsewhere (Sanford, et. al., 1974). It has been pointed out (Sanford, 1971) that the electrodes that sense horizontal electric current density only measure the depth-varying part of the current. That is, there is a depth-independent part of the current that is not sensed by the EMVP. Therefore, the instrument measures horizontal current in much the same way that geostrophic shear calculations do, when a "level of no motion" must be assumed. This is clearly a loss of accuracy in the instrument.

A second cause of loss of accuracy in the EMVP involves the actual location of the electrodes on the instrument. As the profiler falls, it rotates. This rotation causes an oscillatory current to flow in a coil within the profiler, since the coil is rotating in the terrestrial magnetic field. This oscillating current is then used to determine the point in a cycle of rotation when the coil is pointing toward magnetic north. The orientations of the two independent sets of electrodes on the profiler are defined relative to the direction of this "compass coil." In the present configuration of the instrument, one set of electrodes is

oriented parallel to the compass coil, and one set is oriented perpendicular to it. However, these "perpendicular" and "parallel" orientations relative to the compass coil can only be measured to about a degree. The result is that errors in defining the orientation of the electrodes on the instrument cause errors in the determination of the magnetic bearing of the horizontal electric current density vector, and thus errors in the measured water velocity. This is a systematic error, which is another cause of loss of accuracy in the measurements. If, in a small section of a profile, velocity readings from the two independent electrodes are compared, it is usually found that although the two velocity readings track each other closely with changing depth, there can be a constant offset between the two of up to 1 cm/sec. If this offset is removed, the actual RMS difference between the two readings is usually less than 0.5 cm/sec. This RMS error can be taken to be an estimate of the precision of the velocity measurements.

A more detailed discussion of EMVP velocity measurement errors can be found in Sanford et. al. (1974). The above sources of error should be kept in mind when interpreting velocity profiles.

As mentioned in the introduction, the EMVP also carries pressure, temperature and conductivity sensors. We will consider the pressure sensor error first. Because data in the EMVP is recorded in digital format, there is a quantizing error in any recorded variable. In the case of pressure, this quantizing error amounts to about 1.5 dbar. Bottom pressure values as obtained by

the EMVP for each drop in the time series have been compared in order to estimate the precision of pressure measurements. If we assume that the bottom at the time series site is flat, so that the EMVP hit bottom at the same depth in each drop, then a comparison of bottom pressures as recorded by the EMVP indicates a root-mean-square error of about ± 1 dbar at about 5500 dbar. This is a measure of the precision, or repeatability, of the pressure measurements. On the other hand, accuracy is limited by the fact that values of pressure computed from PGR (Precision Graphic Recorder) readings could be determined to only about 5 dbar.

Temperature and conductivity measurements were notably less successful than pressure measurements. The quantizing errors for temperature and conductivity are 0.017° C and 0.02 mmho/cm. The quantizing error in temperature is twice what it should have been, since the least significant bit in the digitizer was usually stuck in the "1" mode. In addition, due to a failure of the conductivity head on the profiler (the quartz liner in the head cracked under high pressure and fell out), the conductivity measurements of the head were seriously influenced by temperature and pressure. This made the computation of salinity difficult. Although a curve was derived which corrects conductivity for the above influences of temperature and pressure on the head, the resulting computed salinity was only accurate to about 0.035 ‰. This was not judged to be sufficient for density computations, and so these measurements have not been used in the present work.

Finally, a comment should be made on navigational accuracy during the time series. Ship positions were determined by Loran C. Although nominally performed at one location, a comparison of recorded ship positions for all drops during the time series indicates that the ship positions have a standard deviation of about ± 230 meters (east-west) and ± 270 meters (north-south) around a mean position of $27^{\circ} 59.75' N$, $69^{\circ} 39.04' W$. It should be noted that the above numbers are based on ship position at the beginning of each drop. The EMVP usually spent 5 to 10 minutes on the surface before it began its descent. During this time the instrument was drifting free of the ship and was presumably carried to the south by the mean flow (see Figure 5). This additional drift of the instrument to the south would result in a shift of the mean position of the time series to the south (probably by about 100 to 200 meters) but presumably would not increase the standard deviation of the drop positions appreciably.

APPENDIX D

A More General Treatment of the Partition of Energy
Between Clockwise and Counterclockwise Spectra

We let m be the vertical wave number in the stretched vertical coordinate, f be the inertial frequency, and ω be the wave frequency. In what follows, we will use the vertical coordinate s , where $s = -\tilde{z}^*$. Thus s is a stretched vertical coordinate increasing upward. The horizontal velocity components of a single internal wave may be represented by:

$$U_{\perp}(s,t;\omega,m) = e^{2\pi i(ms - \omega t)} ; U_{\top}(s,t;\omega,m) = \frac{f}{\omega} e^{2\pi i(ms - \omega t)} , \quad D-1$$

where U_{\perp} and U_{\top} are the horizontal velocity components parallel and perpendicular to the direction of horizontal phase propagation, respectively. Then (Garrett and Munk, 1972), the east and north (u and v) velocity components are given by:

$$u = i U_{\perp} \cos\phi - U_{\top} \sin\phi$$

and

$$v = i U_{\perp} \sin\phi + U_{\top} \cos\phi , \quad D-2$$

where ϕ is the horizontal phase propagation direction. We adopt the convention that m is always positive. A wave with upward phase propagation then has a positive frequency, ω , while a wave with downward phase propagation has a negative frequency. All

contributions to the profiles from upward propagating waves may then be represented by:

$$U_L^U(s, t; \phi) = \int_f^N \int_0^\infty A(\omega, m; \phi) e^{2\pi i(ms - \omega t)} dm d\omega$$

and

$$U_T^U(s, t; \phi) = \int_f^N \int_0^\infty \frac{f}{\omega} A(\omega, m; \phi) e^{2\pi i(ms - \omega t)} dm d\omega \quad D-3$$

The amplitude function, A , is considered to be non-zero only for $f \leq \omega \leq N$ and $m > 0$. Therefore, the double integrals can be considered to be integrals from $-\infty$ to $+\infty$. We similarly represent the contributions to the profiles from downward propagating waves as:

$$U_L^D(s, t; \phi) = \int_{-\infty}^\infty \int_{-\infty}^\infty B(\omega, m; \phi) e^{2\pi i(ms - \omega t)} dm d\omega$$

and

$$U_T^D(s, t; \phi) = \int_{-\infty}^\infty \int_{-\infty}^\infty \frac{f}{\omega} B(\omega, m; \phi) e^{2\pi i(ms - \omega t)} dm d\omega \quad D-4$$

In this case, B is non-zero only for $-f \leq \omega \leq -N$ and $m > 0$.

The total horizontal velocity components are then given by:

$$U_L = U_L^U + U_L^D \quad \text{and} \quad U_T = U_T^U + U_T^D. \quad D-5$$

The cross correlation between u and v and the autocorrelation for the u and v components are:

$$\rho_{uv}(\bar{s}, t; \phi) \delta(T) = \langle\langle \left\{ u(s, t) v^*(s + \bar{s}, t + T) + u^*(s, t) v(s + \bar{s}, t + T) \right\} \delta(t) \delta(t - T) \rangle_t \rangle_s \quad D-6$$

and

$$\begin{aligned} & [\rho_{uu}(\bar{s}, T; \phi) + \rho_{vv}(\bar{s}, T; \phi)] \delta(T) \\ &= \langle\langle \left\{ u(s, t) u^*(s + \bar{s}, t + T) + u^*(s, t) u(s + \bar{s}, t + T) \right. \\ & \left. + v(s, t) v^*(s + \bar{s}, t + T) + v^*(s, t) v(s + \bar{s}, t + T) \right\} \delta(t) \delta(t - T) \rangle_t \rangle_s \quad D-7 \end{aligned}$$

where the angle brackets denote averages over s and t . The δ -functions arise because we are making a linear section of the random wave field along the s axis (Konyaev, 1973). (The contributions to u and v at a given frequency and vertical wave number are assumed to be a sum of waves with random phases.)

We assume that the above integral limits may be taken as $-\infty$ to $+\infty$. This implies an infinitely deep water column. Strictly speaking, the limitation to a finite depth will cause the vertical wave number spectra calculated below to be smoothed by a window which is a function of (stretched) vertical wave number. The finite depth limitation has been ignored in what follows. Using the above expressions for the correlation functions, we can calculate the cospectrum (P), quadrature spectrum (Q), and the total energy spectrum (TE) for zero time lag. These quantities are given by:

$$P(m; \phi) + iQ(m; \phi) = \int_{-\infty}^{\infty} \int_{-\infty}^{\infty} \rho_{uv}(\bar{s}, T; \phi) \delta(T) e^{-2\pi i(m\bar{s} - \omega T)} d\bar{s} dT \quad \text{D-8}$$

and

$$TE(m; \phi) = \int_{-\infty}^{\infty} \int_{-\infty}^{\infty} (\rho_{uu} + \rho_{vv})(\bar{s}, T; \phi) \delta(T) e^{-2\pi i(m\bar{s} - \omega T)} d\bar{s} dT \quad \text{D-9}$$

Carrying out the required calculations, we find:

$$\begin{aligned} P(m; \phi) + iQ(m; \phi) = & 1/4 \left\{ \cos\phi \sin\phi \int_f^N \left(1 - \frac{f^2}{\omega^2}\right) |A(\omega, m; \phi)|^2 d\omega \right. \\ & + \int_{-f}^{-N} \left(1 - \frac{f^2}{\omega^2}\right) |B(\omega, m; \phi)|^2 d\omega \\ & \left. - i \left[\int_f^N \frac{f}{\omega} |A(\omega, m; \phi)|^2 d\omega + \int_{-f}^{-N} \frac{f}{\omega} |B(\omega, m; \phi)|^2 d\omega \right] \right\} \quad \text{D-10} \end{aligned}$$

and

$$\begin{aligned} TE(m; \phi) = & 1/4 \left\{ \int_f^N |A(m, \omega; \phi)|^2 \left(1 + \frac{f^2}{\omega^2}\right) d\omega \right. \\ & \left. + \int_{-f}^{-N} |B(\omega, m; \phi)|^2 \left(1 + \frac{f^2}{\omega^2}\right) d\omega \right\} \quad \text{D-11} \end{aligned}$$

We can simplify these expressions if we assume:

$$\begin{aligned}
 |A(m, \omega; \phi)|^2 &= (1 - \alpha(m, \omega')) E(\omega') \hat{A}(m) R(\phi) ; \\
 |B(m, \omega; \phi)|^2 &= \alpha(m, \omega') E(\omega') \hat{A}(m) R(\phi), \quad \text{D-12}
 \end{aligned}$$

where $\omega' > 0$. The value of $\alpha(m, \omega')$ is between zero and one. Use of this coefficient allows us to indicate how much energy is contributed to a one-sided frequency spectrum by waves with upward and downward phase propagation. $R(\phi)$ is assumed to be normalized so that its integral around 2π is one. $E(\omega')$ and $\hat{A}(m)$ could be identified with the frequency and vertical wave number dependence, respectively, of the Garrett-Munk spectrum given in Chapter V.

Integrating around ϕ , we get

$$TE(m) = 1/4 \int_f^N E(\omega') \hat{A}(m) \left(\frac{\omega'^2 + f^2}{\omega'^2} \right) d\omega' \quad \text{D-13}$$

and

$$Q(m) = 1/4 \int_f^N E(\omega') \hat{A}(m) \left(\frac{f}{\omega'} \right) (1 - 2\alpha) d\omega' \quad \text{D-14}$$

The clockwise and counterclockwise spectra are given (to within a constant) by:

$$C(m) = TE(m) + 2Q(m) ;$$

$$A(m) = TE(m) - 2Q(m) . \quad (\text{Gondalla, 1972}). \quad \text{D-15}$$

We point out that neither TE nor Q contains multiplicative factors involving $\cos\phi$ or $\sin\phi$ in equations D-10 and D-11. These quantities (and therefore $C(m)$ and $A(m)$) do not depend on the distribution of

$R(\phi)$ around a circle. This is another way of saying that $C(m)$ and $A(m)$ are invariant with respect to a rotation of the horizontal coordinates. If we now assume that $E(\omega')$ has a sharp peak at a frequency ω'_0 near the inertial frequency, so that $\omega'_0/f \sim 1$, then

$$\frac{A(m)}{C(m)} \approx \frac{1 - \alpha(m, \omega'_0)}{\alpha(m, \omega'_0)}, \quad \text{D-16}$$

which is the ratio of downward to upward energy propagation. For a small α (which means that most of the energy is propagating downward), $A(m)$ is much larger than $C(m)$. It is important to remember that s is positive up. If we were to use \tilde{z}^* , the stretched vertical pressure coordinate which increases downward (as for the spectrum in Figure 13, for example), then $C(m)$, the clockwise spectrum, would dominate. (Changing the vertical coordinate from s to \tilde{z}^* is equivalent to inter-changing A and C .) Several other points can be made. First, if $\alpha = 1/2$ everywhere, the quadrature spectrum will be zero, and clockwise and counterclockwise energy will be equal. The choice of $\alpha = 1/2$ corresponds to the case when, on the average, equal energy is contained by waves with upward and downward energy propagation. Second, if an energetic wave is present with a frequency much greater than inertial (such as the semidiurnal tide), we might expect that the addition of this wave will cause the ratio $A(m)/C(m)$ to approach one. It is interesting to note in this context that the estimates of $A(m)/C(m)$ (using \tilde{z}^* as the vertical

coordinate) at the smallest vertical wave numbers in Figure 22 (where we know that the semidiurnal tide is important) do seem to increase, relative to estimates at neighboring, higher stretched vertical wave numbers.

BIBLIOGRAPHY

- Bell, T. H., Jr., Topographically generated internal waves in the open ocean, Jour. Geophys. Res., Vol. 80, No. 3, pp. 320-327, 1975.
- Broglio, L., Review of Italian meteorological activities and results, Proceedings of the First International Symposium on Rocket and Satellite Meteorology, ed. by H. Wexler and J. E. Caskey, Jr., North-Holland Publishing Co., Amsterdam, p. 94, 1963.
- Charnock, H., A preliminary study of the directional spectrum of short period internal waves, Proc. 2nd U.S. Navy Symp. Mil. Oceanog., pp. 175-178, 1965.
- Elford, W. G. and D. S. Robertson, Measurements of winds in the upper atmosphere by means of drifting meteor trails II, Jour. Atmos. Terr. Phys., Vol. 4, No. 5, pp. 271-284, 1953.
- Endlich, R. M., R. C. Singleton and J.W. Kaufman, Spectral analysis of detailed vertical wind speed profiles, Jour. of the Atmos. Sciences, Vol. 26, No. 5, pp. 1030-1031, 1969.
- Fofonoff, N. P., Spectral characteristics of internal waves in the ocean, Deep-Sea Res., pp. 58-71, 1969.
- Frankignoul, C. J., Stability of finite amplitude internal waves in a shear flow, Geophys. Fluid Dynam., Vol. 4, No. 2, pp. 91-99, 1972.
- Frankignoul, C. J. and E. J. Strait, Correspondence and vertical propagation of the inertial-internal wave energy in the deep sea, Mem. Soc. Roy. des Sci. de Liege, series 6, Vol. 4, pp. 151-161, 1972.
- Garrett, C. and W. Munk, Space-time scales of internal waves, Geophys. Fluid Dynam., Vol. 2, pp. 225-264, 1972.
- Garrett, C. and W. Munk, Space-time scales of internal waves: a progress report, Jour. Geophys. Res., Vol. 80, No. 3, pp. 291-298, 1975.

- Gonella, J., A rotary-component method for analyzing meteorological and oceanographic vector time series, Deep-Sea Res., Vol. 19, No. 12, pp. 833-846, 1972.
- Hauritz, B., H. Stommel and W. H. Munk, On thermal unrest in the ocean, Rossby Memorial Volume, New York: Rockefeller Inst. Press, pp. 74-94, 1959.
- Hayes, S. P., Preliminary Measurements of the time-lagged coherence of vertical temperature profiles, Jour. Geophys. Res., Vol. 80, No. 3, pp. 307-311, 1975.
- Hayes, S. P., T. M. Joyce and R. C. Millard, Measurements of vertical fine structure in the Sargasso Sea, Jour. Geophys. Res., Vol. 80, No. 3, pp. 314-319, 1975.
- Hendershott, M. C., "Inertial Oscillations of Tidal Period." Unpublished Ph.D. dissertation, Harvard University, 1964.
- Hendry, R., Semidiurnal tides as observed in the MODE-1 field experiment, Draft Report of the MODE-1 Dynamics Group, Woods Hole Oceanographic Institution. Unpublished manuscript, 1974.
- Hines, C. O., Internal atmospheric gravity waves at ionospheric heights, Can. Jour. Phys., Vol. 38, No. 1, pp. 1441-1481, 1960.
- Hines, C. O., Diurnal tide in the upper atmosphere, Jour. Geophys. Res., Vol. 71, No. 5, pp. 1453-1459, 1966.
- Jenkins, C. M. and D. G. Watts, Spectral Analysis and Its Application. San Francisco: Holden-Day, pp. 79-82, 1968.
- Justus, C. G. and A. Woodrum, Upper atmospheric planetary-wave and gravity-wave observations, Jour. of the Atmos. Sciences, Vol. 30, No. 7, pp. 1267-1275, 1973.
- Katz, E. J., Profile of an isopycnal surface in the main thermocline of the Sargasso Sea, Jour. Phys. Ocean., Vol. 3, No. 4, pp. 448-457, 1973.
- Katz, E. J., Tow Spectra from MODE, Jour. Geophys. Res., Vol. 80, No. 9, pp. 1163-1167, 1975.
- Konyaev, K. V. Spectral Analysis of Random Processes and Fields. Moscow: "Nayka" Publishing House. Translated by K.D. Leaman. Microform Publication MP0001 from American Geophysical Union, Washington, D. C., pp. 129-132, 1973.

- LaFond, E. C. and K. G. LaFond, Thermal structure through the California front, Report N.U.C. TP 224, p. 133, 1971.
- Lazier, J. R. N., Temporal changes in some fresh water temperature structures, Jour. Phys. Ocean., Vol. 3, No. 2, pp. 226-229, 1973.
- Leaman, K. D. and T. B. Sanford, Vertical energy propagation of inertial waves: a vector spectral analysis of velocity profiles, Jour. Geophys. Res., Vol. 80 (in press) 1975.
- McNary, J. F., Determination of current velocity profile using an inclinometer line, University of Miami Report, ML 68371, 90 pages, 1968.
- Mooers, C. N. K., A technique for the cross spectrum analysis of pairs of complex-valued time series, with emphasis on properties of polarized components and rotational invariants, Deep-Sea Res., Vol. 20, No. 12, pp. 1129-1141, 1973.
- Muller, P. and D. J. Olbers, On the dynamics of internal waves in the deep ocean, Jour. Geophys. Res., (in press) 1975.
- Munk, W. and N. Phillips, Coherence and band structure of inertial motion in the sea, Rev. Geophys., Vol. 6, No. 4, pp. 447-471, 1968.
- Phillips, O. M., Energy transfer in rotating fluids by reflection of inertial waves, Phys. Fluids, Vol. 6, No. 4, pp. 513-520, 1963.
- Phillips, O. M. The Dynamics of the Upper Ocean. Cambridge, England: Cambridge University Press, pp. 173-174, 1966.
- Pochapsky, T. E., Internal waves and turbulence in the deep ocean, Jour. Phys. Ocean., Vol. 2, No. 1, pp. 96-103, 1972.
- Pochapsky, T. E. and F. D. Malone, A vertical profile of deep horizontal current near Cape Lookout, North Carolina, Jour. Mar. Res., Vol. 30, No. 2, pp. 163-167, 1972.
- Pollard, R. T., On the generation by winds of inertial waves in the ocean, Deep-Sea Res., Vol. 17, No. 4, pp. 795-812, 1970.
- Rossby, H. T., A vertical profile of currents near Plantagenet Bank, Deep-Sea Res., Vol. 16, No. 4, pp. 377-385, 1969.

- Sanford, T. B., Motionally induced electric and magnetic fields in the sea, Jour. Geophys. Res., Vol. 76, No. 15, pp. 3476-3492, 1971.
- Sanford, T. B., R. G. Drever and J. H. Dunlap, The design and performance of a free-fall electro-magnetic velocity profiler (EMVP). Woods Hole Oceanographic Institution reference 74-76. Unpublished manuscript. 1974.
- Smith, L. B., The measurement of winds between 100,000 and 300,000 feet by use of chaff rockets, Jour. Meteor., Vol. 17, No. 3, pp. 296-310, 1960.
- Titov, V. B. and L. M. Fomin, Vertical structure of currents in the Indian Ocean based on measurements, Oceanology, Vol. 11, No. 4, pp. 486-493, 1971.
- Voorhis, A. D., Measurements of vertical motion and the partition of energy in the New England slope water, Deep-Sea Res., Vol. 15, No. 5, pp. 599-608, 1968.
- Voorhis, A. D. and R. R. Benoit, MODE SOFAR Float in situ data summary, Woods Hole Oceanographic Institution Technical Report 74-37. Unpublished manuscript. 1974.
- Webster, F., Observations of inertial-period motions in the deep sea, Rev. Geophys., Vol. 6, No. 4, pp. 473-490, 1968.
- Webster, F., Turbulence spectra in the ocean, Deep-Sea Res., Suppl. to Vol. 16, pp. 357-368, 1969.
- Wunsch, C., Progressive internal waves on slopes, Jour. Fluid Mech., Vol. 35, No. 1, pp. 131-144, 1969.
- Yih, C.-S. Fluid Mechanics. New York: McGraw-Hill. p. 44, 1969.

BIOGRAPHICAL NOTE

NAME: Kevin Douglas Leaman

BORN: November 23, 1948, Lakewood, Ohio

MARITAL STATUS: Married to the former Diane Saul

EDUCATION:

<u>Institution</u>	<u>Dates of Attendance</u>	<u>Degree Earned</u>	<u>Date of Degree</u>	<u>Major Field</u>
Univ. of Washington	9/66-6/67			Oceanography
Univ. of Michigan	9/67-6/71	B.S. M.S.	12/70 12/72	Oceanography Oceanography

EMPLOYMENT:

<u>Institution</u>	<u>Dates of Employment</u>	<u>Duties</u>
Univ. of Michigan	9/69-6/70	Teaching Assistant in Department of Meteorology and Oceanography
Woods Hole Ocean. Inst.	1/74-6/75	Research Assistant in Physical Oceanography

PUBLICATIONS:

Translation from Russian to English of Konyaev, K. V. Spectral Analysis of Random Processes and Fields. Moscow: "Nayka" Publishing House. Microform Publication MP0001 from American Geophysical Union, Washington, D. C., 1973.

Leaman, K. D. and T. B. Sanford, Vertical energy propagation of inertial waves: a vector spectral analysis of velocity profiles, Jour. Geophys. Res., Vol. 80 (in press), 1975.